GEOMETRY MODIFICATION EFFECTS
ON A JUNCTION VORTEX FLOW

by

George A. Frangistas

Thesis submitted to the Graduate Faculty
of the Virginia Polytechnic Institute and State University
in partial fulfillment of the requirements for the degree of

MASTER OF SCIENCE

in

Mechanical Engineering

APPROVED:

F. J. Pierce, Chairman

W. C. Thomas

D. J. Nelson

May, 1987

Blacksburg, Virginia

GEOMETRY MODIFICATIONS EFFECTS ON A JUNCTION VORTEX FLOW

by

George A. Frangistas

Committee Chairman: F. J. Pierce
Mechanical Engineering

(ABSTRACT)

The effects of geometry modifications on some properties of time-resolved flow measurements on the upstream symmetry plane of a junction vortex region were studied. A single linearized hot-wire was used to characterize the spatial distribution of the fluctuating flow turbulent kinetic energy. The distribution was integrated to give a measure of the turbulent kinetic energy content of the flow region where the largest fluctuations were seen in real time smoke visualizations. The wire signal was also used for spectral estimations throughout the flow field.

Six different cases were considered including a reference case with no geometry changes. The geometry modifications consisted of a large circular wraparound fillet, a small elliptic wraparound fillet, a small circular wraparound fillet, an upstream flow fence and, a large leading-edge triangular fillet. In the smoke visualizations, none of the modifications had any significant effect except the large triangular fillet which resulted in a reduced vortex structure. The large triangular fillet also appeared to be the most effective in significantly reducing the integrated turbulent kinetic energy. With

regard to the turbulent kinetic energy, the elliptic wraparound fillet had an insignificant effect while the large and small wraparound fillets and the vortex generator fence had adverse effects.

The spectra obtained over the flow field suggest that the upstream turbulent boundary layer was the driving force behind the junction vortex time variant behavior. An examination of the low frequency end of the spectra suggests a weak local peak at about 11 Hz for the flow between the upstream separation point and the average vortex center.

ACKNOWLEDGEMENTS

The author expresses his thanks to Dr. Felix J. Pierce for his relentless efforts in providing help, guidance, and the necessary feeling of motivation throughout this research. Thanks are also extended to Dr. W. C. Thomas and Dr. D. J. Nelson for serving on the advisory committee.

Gratitude is expressed to Mr. S. K. Nath and Mr. J. Shin for their assistance in the laboratory.

Special thanks are extended to his parents and family for their encouragement and support and for never questioning his ability to succeed.

TABLE OF CONTENTS

TABLE OF CONTENTS (cont.)

LIST OF FIGURES

LIST OF FIGURES (Cont.)

LIST OF FIGURES (Cont.)

LIST OF TABLES

1. Introduction

The objective of this research was to experimentally study some characteristics of the time variant flow of the incompressible, three-dimensional, separation and junction vortex flow upstream of a streamlined body extending beyond a turbulent boundary layer. This type of flow, shown in Fig. 1-1, is dominated by a horseshoe-shaped vortex, [1]. The formation of this vortex flow is the result of the total pressure gradient through the boundary layer upstream in the proximity of the body. Such vortices form at the junction of aeroplane wings and fuselages, around the bases of bridge piers, at control surface and body junctions, and at the base of tall isolated buildings in the presence of the atmospheric turbulent boundary layer.

Recent studies on the junction vortex flow include the work of Menna [2], Baker [1], and Harsh [3]. The quantitative data available describe the mean flow in the vortex system including wall pressure measurements [1], oil-flow visualizations [1,3], mean velocity field, and static and total pressure measurements in the flow field [3]. The time varying characteristics have only been described qualitatively through smoke visualization. This experimental study attempts to describe quantitatively some characteristics of the time-resolved behavior of the junction vortex, and the effects of flow geometry modifications on the junction vortex flow region. This work focuses on an estimate of the turbulent kinetic energy and the spectral signature of the upstream plane of symmetry flow. Measurements were made using a single hot-wire sensor placed normal to the upstream mean velocity

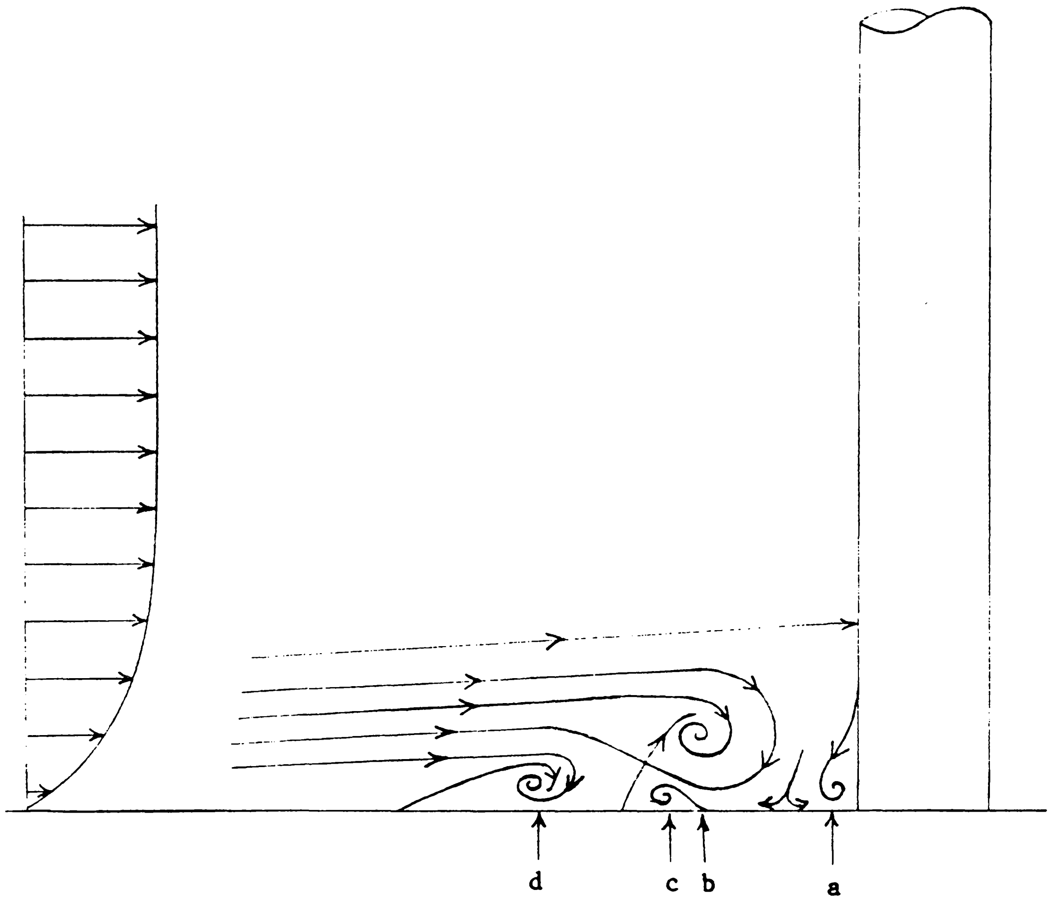

(a) Vortex caused by separation of the boundary layer on the upstream face of the cylinder.

(b) Main or primary vortex.

(c) Vortex caused by separation of the boundary layer beneath the main vortex.

(d) Vortex caused by the primary separation.

Figure 1-1 The Junction Vortex Flow After Baker [1].

vector. The sensor was positioned along the symmetry plane of the upstream flow as shown in Fig. 1-2.

The work presented here is a first attempt in examining these characteristics of the time varying behavior.

There are inherent limitations in using a single hot-wire sensor:

1. It is not directionally sensitive in the presence of flow reversal.
2. It is difficult to interpret in zones of high local turbulence intensity because it senses some combination of the velocity components along the x,y,z axes as defined in Fig. 1-2.
3. It may cause interference with the flow and/or itself, particularly in regions of large velocity fluctuations.

With those limitations in mind, measurements were taken with the test body seen in Fig. 1-3. in the wind tunnel described by Harsh [3] which has a rectangular cross section 0.61 m high by 0.91 m wide.

Two types of measurements taken were:

1. The root-mean-square (rms) value of the linearized hot-wire signal were recorded. This was taken as an approximation to the square root of the kinetic energy at a particular location.
2. Spectral estimations were made to obtain information on the frequency content of the flow in the vortex region.

Six separate cases were studied. The streamlined cylinder as seen in Fig. 1-3 was used as a reference flow. Subsequently, five geometry modifications were made of the physical junction or corner region. The

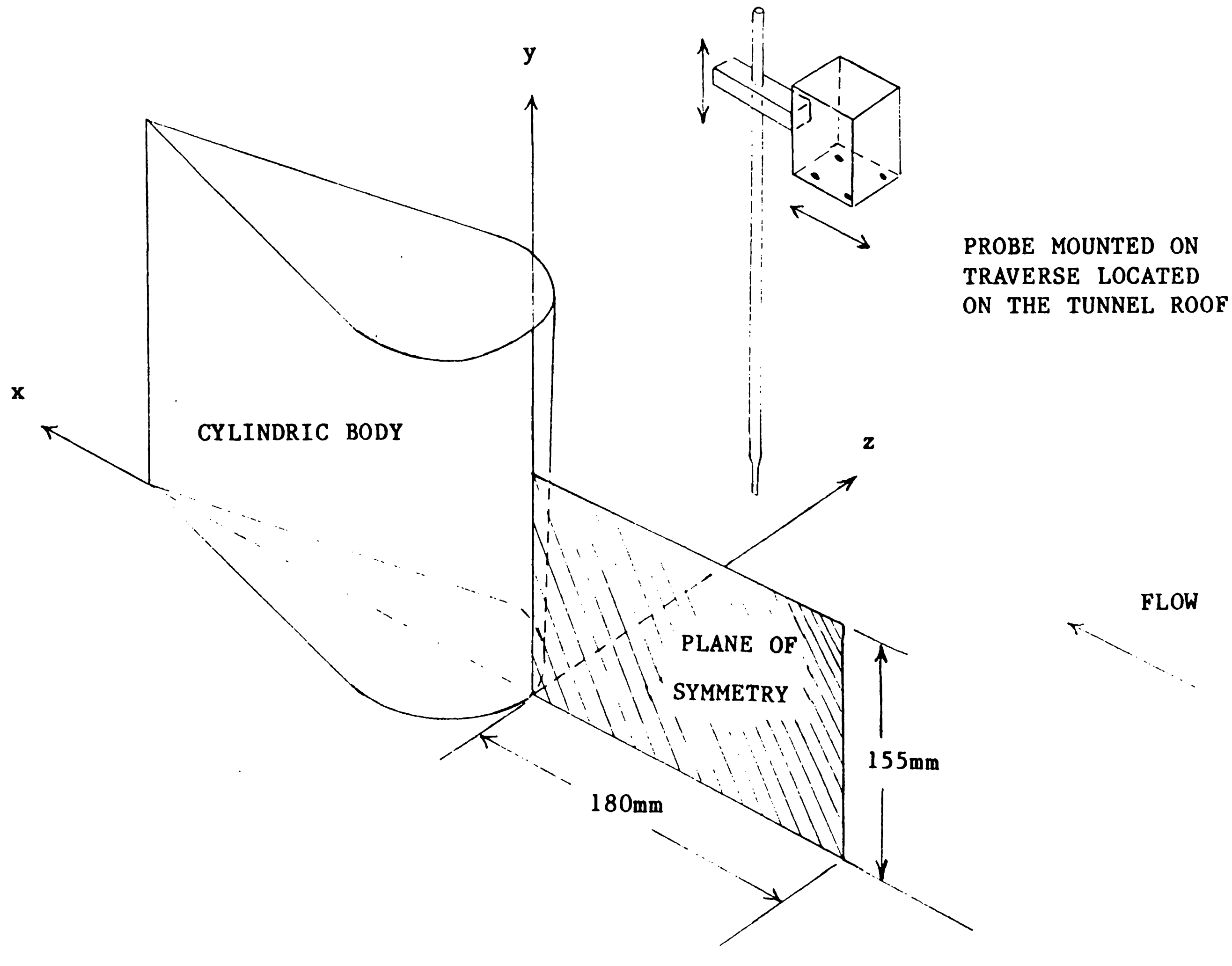

Figure 1-2 The Symmetry Plane.

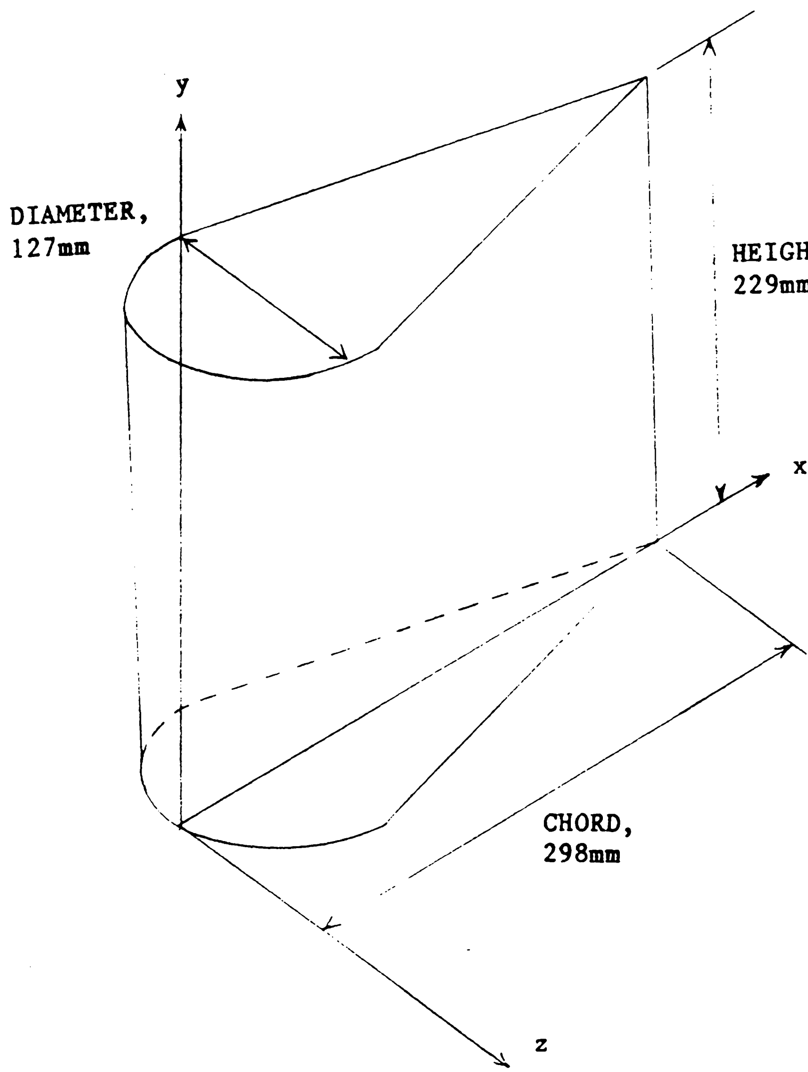

Figure 1-3 The Cylindric Test Body.

geometry modifications were made to determine their influence on the time variant character of the junction vortex flow, in particular, their effects on the kinetic energy field and spectral estimates as sensed by a single hot wire probe on the plane of symmetry flow.

2. PRELIMINARY WORK

2-1 Geometrical Modifications

The modifications made to the corner between the body and the floor were intended to influence and modify the turbulent junction vortex flow. In this study, the turbulent kinetic energy generated by the vortex system and its frequency content were examined. The basic teardrop test body geometry was modified by adding four collars or fillets and a fence. The fillets changed the corner geometry of the right angle between the body and the tunnel floor. These modifications include a:

(1) large circular wraparound fillet

(2) small elliptic wraparound fillet

(3) small circular wraparound fillet

(4) large triangular leading edge fillet, and an

(5) upstream vortex generator or fence.

The geometric details of this choice of modifications were guided by the shape of the large vortex as seen in the mean flow structure determined in earlier five-hole probe results [4], and from the shape and dynamic behavior of the primary vortex as seen in real-time smoke visualizations.

The first three modifications were fillets which were designed to slide over the test body and rest on the tunnel floor as shown in Fig. 2-1. Their descriptive names are related to their constant cross-sections that wrapped around the body much as a collar. The cross-

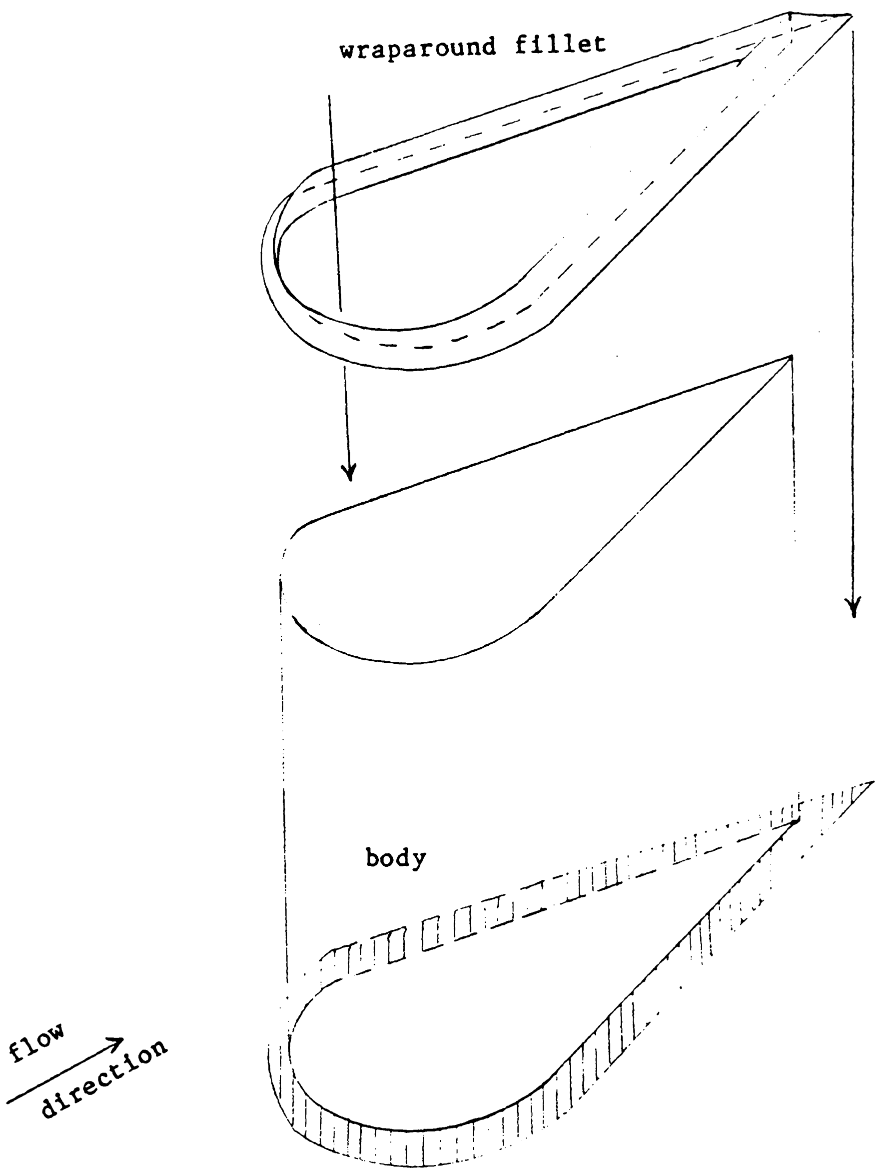

Figure 2-1 The Wrap Around Fillets of Constant Cross Section.

sections are shown in Fig. 2-2. Automotive body filler was used to make these fillets. This material proved convenient to use and gave better results than plaster, epoxy resin, plastecine, wax or silicone. The body filler shape was defined by a carefully formed metal scraper with one of its corners in the form of the desired cross section for the given fillet. This metal piece was placed vertically on the floor and perpendicular to the body. After covering the body and the floor with wax paper, the body filler was placed all around the corner of the cylindric body. The fillet was formed by sliding the scraper along the entire perimeter of the test body. After a curing period of two hours, each fillet was hand finished to a streamlined taper, faired to a point at the downstream end, approximately 30 mm beyond the trailing edge of the test body.

The large triangular leading edge fillet was made of plaster and did not wrap around the entire test body. Here again, it was arbitrarily decided to have a simple design where the two sides forming the fillet were flat surfaces. These sides were nearly triangular with the side in contact with the test body curved to accommodate the cylindric contour as shown in Fig. 2-3.

The vortex generator or fence was made up of seven copper circular cylinders glued vertically on a flat metal plate and placed upstream of the bluff body as shown in Fig. 2-4. The fence was placed in the approximate position of the separation line in an effort to anchor it. The physical presence of the fence cylinders was intended to stabilize the strong time-variant oscillations of the junction vortex as seen in real-time smoke visualizations.

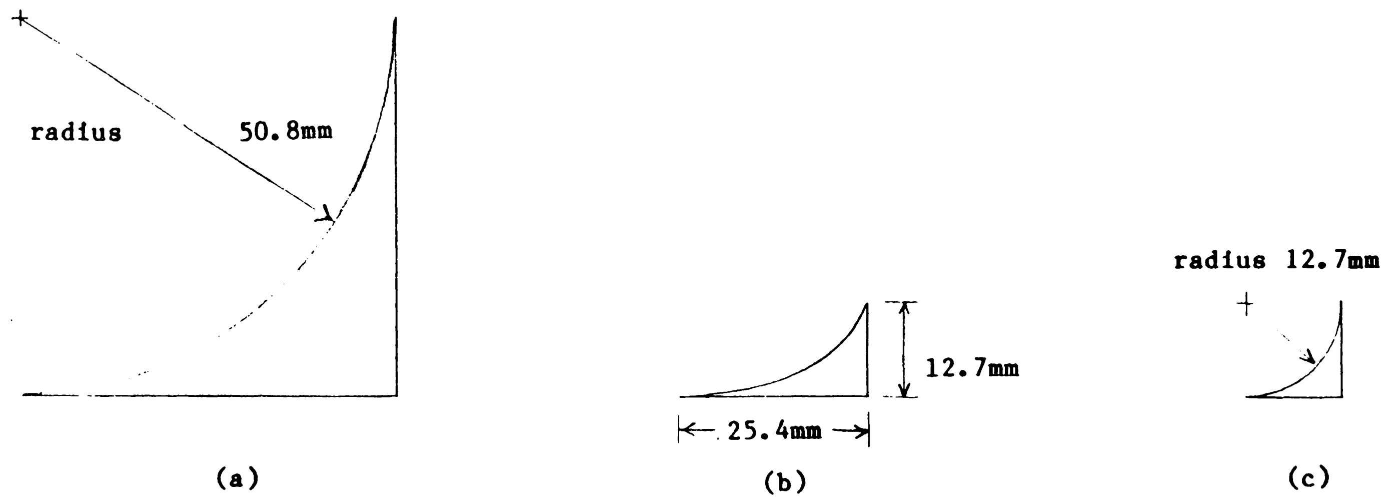

Figure 2-2 Cross Sections (to scale) of the Large Circular Fillet (a), the Small Elliptic Fillet (b), and the Small Circular Fillet (c).

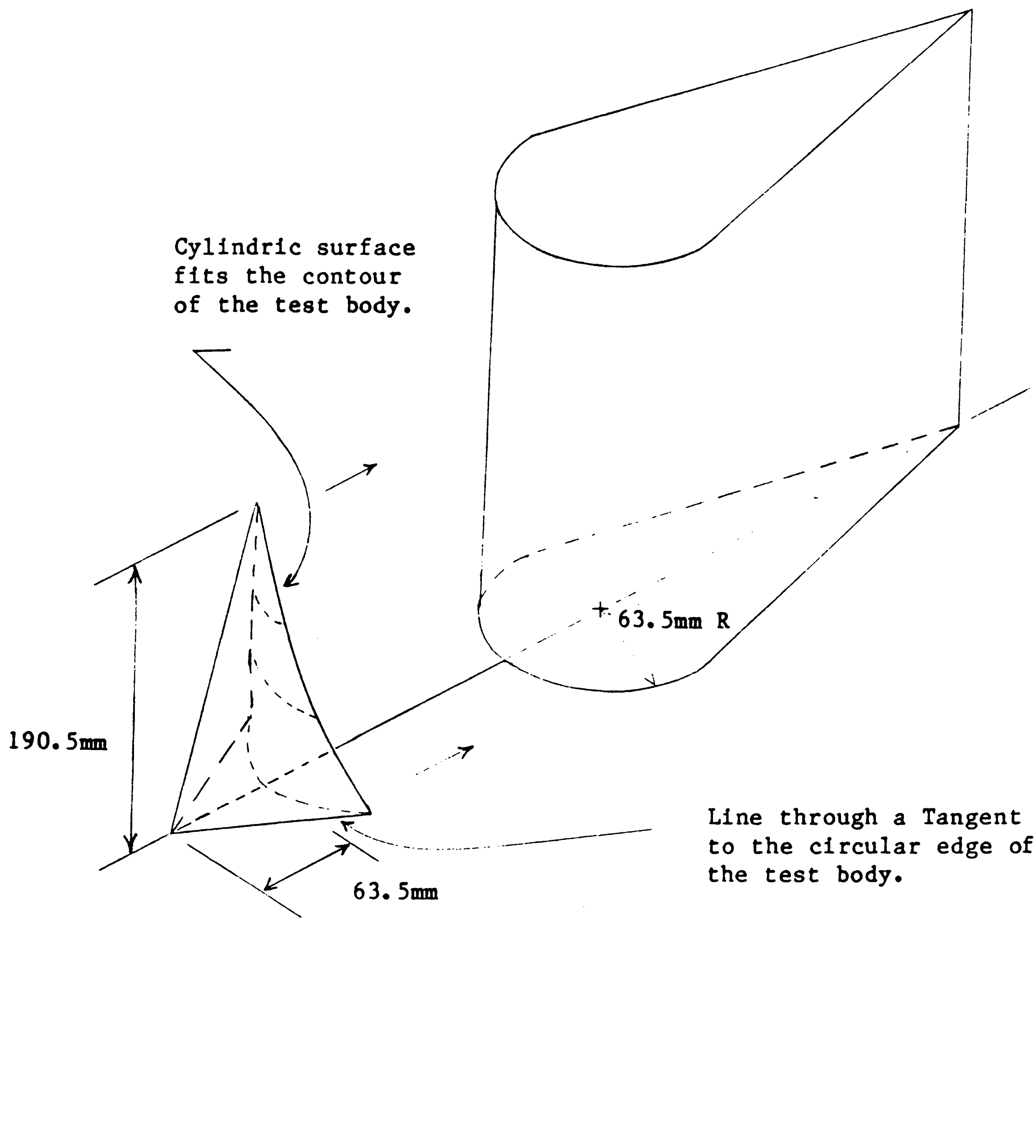

Figure 2-3 The Large Triangular Fillet.

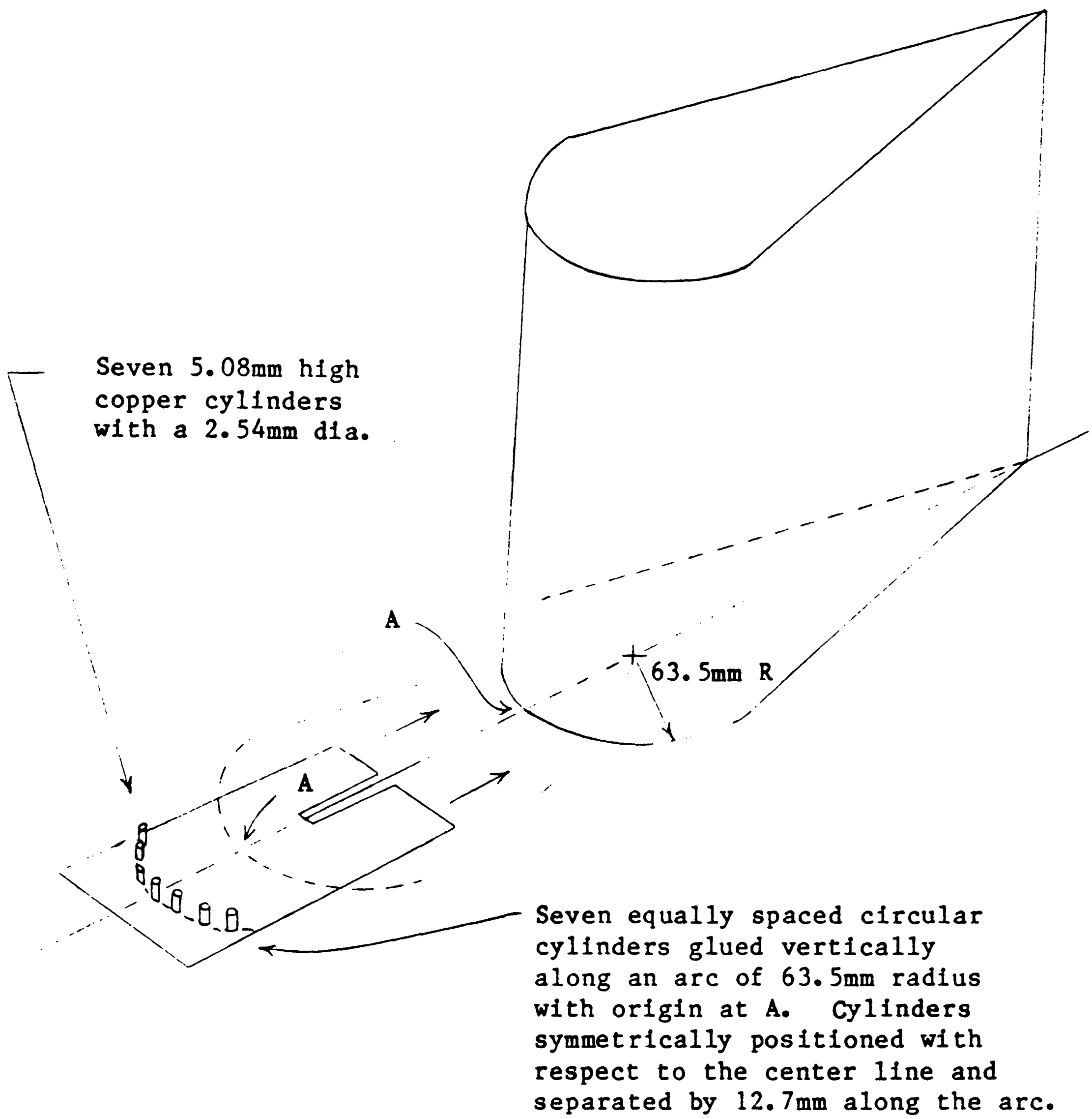

Figure 2-4 The Fence or Vortex Generator.

2-2 Real Time Smoke Visualizations

In order to obtain a clear image of the turbulent junction vortex system, real-time smoke visualizations were made with smoke injected through the tunnel floor. Initially, two types of smoke were used, theatrical smoke and chemical smoke.

The theatrical smoke is a water based fog that is more easily generated and handled. However, this smoke had a low light reflectivity which made it difficult to capture on film.

The preferred smoke was a chemical smoke. This smoke results when titanium tetrachloride combines with atmospheric moisture to form a highly visible, persistent white smoke cloud. Small quantities of very dilute hydrochloric acid ($HC\ell$) vapor is liberated with the smoke and this potential hazard must be considered with only short-term runs in even a well ventilated laboratory space.

Four smoke ports were made on a removable tunnel floor piece. Smoke was injected along the tunnel floor centerline at the points as shown in Fig. 2-5. A light sheet was used to illuminate the symmetry plane. The light sheet source was a standard 35 mm slide projector in which a darkened slide having a 0.4 mm clear slot was inserted.

Real time smoke flow visualizations were made and video taped for all six cases. Due to their physical size, some fillets covered one or more smoke injection ports. On the video tapes none of the geometry modifications seemed to noticeably affect the vortex flow except the large triangular fillet which noticeably reduced any vortex formation. Nevertheless, the smoke visualizations gave an indication of the time

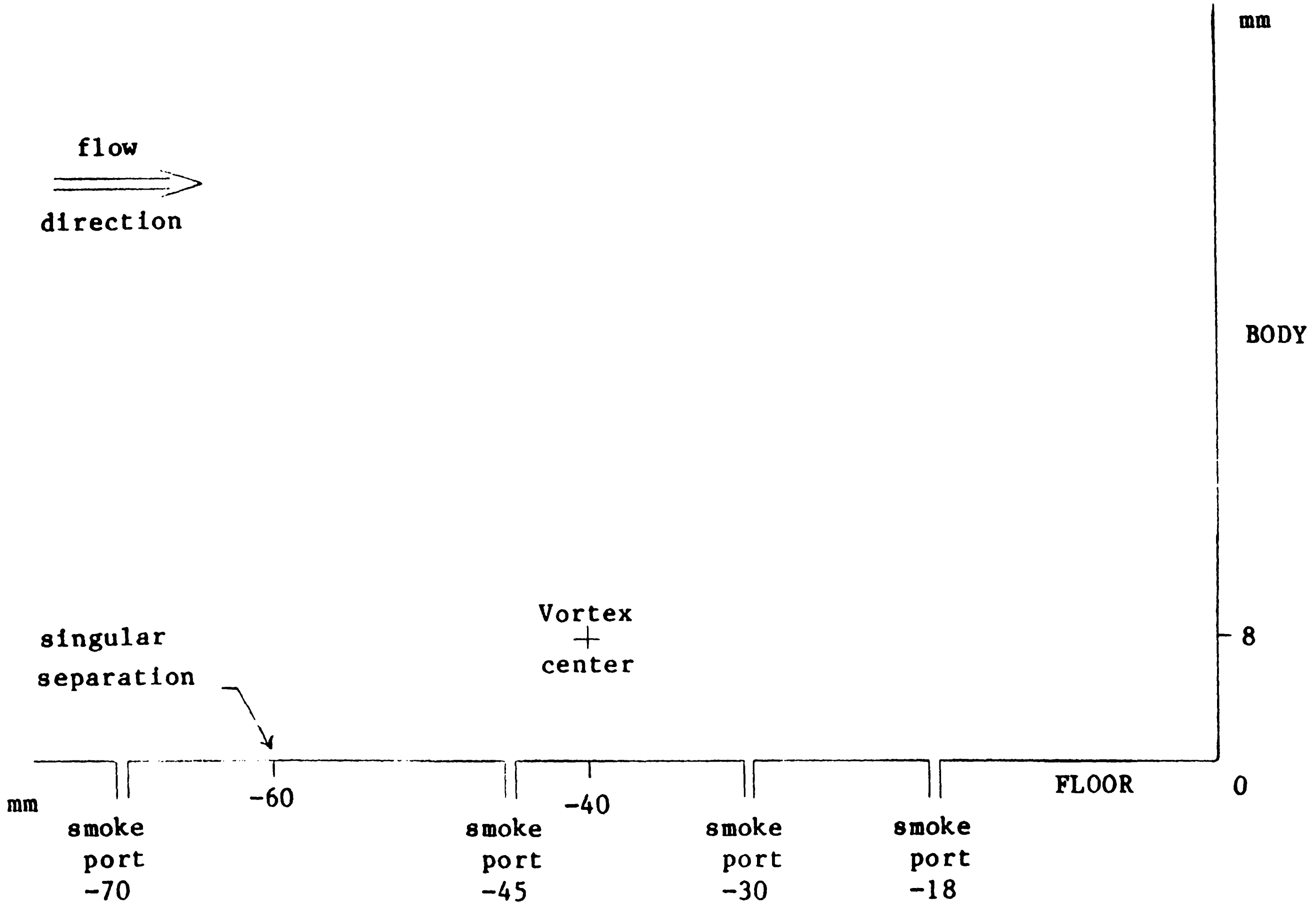

Figure 2-5 Location of the Four Smoke Ports.

variant character of each of the geometrically modified junction vortex systems.

2-3 Surface Flow Visualizations

The mean surface flows on the flat floor of the wind tunnel and on the bluff body were made visible using an oil-film technique described by Squire, et al. [5]. The details of applying the technique to this particular experiment are described by Harsh [3] who carried out extensive earlier flow visualizations with the streamlined body. For comparison, two additional flow visualizations were made, one using the small circular fillet and a second using the small elliptic fillet. A schematic diagram of what was seen in each case is shown in Figs. 2-6 and 2-7. The primary separation point (point A) was moved upstream by the fillets. In comparison with Harsh's work it would appear that point A was moved about 15 mm for the elliptic fillet and about 10 mm for the small circular fillet. This shift was the only significant difference that was noted on the oil flow visualizations.

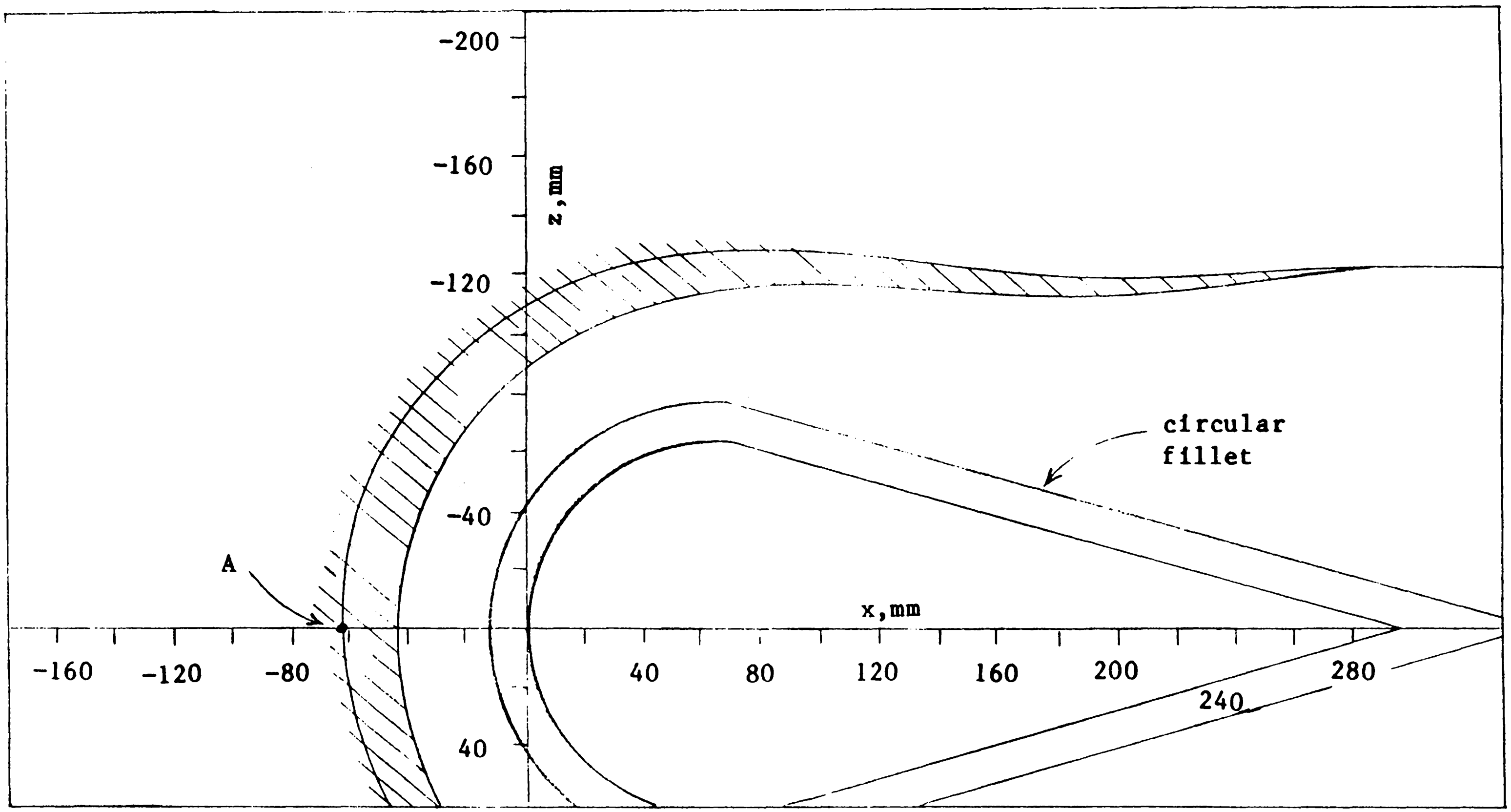

Figure 2-6 Surface Flow Visualization for the Small Circular Fillet.

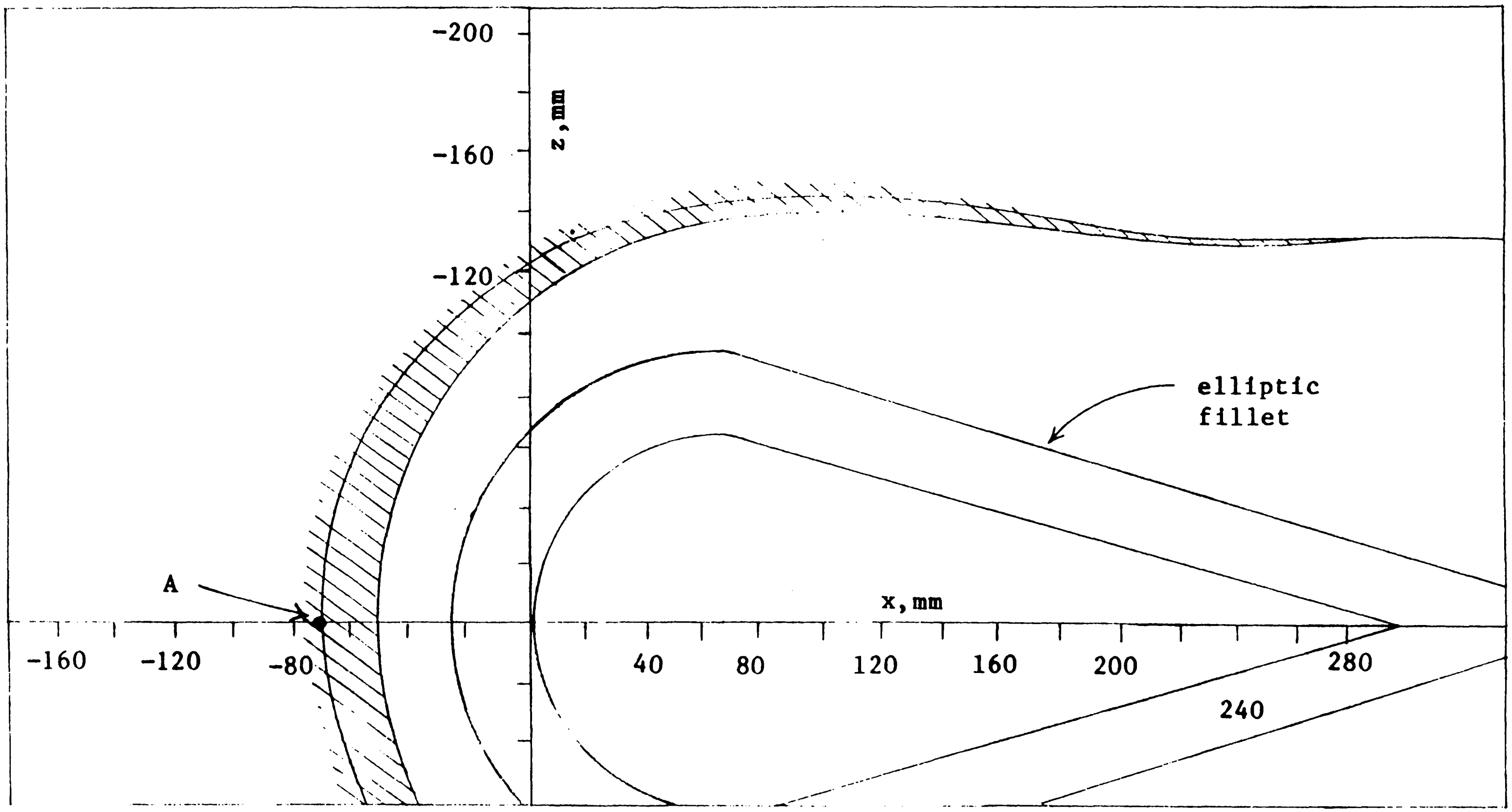

Figure 2-7 Surface Flow Visualization for the Small Elliptic Fillet.

3. SET-UP AND PARAMETERS

3-1 Running Conditions

Nominal laboratory temperature	25°C
Nominal laboratory barometric pressure	94.5 kPa
Nominal test section velocity	22.3 m/s
Reynold number based on body diameter	145,000

3-2 Instrumentation

The objective of this experimental study was to describe some additional characteristics of the time varying behavior of the horseshoe vortex system in a separated three-dimensional turbulent boundary layer. Three choices of instrumentation were considered:

1. Laser-Doppler velocimeter. While such a system was available, the extensive time commitment needed for a sound familiarity with its operation precluded this choice for this first attempt in gathering the necessary data.
2. Hot-wire anemometer. This system is considered the principal instrument in measuring turbulence [6].
3. Hot-film anemometer. This is similar to item (2). The film has the advantage of being a more rugged, trouble free, sensor by comparison to the wire. However, questions on frequency response persist for films.

The hot-wire sensor was chosen over the hot-film. Justification for this decision is given in the next section. The hot-wire system

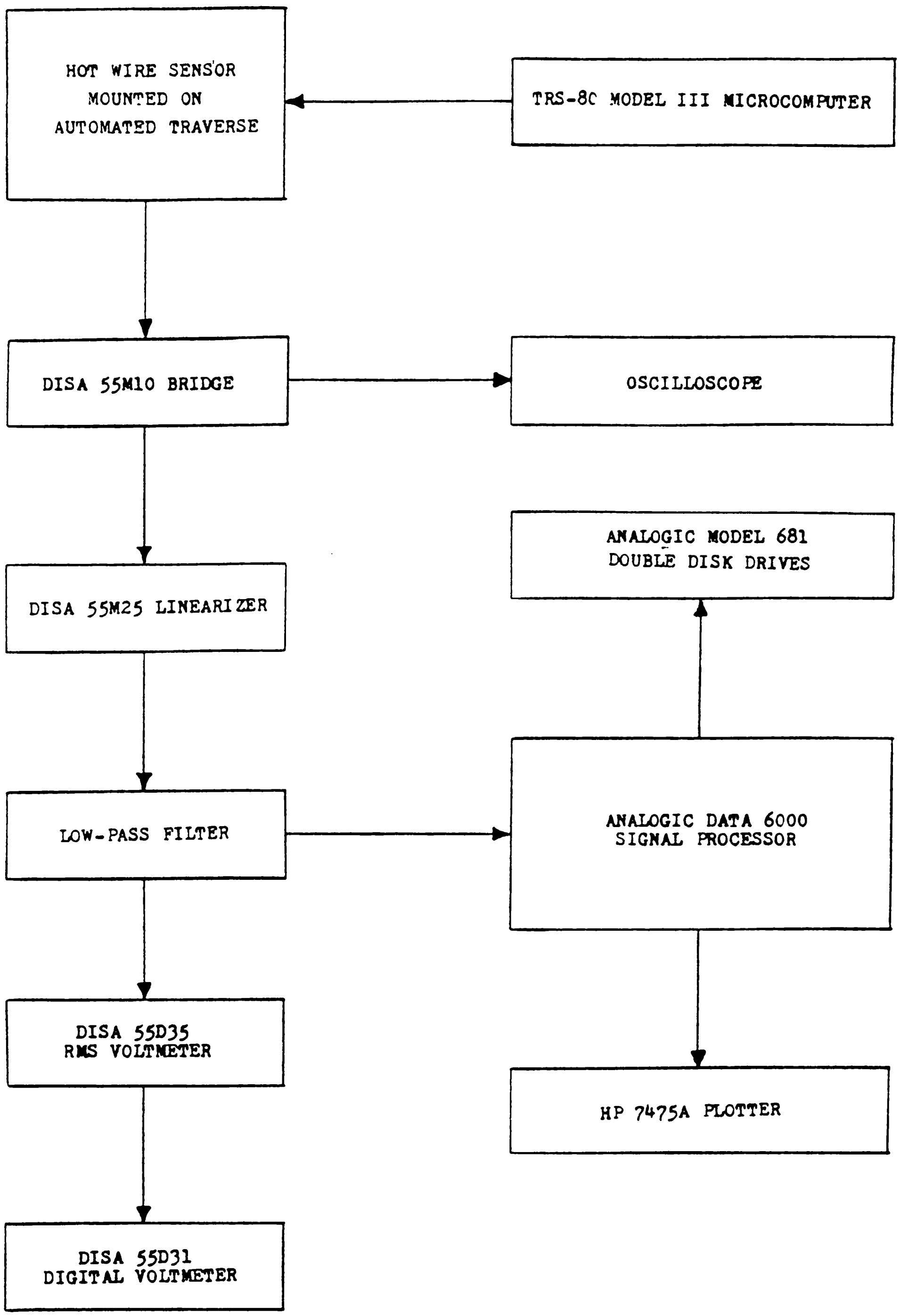

Figure 3-1 Block Diagram of the Data Acquisition System.

used is shown in Fig. 3-1. A TSI 1210-T1.5 tungsten hot wire sensor was used with a Disa 55M10 CTA (constant temperature anemometer) and standard bridge. The bridge output was linearized using a Disa 55M25 linearizer. The linearized signal was then filtered by a ten-pole Butterworth (-60 dB/octave roll-off) active low pass filter. The filter output was divided and input to:

(1) A Disa 55D35 RMS (root-mean-square) voltmeter connected in series to a Disa 55D31 digital voltmeter. The digital voltmeter served as a convenient digital read-out of the RMS voltmeter.

(2) An Analogic Data 6000 signal processor with a model 620 front end which allows sampling rates up to 50 kHz. An Analogic model 681 double disk drive provided the Data 6000 with additional storage for permanent records of both raw data and processed results.

The bridge output was also monitored on an oscilloscope. Hard copies of the Data 6000 output were made on a Hewlett Packard 7475A plotter.

The probe was positioned vertically by a two degree-of-freedom traverse run by a Radio Shack TRS-80 microcomputer.

3-3 Choice of Sensor

While the wire and film sensors are very similar, the films are more rugged. Since the data acquisition phase was expected to last from

4 to 6 weeks, there was concern that a given hot-wire sensor would not survive such a long period of service.

Both type sensors were tested in the calibration tunnel described in reference [3] to determine whether a film (TSI 1210-20) could reproduce the spectrum obtained with a wire (TSI 1210-T1.5). No linearization was done for the test conducted under the following conditions:

Ambient temperature	25°C
Barometric pressure	94.3 kPa
Free stream velocity	22 m/s
Velocity at sensor location	18 m/s
Low-pass filter cut-off	15 kHz
Sampling frequency	40 kHz
Number of averaged FFT's	100
Position from floor (within boundary layer)	6.3 mm

Both sensors were placed normal to the free stream velocity vector.

The averaged Fast Fourier Transform (FFT) output of each sensor is shown in Figs. 3-2 and 3-3. The magnitudes on these graphs are plotted on logarithmic scale (dB).

Both graphs have the same shape and the sharp filter roll-off can be seen beyond 15 kHz. The wire spectrum is approximately 8 dB lower over the entire frequency range by comparison to the film spectrum. This difference of 8 db is most likely due to the fact that the bridge

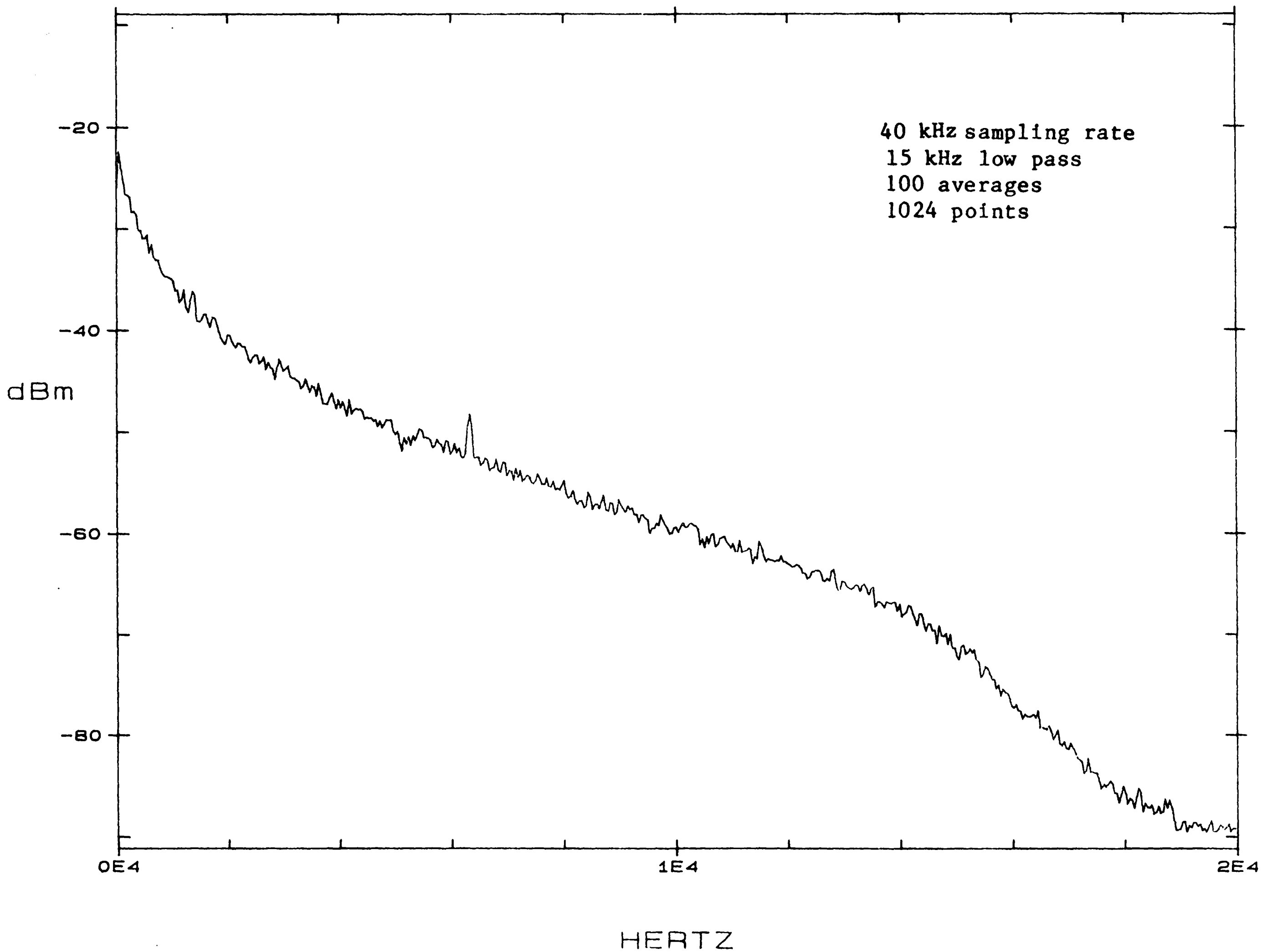

Figure 3-2 Nonlinearized Film Response After 100 Averages.

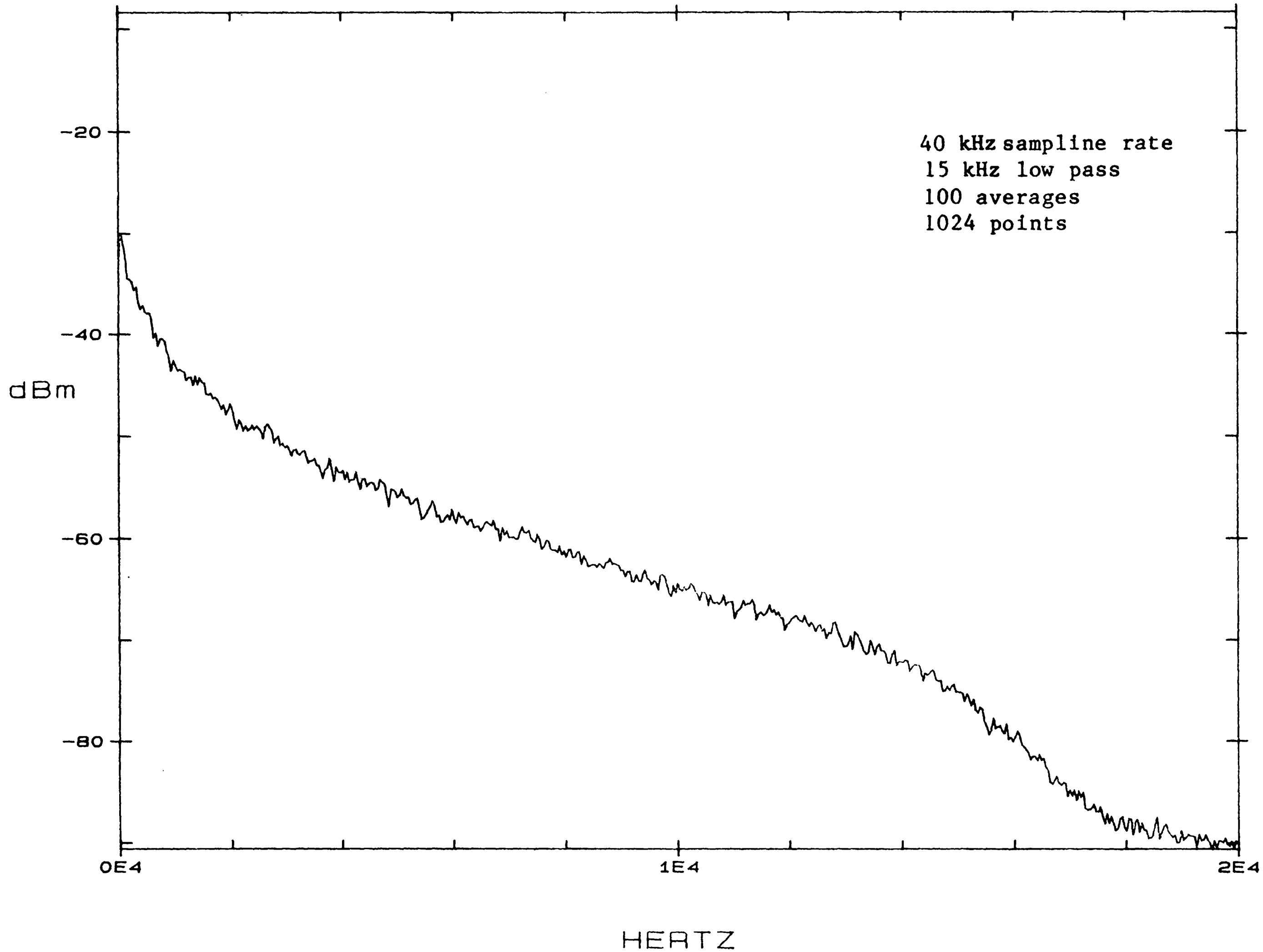

Figure 3-3 Nonlinearized Wire Response After 100 Averages

output voltages are different for the wire and the film. Since no linearization was done, these voltage differences would result in differences in the computed Discrete Fourier Transforms (DFT).

The significant difference between these two plots is the peak at about 6 kHz seen on the film response. This peak was attributed to shedding off the sensor support prongs.

The Reynolds number based on the prong diameter was

$$Re = \frac{Ud}{\nu} = \frac{18 \text{ m/s } 0.635 \ 10^{-3} \text{m}}{1.95 \ 10^{-5} \ \text{m}^2/\text{s}} = 586 \ .$$

Using the Reynolds Strouhal correlation found in [7], a Re of 586 has a corresponding Strouhal number of 0.22. Using the definition of the Strouhal number, St=fd/U, and solving for the frequency, the shedding frequency of the prongs can be estimated as

$$f = \frac{0.22 \ (18 \text{ m/s})}{0.635 \ 10^{-3} \text{m}} = 6200 \text{ Hz}$$

This frequency is the shedding frequency based on the nominal diameter of the prongs. The actual prongs are tapered toward the film element to about half their nominal diameter. This would suggest that the shedding frequency the film might sense could be as high as approximately twice this value.

Whether the 6 kHz peak is due to shedding from the upper portion of the support prongs or not, could not be determined. However, concern over the repeatable detection of this frequency spike resulted in the choice of the hot wire as the preferred sensor element.

3-4 Linearizing

The output voltage of a constant temperature anemometer is a nonlinear function of the flow velocity. This nonlinearity does not have a large influence in measurements of small degrees of turbulence since in such a case only a small portion of the calibration curve is used which may be considered to be locally linear. At higher turbulence intensities, however, the curvature of the calibration curve can become significant [8]. For the junction vortex, linearization was judged necessary. The linearizer was calibrated for both the wire and film probes using velocity data obtained with a pitot-static probe. Although it was decided to use the wire over the film, both were linearized for comparison. The transfer functions of the bridge and the linearizer output are shown for comparison in Fig. 3-4. The linearized signal is within 2 percent of reproducing the velocities measured with a pressure probe.

3-5 Low-Pass Filter and Sampling Rate

The low-pass filter is used in conjunction with digital sampling to prevent frequency aliasing of a signal due to an insufficient sampling rate. Sampling theory dictates that to accurately describe a time history in the frequency domain, the sample rate must be at least two times the highest frequency contained in the signal. This theory is the Nyquist criterion. A typical turbulent boundary layer has a broad band signal extending beyond 20 kHz as reported by Klebanoff [9]. Nevertheless, most of the turbulent energy is contained in the lower

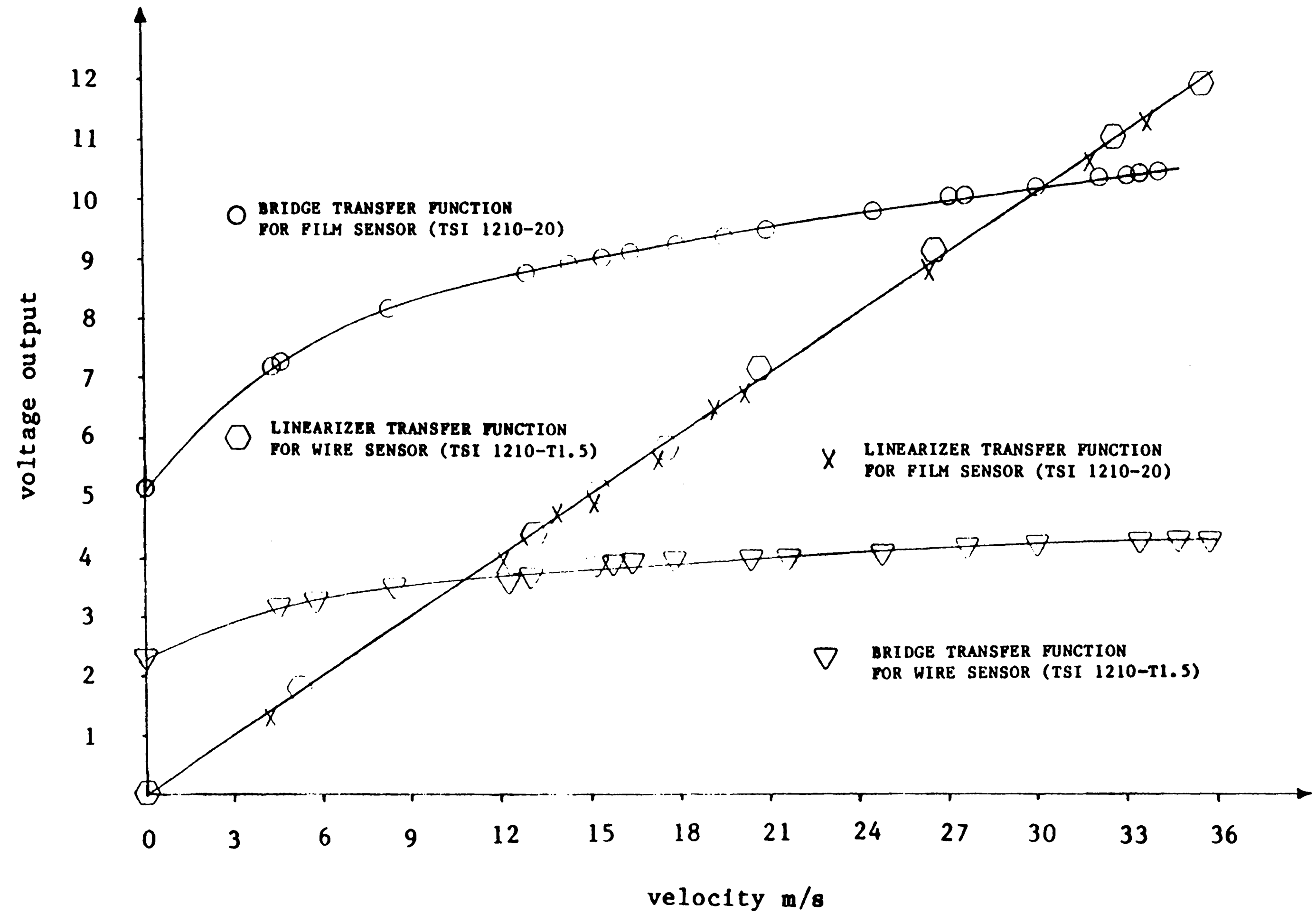

Figure 3-4 Comparison of Bridge and Linearizer Transfer Functions.

frequencies. Quantifying what is meant by lower frequencies is difficult for it depends on the objective of the experiment and is a subjective criterion.

In any case a filter cut-off frequency must be imposed in order to reduce this broad band signal to an acceptable band width for the Nyquist criterion to be met. In practice, meeting this criterion is not enough: typically, sampling rates are in the 3 to 4 times Nyquist range. This oversampling gives a more conservative setting.

The Zonic filter used is a ten-pole filter which provides a -60 decibel per octave roll-off or -200 dB/decade. The available cut-off settings were 6 kHz and 15 kHz. The 15 kHz setting is the highest that could be used with the 50 kHz maximum sampling rate of the Data 6000 while maintaining a sampling rate of 3.3 times the Nyquist rate.

In an effort to examine the frequency content of the turbulent boundary layer, a FFT was done using a low-pass setting of 15 kHz and a sampling frequency of 40 kHz (sampling at 2.7 Nyquist). The FFT output plotted on a linear scale is shown in Fig. 3-5. This plot shows very little signal content beyond 6 kHz. The sharp drop in the curve is not due to the filter since the cut-off was set at 15 kHz.

To emphasize the lower frequencies the next available lower setting of 6 kHz was used with a sampling frequency of 20 kHz (sampling at 3.3 Nyquist). This FFT output also plotted on a linear scale gives the result seen in Fig. 3-6.

Some information at the higher frequencies is lost by low-passing at 6 kHz: however, this loss was judged acceptable and a higher resolution is attained in the lower region.

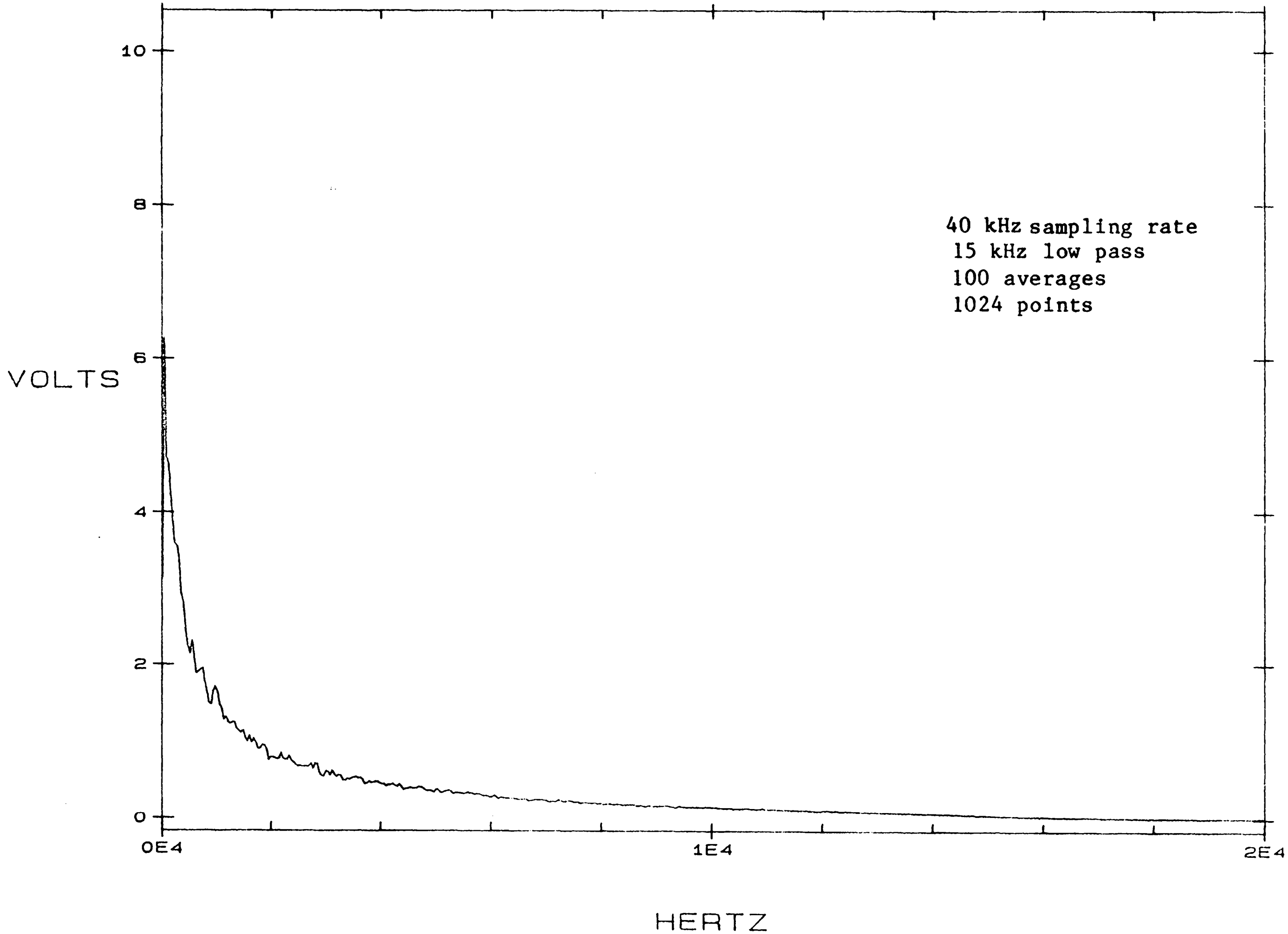

Figure 3-5 Turbulent Boundary Layer Spectrum Using a 15 kHz Low Pass Filter.

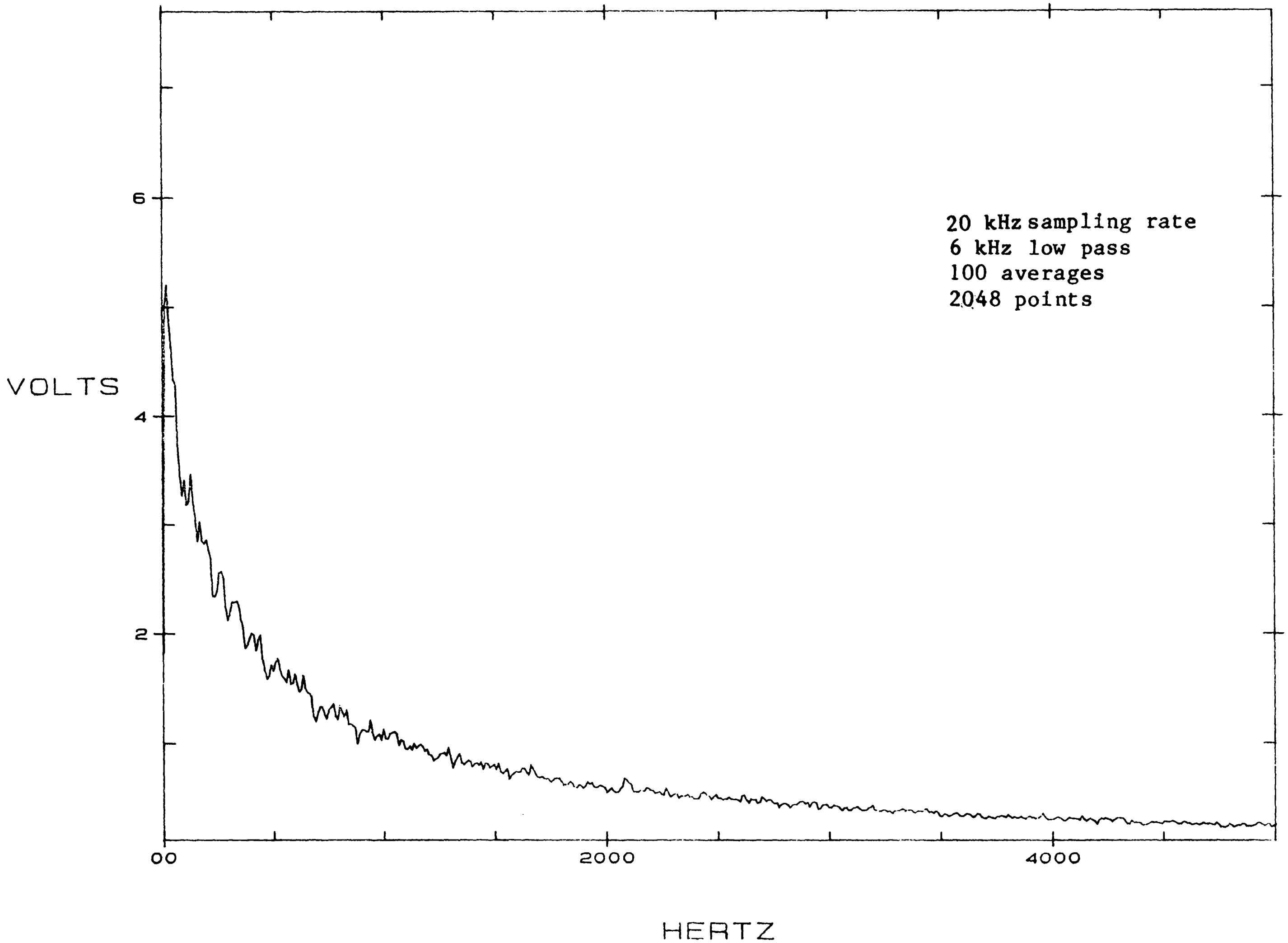

Figure 3-6 Turbulent Boundary Layer Spectrum Using a 6 kHz Low Pass Filter.

3-6 Averaging

The Data 6000 was set to collect 1024 data points per data string, i.e., 1024 points were sampled before any mathematical operation was performed. The discrete Fourier transform of a data record from a random process represents only one estimate of the frequency content of the process. A better estimate of the frequency content is obtained by frame to frame averaging of a number of frequency content estimates. This is referred to as "ensemble averaging". The Data 6000 has the capability of performing such averaging for a specified number of estimates [10]. The larger the number of estimates averaged, the better the spectral estimates and the smoother the result. The number of averages used throughout this experiment was 100. This choice provided sufficiently clear images (the peak of 6 kHz in Fig. 3-2 is clearly seen) for a reasonable computational penalty of 45 seconds. Figure 3-7 shows typical results for 500 averages for comparison with Fig. 3-2.

This plot shows a definite improvement in curve smoothness and signature clarity that comes with the smaller variance from the larger number of averages. However, this improvement was judged not worth the computational penalty of approximately 4 minutes.

3-7 FFT and Window

As stated by Kay [11], the spectrum of discretely sampled processes is usually based on procedures employing the Discrete Fourier Transform (DFT) implemented in a Fast Fourier Transform (FFT). This approach to spectrum analysis is computationally efficient and produces reasonable

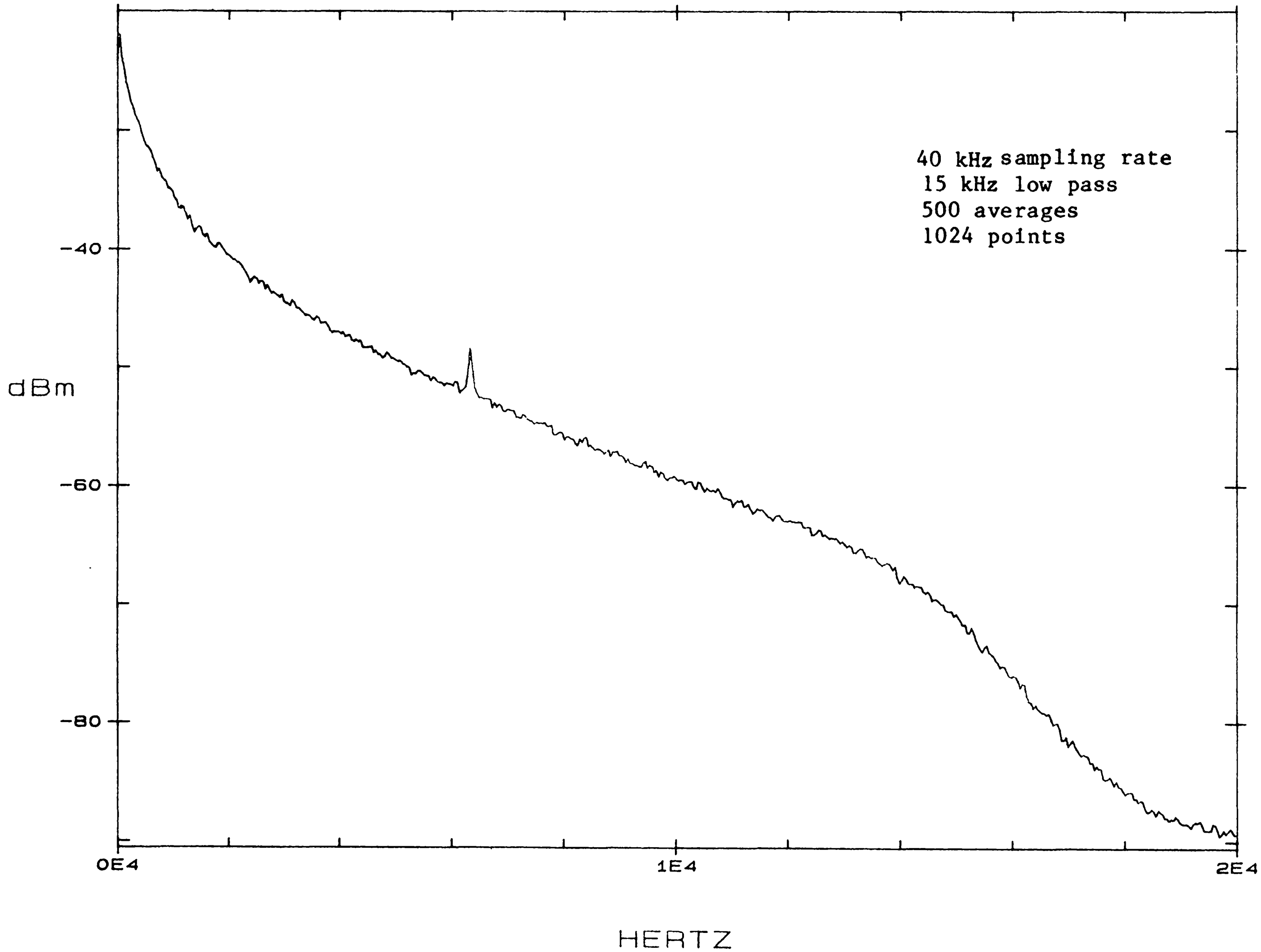

Figure 3-7 Nonlinearized Film Response After 500 Averages.

results for a large class of signals. In spite of these advantages, there are several inherent performance limitations of the DFT approach. The most prominent is that of frequency resolution, i.e., the ability to distinguish the spectral responses of two or more signals. This frequency resolution limitation is related to the implicit windowing of the data that occurs when processing with the DFT. Windowing manifests itself as "leakage" in the spectral domain. Weak frequency contributions can be masked by leakage from stronger frequency contribution.

The window or weighting function that was used in this work was the Hanning window. The .FFT output was plotted on a linear scale emphasizing the lower frequencies.

3-8 RMS Integrating Constant

The Disa type 55D35 RMS voltmeter is designed for measurement of the true root-mean-square value of AC voltages [12]. This ability ensures a high degree of accuracy even in measurements with noise or in pulse trains.

The principle underlying this voltmeter is based on the definition of the true root-mean-square value of an AC voltage, i.e.,

$$e_{rms} = \left(1/T \int_o^T e^2 dt \right)^{1/2}$$

The integration constant T is selected on the front panel and has six values covering a range from 0.3 seconds to 100 seconds. Normally, the integration constant used is the shortest one yielding a stable meter reading. A 30 second integrating interval was selected, and this setting gave repeated readings that varied by only 1-2 percent.

3-9 Immersion of the Probe in the Flow

The tunnel test section is 0.61 m high while the maximum height from the floor that data was recorded was 0.155 m. Entering the flow from the floor with a short probe might seem more desirable than entering from the roof with a substantially longer probe. However, probe entrance from the floor necessitated major tunnel modifications and would have required manual repositioning for every data station. Such a procedure would be both time consuming and tedious. On the other hand, entering from the roof only required a roof piece with a slot along the centerline of the tunnel. Further, an automated traverse could be used for positioning the probe far more accurately than could be expected with manual positioning that floor entry would have required.

Probe entry through the tunnel roof was chosen. In order to determine whether the spectral results of the wire would be independent of floor or roof entry of the probe, a comparison was made. A smoke injection port was used to insert the probe through the floor. The spectrum of this linearized signal is shown with a logarithmic scale in Fig. 3-8 and with a linear scale in Fig. 3-9. The wire sensor was then placed at the same physical location with the longer probe entering from the roof. This signal's spectrum is shown in Figs. 3-10 and 3-11. The

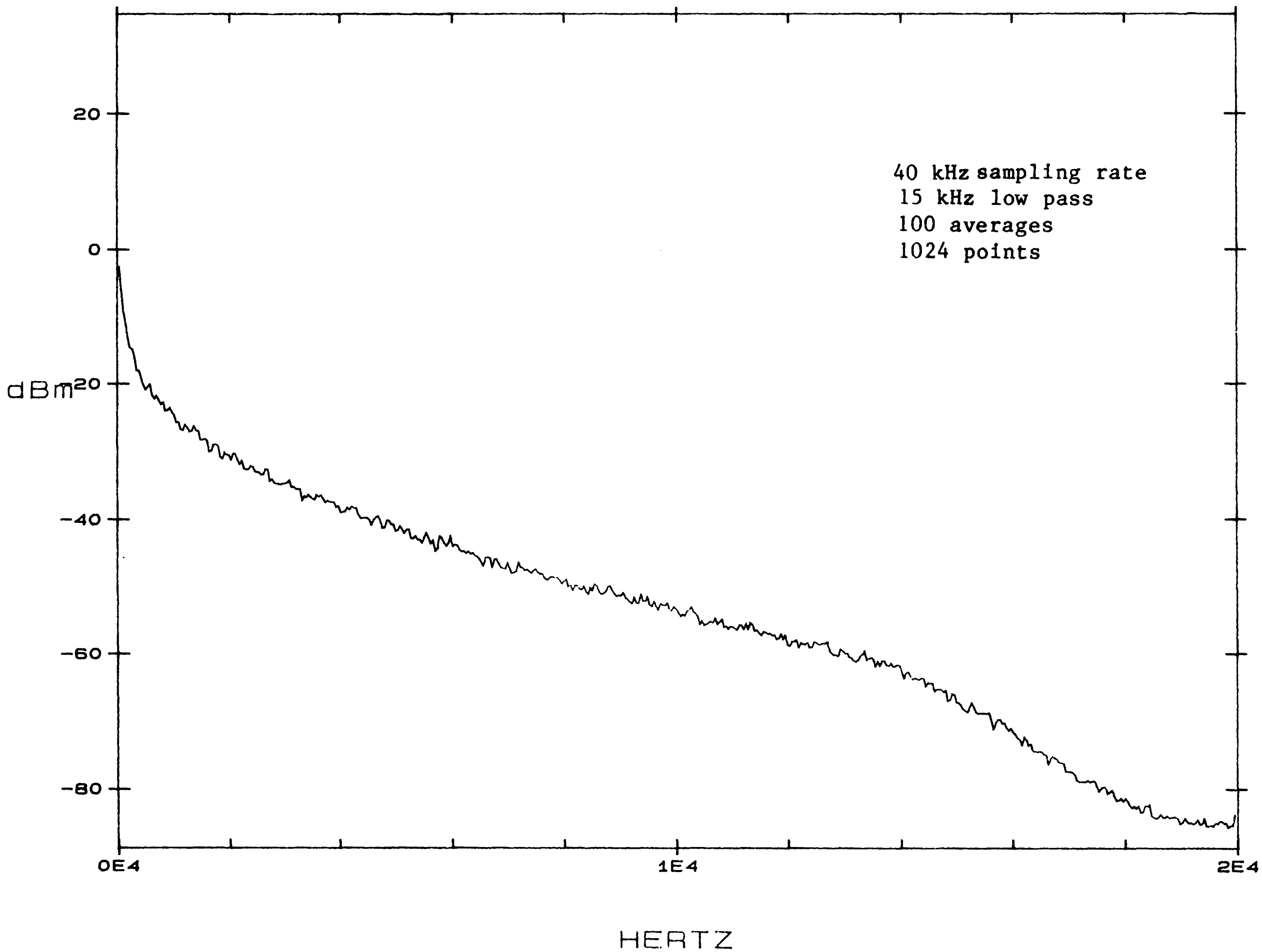

Figure 3-8 Wire Spectrum of Probe Inserted Through the Floor, Logarithmic Scale

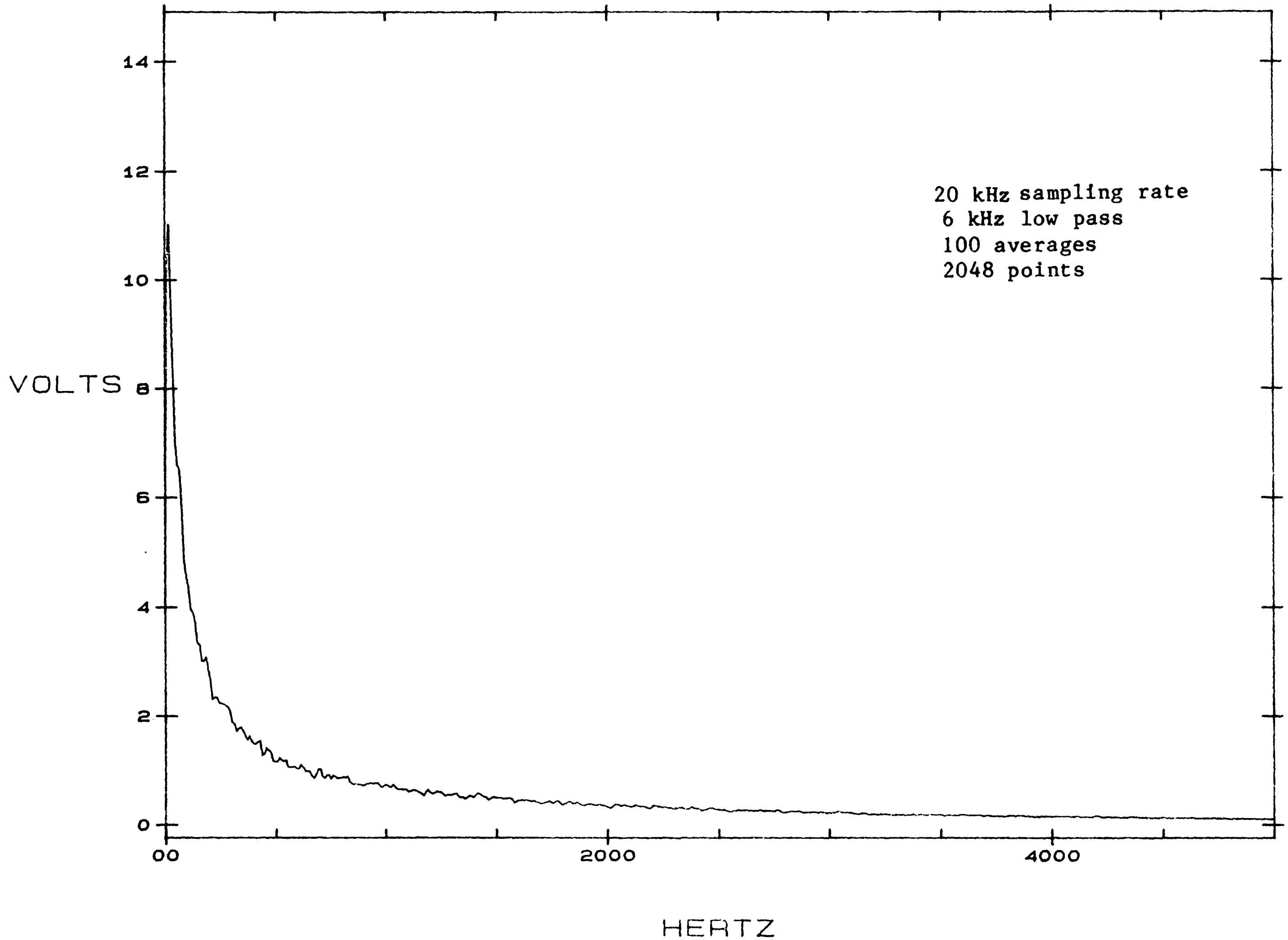

Figure 3-9 Wire Spectrum of Probe Inserted Through the Floor, Linear Scale

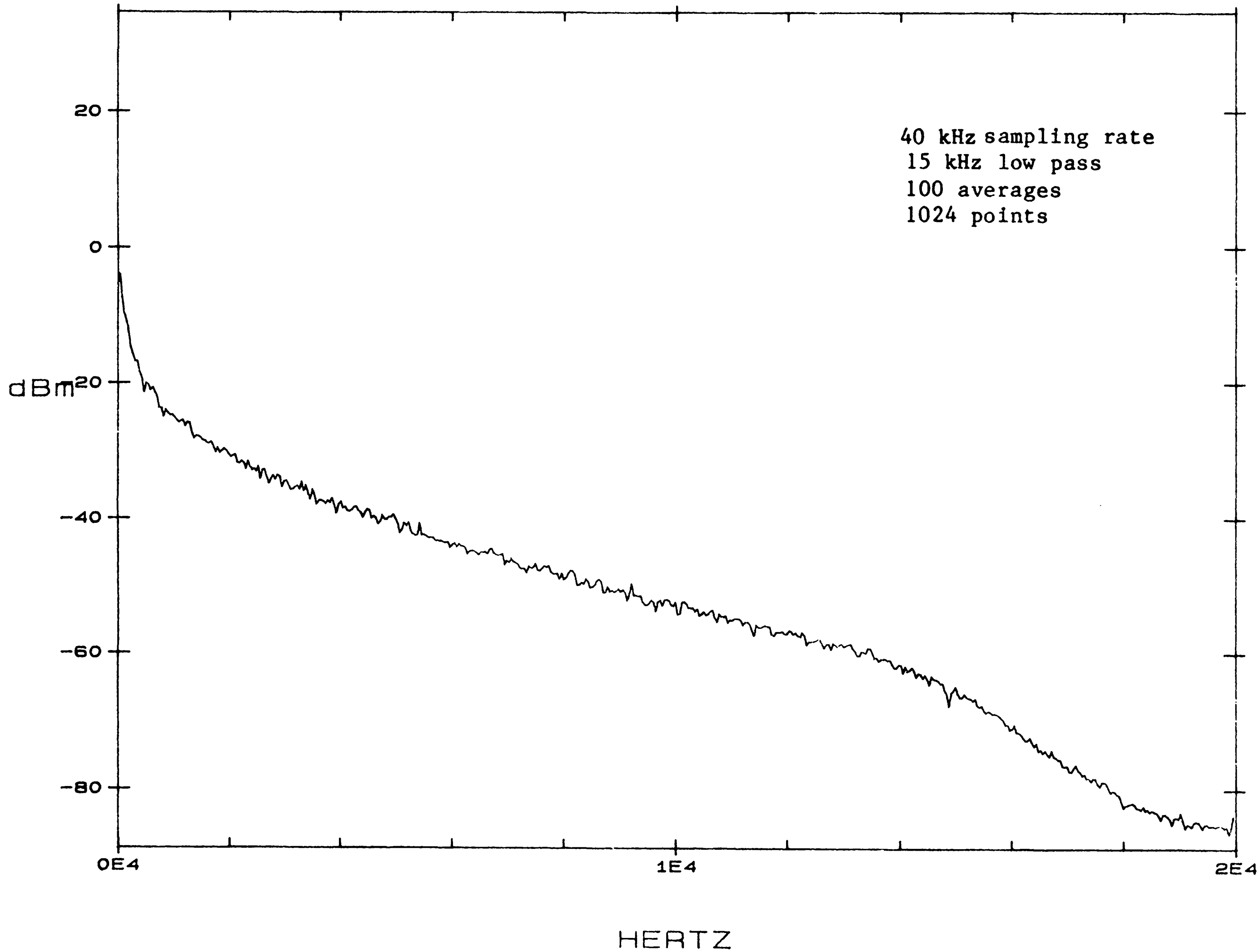

Figure 3-10 Wire Response of Probe Inserted Through the Roof, Logarithmic Scale.

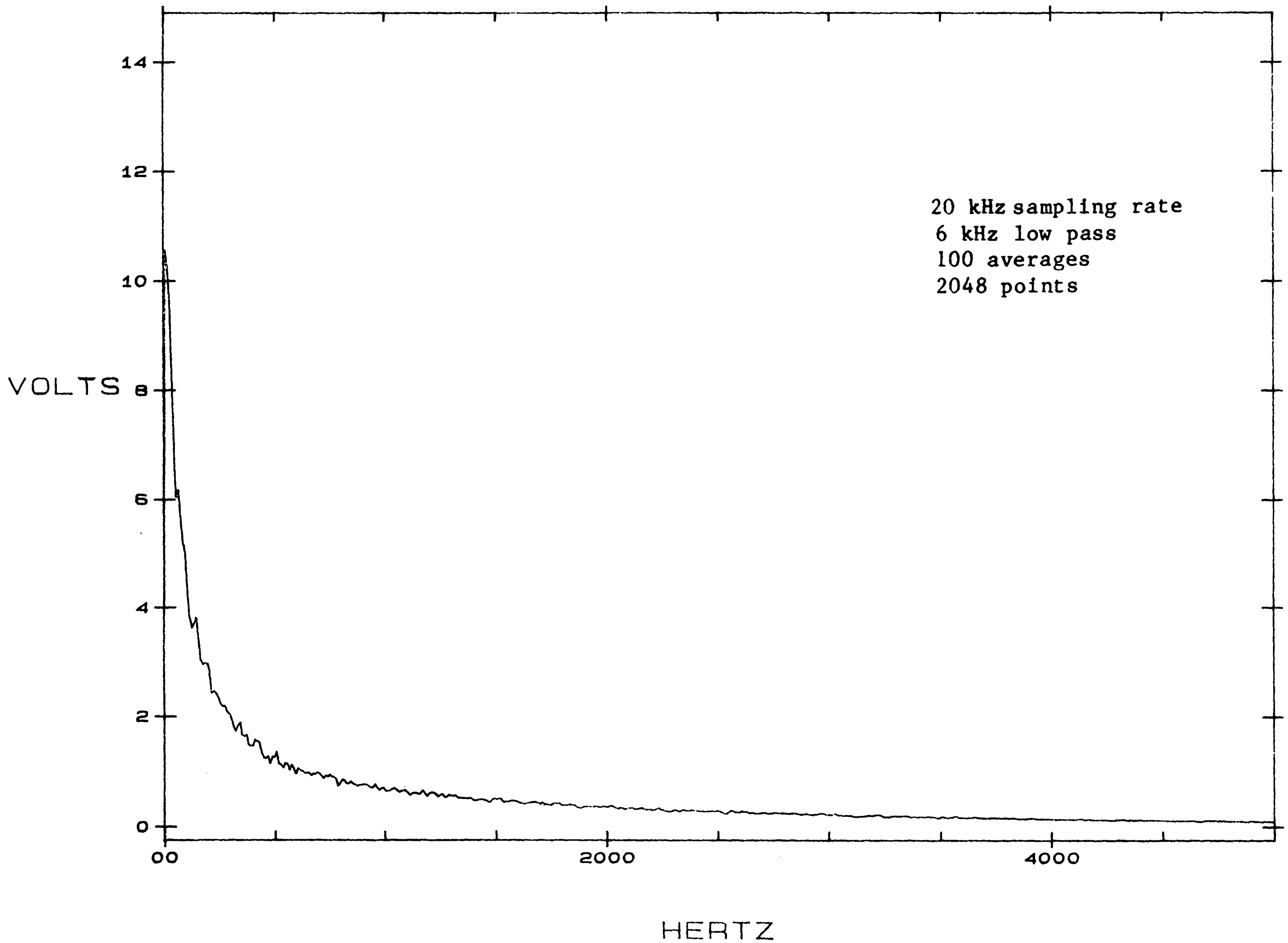

Figure 3-11 Wire Response of Probe Inserted Through the Roof, Linear Scale.

frequency range chosen for the logarithmic scale plots extends to 20 kHz as compared to 5 kHz for the linear scale plots. This permits an examination of the spectrum beyond 5 kHz (at the expense of resolution) which is totally suppressed on a linear scale.

There was a small visible oscillation of the longer probe, probably due to shedding off the stem. The probe Reynolds number based on the probe diameter and local velocity was

$$Re = \frac{Ud}{\nu} = \frac{(21.3 \text{ m/s}) \;\; 0.0127 \text{ m}}{1.95 \; 10^{-5} \; \text{m}^2/\text{s}} \simeq 14000$$

Using the Reynolds-Strouhal correlation found in [7], this Re of 14000 indicated a corresponding Strouhal number of 0.2. Using the procedure of Section 3-2, the estimated shedding frequency was

$$f = \frac{StU}{d} = \frac{(0.2) \;\; 21.3 \text{ m/s}}{0.0127 \text{ m}} = 335 \text{ Hz.}$$

Figures 3-10 and 3-11 do not show any spike at this frequency. Furthermore, the hot-wire RMS values were essentially identical whether the probe was inserted from the floor or through the roof. It was assumed that this small visible oscillation did not introduce any significant error and could be neglected relative to the flow velocity fluctuations.

3-10 Grid Selection

A grid matrix had to be defined for the data stations. Physically the extent of the measurements on the plane of symmetry were dictated by:

(1) The mean flow velocity data taken with the same body [4].

(2) The smoke visualizations.

The mean flow data was used to identify the mean positions of separation and the vortex center. The smoke visualization gave information about the excursions from these mean positions and also about the time-resolved size of the horseshoe vortex. This information has been summarized in Fig. 3-12.

The grid had a fine mesh in the vortex region and close to the tunnel floor. However, upstream of separation and above the vortex core, a coarser grid spacing was selected. An irregular grid spacing was adopted to map a region up to approximately 180 mm upstream of the body and up to 155 mm above the floor. Due to the different geometries of the fillets some data stations were not available. For the flows with no fillet, the large triangular fillet, and the vortex generator strip, additional data was taken between 2 and 6.3 mm from the floor. The grid systems used in each case are shown in Figs. A-1 through A-6 of Appendix A.

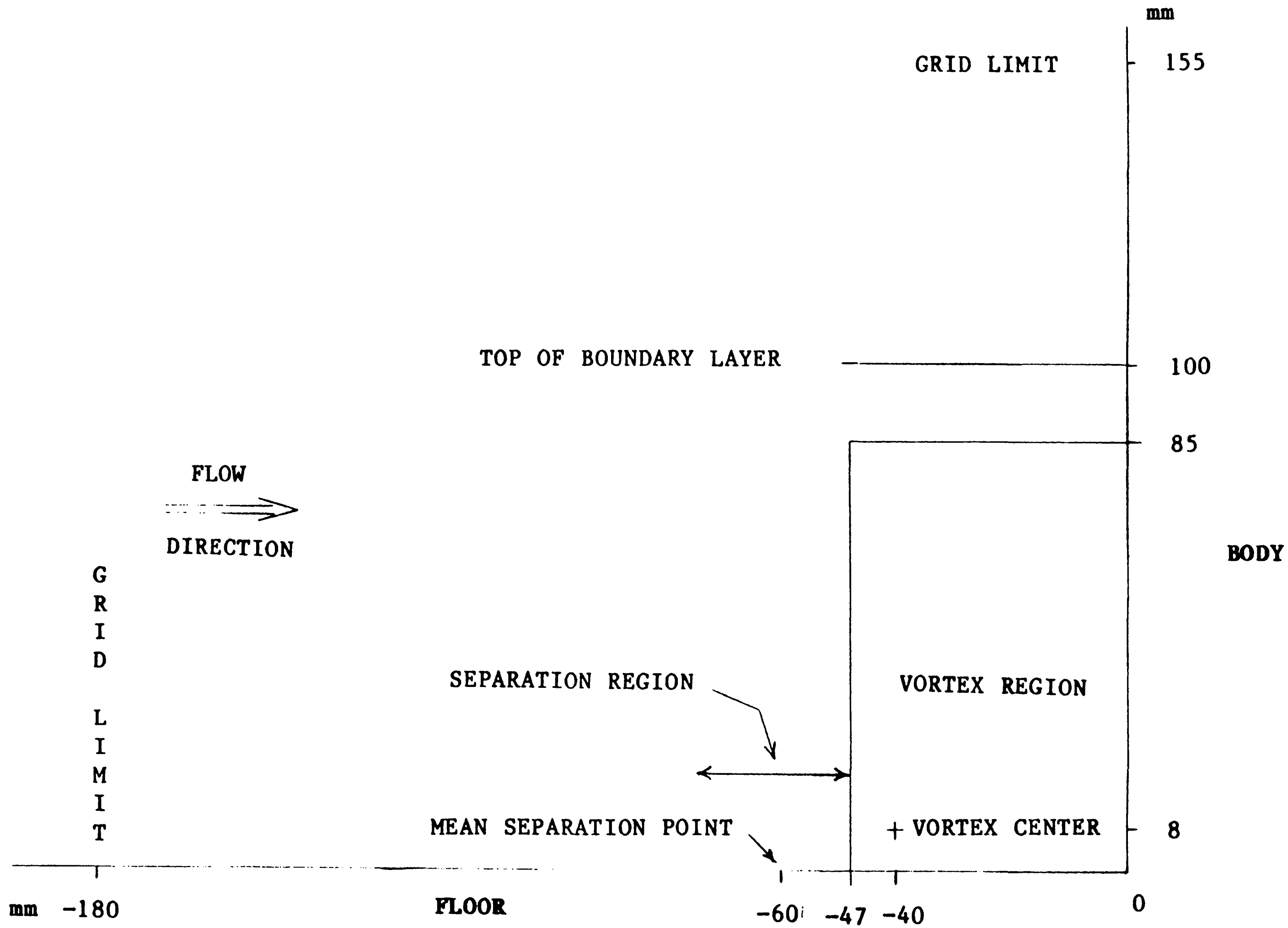

Figure 3-12 Information used in Defining the Grid Limits.

4. DATA REDUCTION AND INTERPRETATION

4-1 RMS Data

The RMS data gathered characterized the flow field as seen by a single hot-wire sensor. This sensor was calibrated in the x direction, as defined in Fig. 1-2. In effect this calibration was assumed to hold for both the x and y directions. On the symmetry plane the contribution of the mean velocity component along the sensor length was assumed to be zero and the fluctuating component effect is usually neglected. Away from separation and the vortex core where the dominant mean velocity is in the x direction, the single sensor measures the instantaneous velocity component in the x direction.

In the separation and vortex regions the single sensor measures some combination of the x and y components of the instantaneous velocity.

The RMS data could be reproduced to within ±10 mvolts with typical data values ranging from 20 mvolts to 800 mvolts. In the background flow (upstream of separation and above the boundary layer) where the smaller RMS values occurred the 10 mvolt uncertainty represented a large percentage (as much as 50 percent). However, in the area of interest where the readings were between 500 mvolts and 800 mvolts the uncertainty was of the order of 1-2 percent.

4-2 Turbulent Velocity

The RMS voltage data can be converted to a RMS fluctuating velocity data by multiplying by the slope of the linearization curve. Figure 3-4 yields a slope of 3 m/s per volt.

4-3 Turbulent Kinetic Energy (e_t)

The single sensor output was taken to characterize the e_t of the plane of symmetry flow. Thus,

$$e_t = \frac{\bar{c}^2}{2}$$

where c is the fluctuating velocity that the single sensor responds to.

This e_t data at discrete x,y space locations were used to evaluate the total E_t content in the plane of symmetry. These discrete e_t values were taken as e_t density values identified with area increments of unit depth surrounding the data station. A numerical integration for the total E_t which was used was:

$$E_t = \left(\sum_i \frac{1}{2} \bar{c}_i^2 \times A_i \right) / \frac{1}{2} V_{th}^2$$

The summation is over the total number of data points (grid points) in each set. The area (A_i) is the rectangle of unit depth having a grid point as center and reaching mid-way between that grid point and its adjacent neighbors. Since the grid spacings were nonuniform, the rectangle sizes were also nonuniform over the data sets. The squared nominal tunnel throat velocity V_{th}^2 (22.3 m/s) was used to nondimensionalize all the e_t data. This in effect was an area weighted sum of nondimensionalized discrete turbulent kinetic energy density values.

The uncertainty of ±10 mvolts in the RMS data corresponds to an uncertainty for the nondimensionalized turbulent kinetic energy values of about 0.02, with typical reported values ranging from 0.07 to 100.

5. RESULTS AND DISCUSSION

5-1 Contour Maps

The RMS data were converted to turbulent kinetic energy density data as described in Section 4-3. These e_t data were used to generate energy contour maps. Surface II software [13] was used for the plots of Figs. 5-1 through 5-6. Zero energy was assigned to the solid surface boundaries (floor and cylindric body) of these plots.

At any x location the energy generally increases as y decreases. This tendency to peak near the floor in effect means that the turbulent energy increases in moving from the outer flow towards the floor. This behavior is seen up to approximately 4 mm from the floor, below which the energy decreases toward the solid boundaries.

For all six cases the largest turbulent kinetic energy values occurred in the regions of the vortex core and separation. By comparison, above the boundary layer ($y \simeq 100$ mm), the turbulent kinetic energy was very low, dropping by over three orders of magnitude with respect to the highest core values.

Using the no-fillet map of Fig. 5-1 as reference, the large circular fillet results in Fig. 5-2 show an increase in the turbulent kinetic energy with significant increases in the length of the contours labelled 60 and 80 in the -x direction. Additionally, a higher energy contour labelled 100 became visible. The flow above y=50 mm did not appear to be affected by this large fillet.

Figure 5-3 indicates that the small elliptic fillet did not have any significant effect on the turbulent kinetic energy distribution.

The small circular fillet did not appear to affect the flow above y=20 mm as shown in Fig. 5-4. However, the contours labelled 60 and 80 were increased in size and a contour level labelled 100 could be seen. The effects of this fillet were similar to, although not as dramatic as, the effects of the large circular fillet shown in Fig. 5-2.

As shown in Fig. 5-5, the large triangular fillet shifted the entire contour figure in the -x direction, while smoothing the contours. This smoothing suggests a more orderly distribution of energy. Additionally, the sharp peaks in the turbulent kinetic energy around x = -60 mm and y = 90 mm for the smaller fillets do not appear with this large triangular fillet. This fillet appeared to have the largest effect in reducing the overall turbulent energy content of the junction vortex region, although it did create some local increases such as the contour level labelled 100. This observation is supported by the fact that a weak vortex structure was detected in the real time smoke visualizations. The physical displacement of the flow field caused by the fillet made comparisons somewhat difficult since corresponding x-y coordinates were in different flow field positions relative to this augmented body.

Figure 5-6 shows how the vortex generator fence caused the most significant increase in size of the high energy contours labelled 60, 80 and 100. The flow above y = 20 mm did not appear to be affected by the presence of the fence.

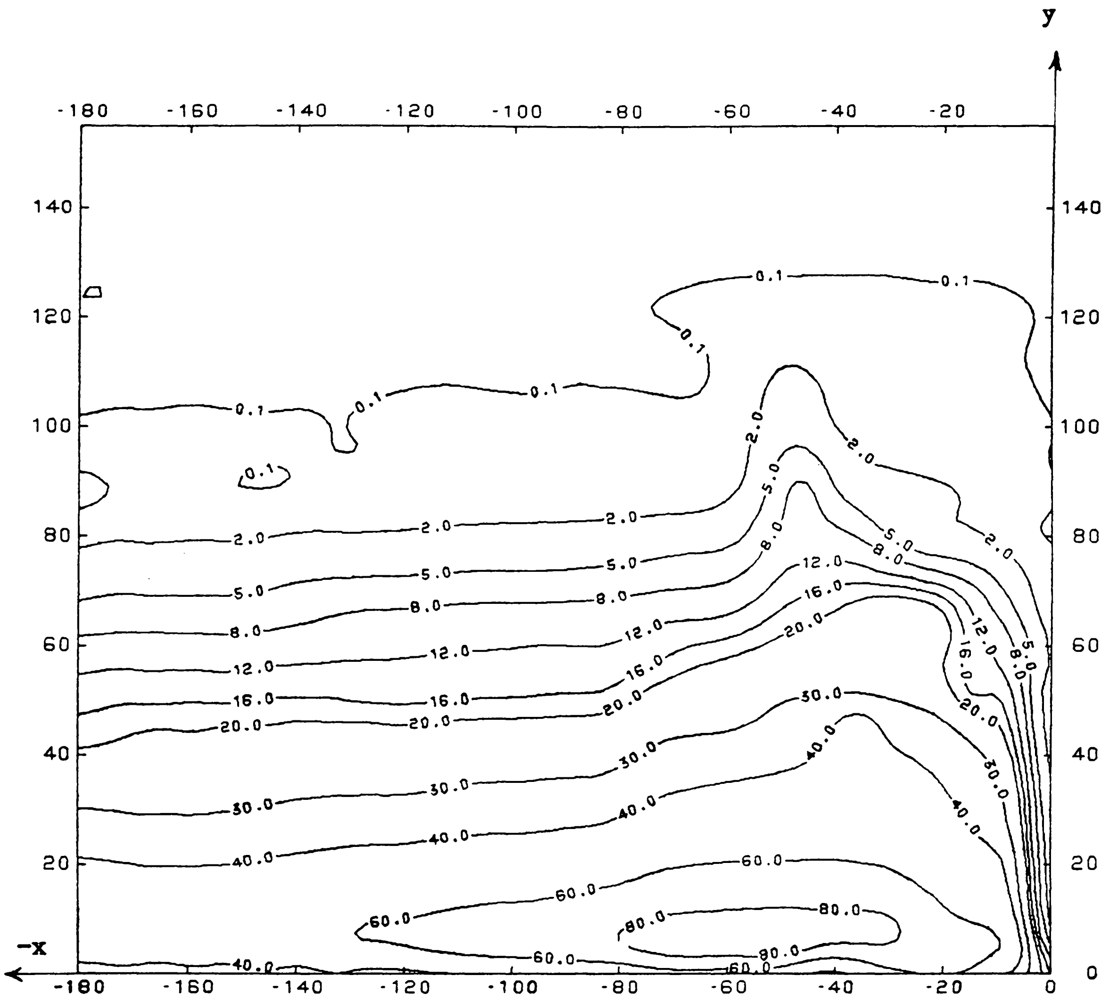

Figure 5-1 Nondimensionalized Energy Density Distribution for the No Fillet Case.

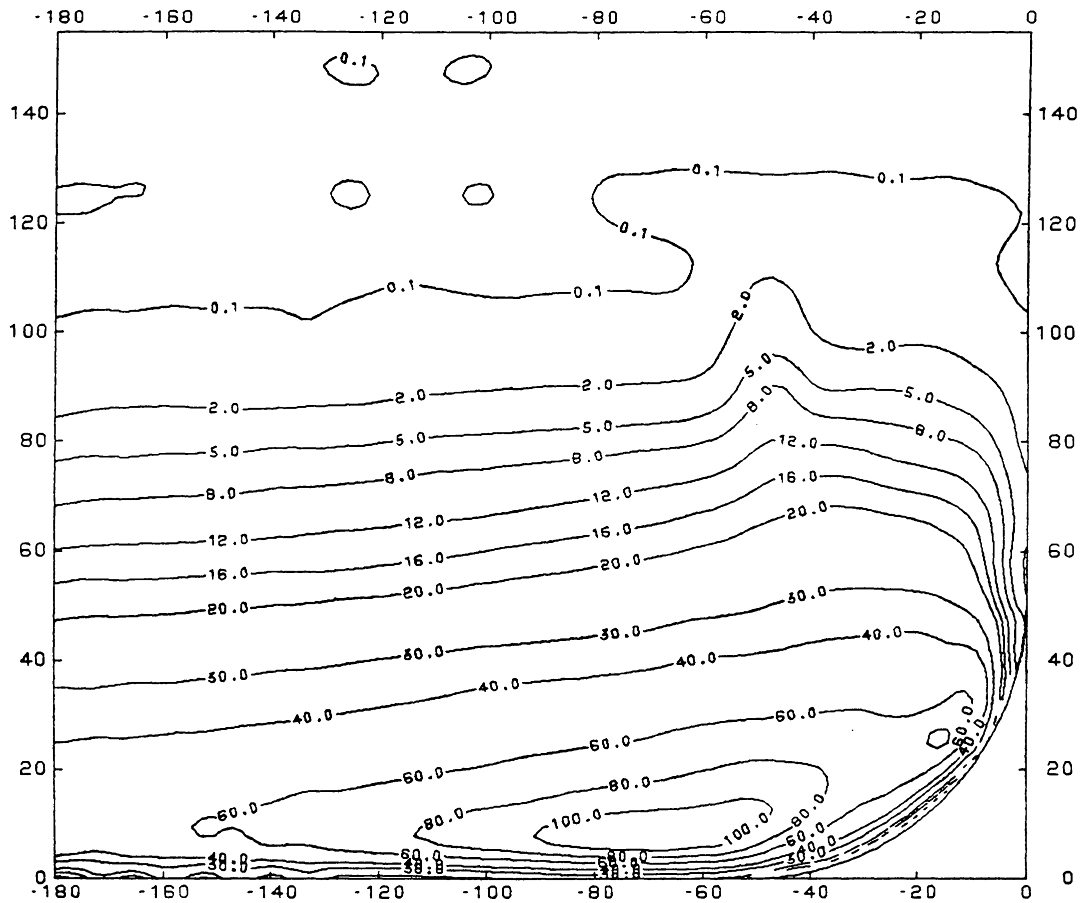

Figure 5-2 Nondimensionalized Energy Density Distribution for the Large Circular Fillet Case.

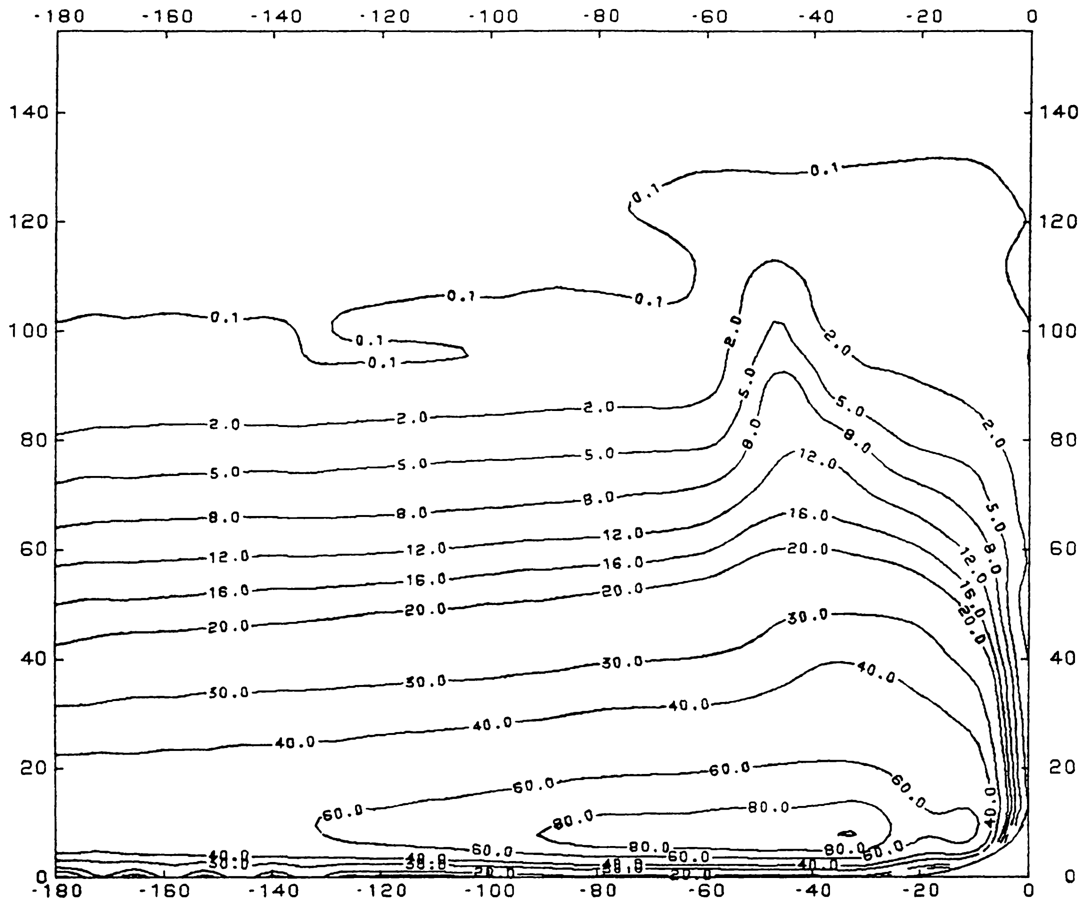

Figure 5-3 Nondimensionalized Energy Density Distribution for the Small Elliptic Fillet Case.

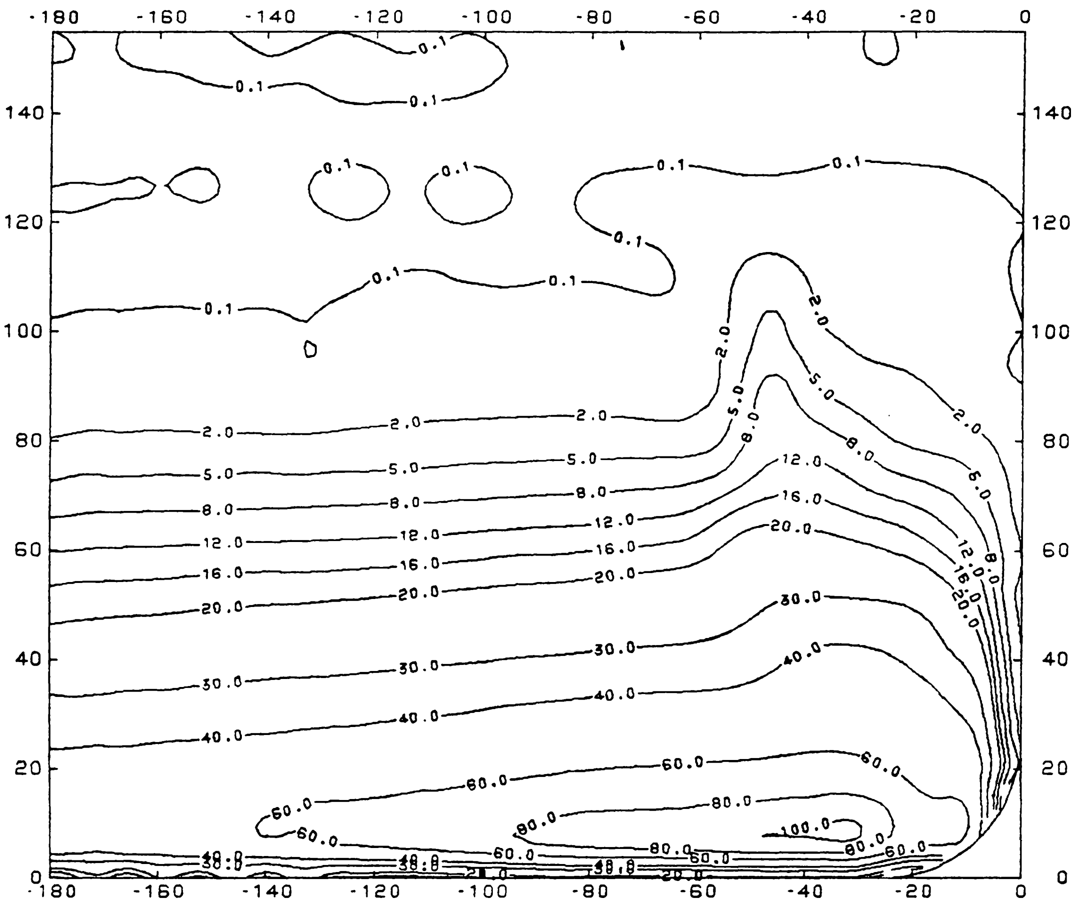

Figure 5-4 Nondimensionalized Energy Density Distribution for the Small Circular Fillet Case.

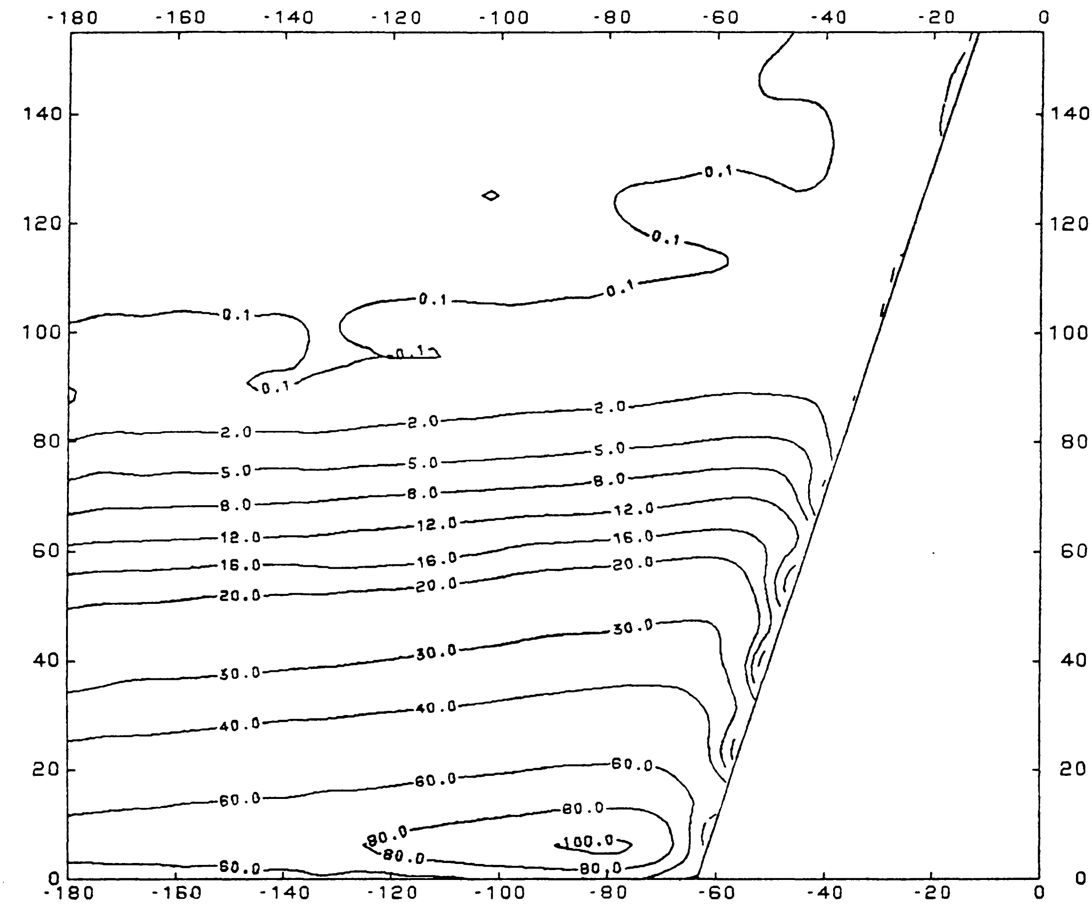

Figure 5-5 Nondimensionalized Energy Density Distribution for the Large Triangular Fillet Case.

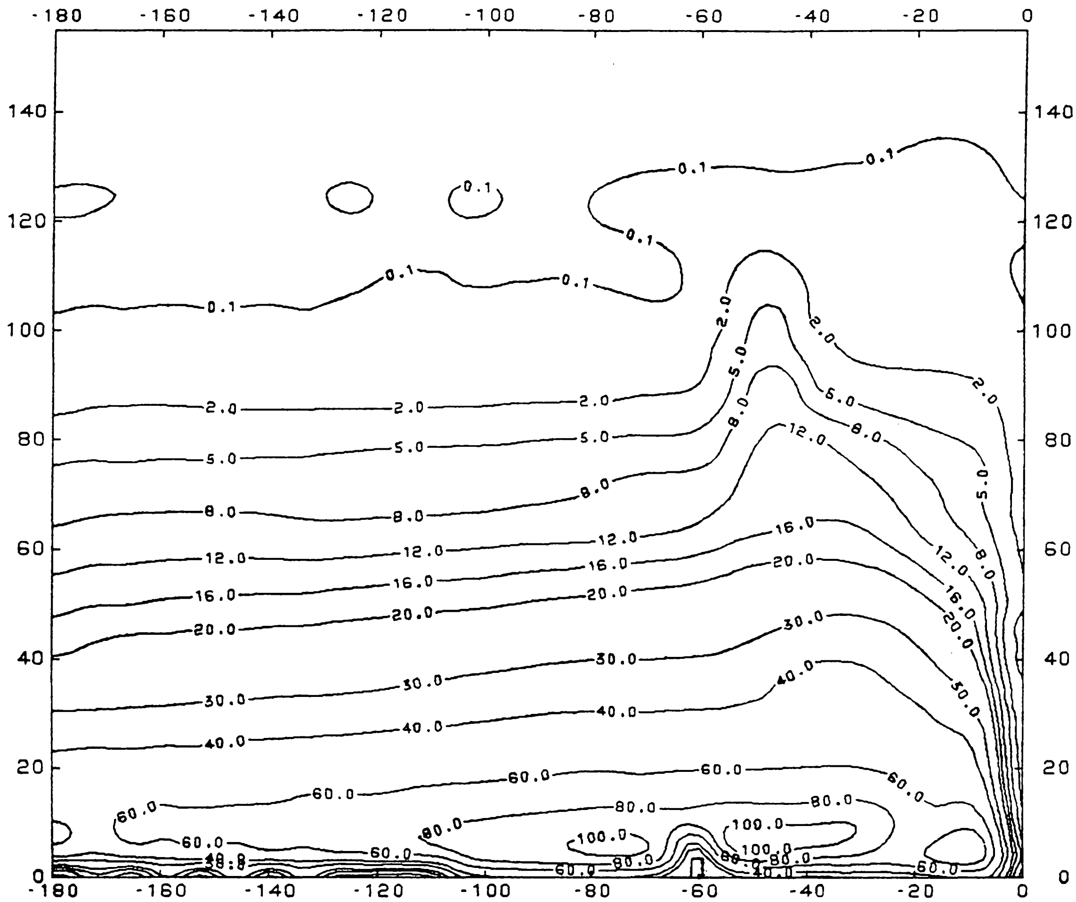

Figure 5-6 Nondimensionalized Energy Density Distribution for the Fence (Vortex Generator) Case.

In order to have a comparison of the six cases and to further identify changes in the effects of the fillets, the flow field boundaries needed to be more nearly identical. Three of the boundaries were clearly the same for all cases; the floor, the body, and the horizontal outer flow boundary. Thus, the choice for the grid limit in the y direction was adequate. The fourth boundary, the vertical upstream line proved to be too close to the body. The slopes of most contours on that face should ideally be near zero (as for the no fillet case) so that the energy distribution could be presumed constant further upstream. It is important to have nearly identical background flow on the boundaries of the integration region to be certain that the entire junction vortex flow is captured in the area to be studied. Examining the large triangular and large circular fillets it was judged that an extension of about 25.4 mm in the -x direction would allow for the slopes of the contours of these plots to approach zero.

In summary, the contour maps suggest that only the large triangular fillet was able to reduce the overall turbulent kinetic energy. The small elliptic fillet did not produce any noticeable effect. The fence, the large circular, and the small circular fillets resulted in an increase of local turbulent kinetic energy values.

5-2 3-D Plots

Using the same nondimensionalized e_t data as for the contour maps, three-dimensional topographic plots were also generated to display the e_t distribution. These plots, shown in Figs. 5-7 through 5-12, show the

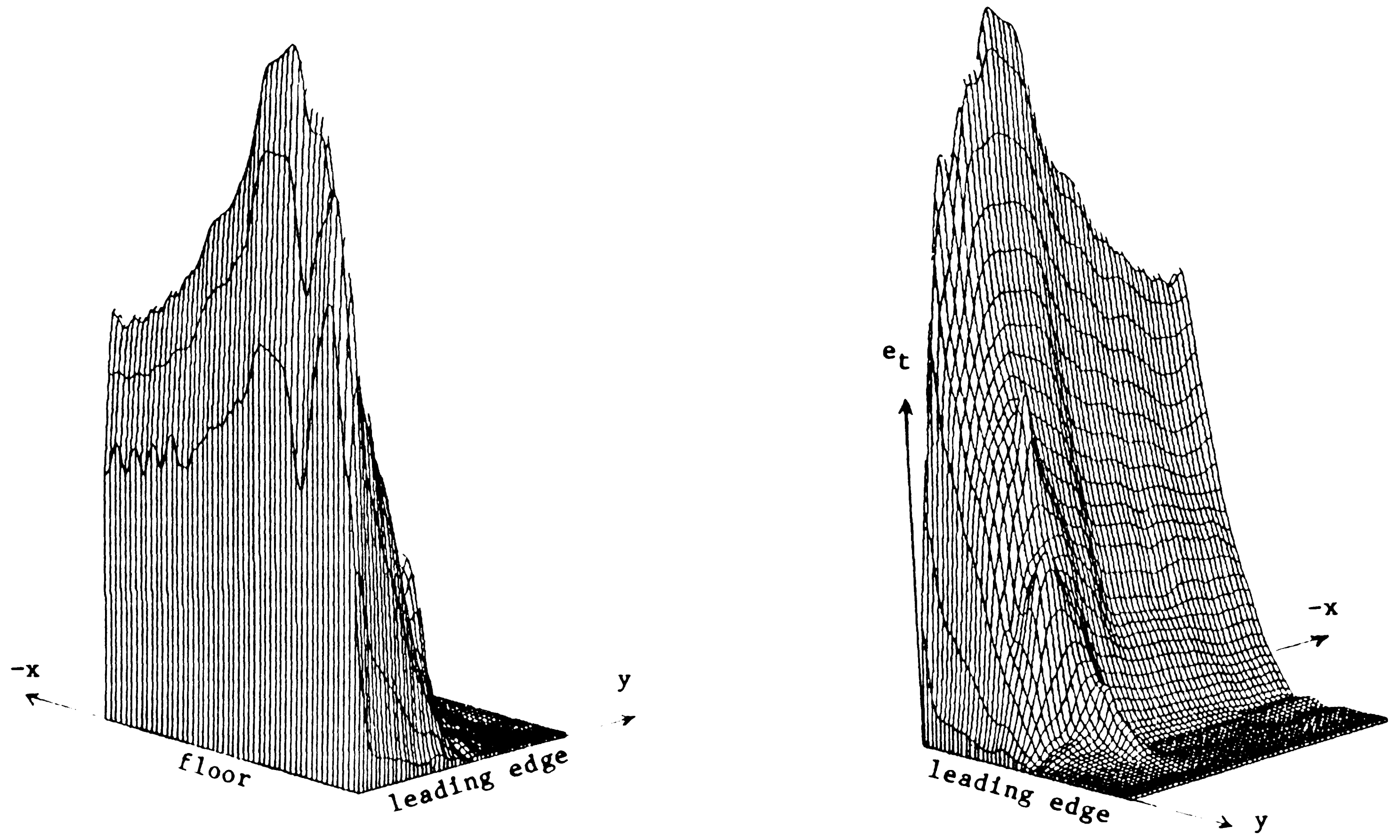

Figure 5-7 3-D Representation of e_t Distribution for the No Fillet Case.

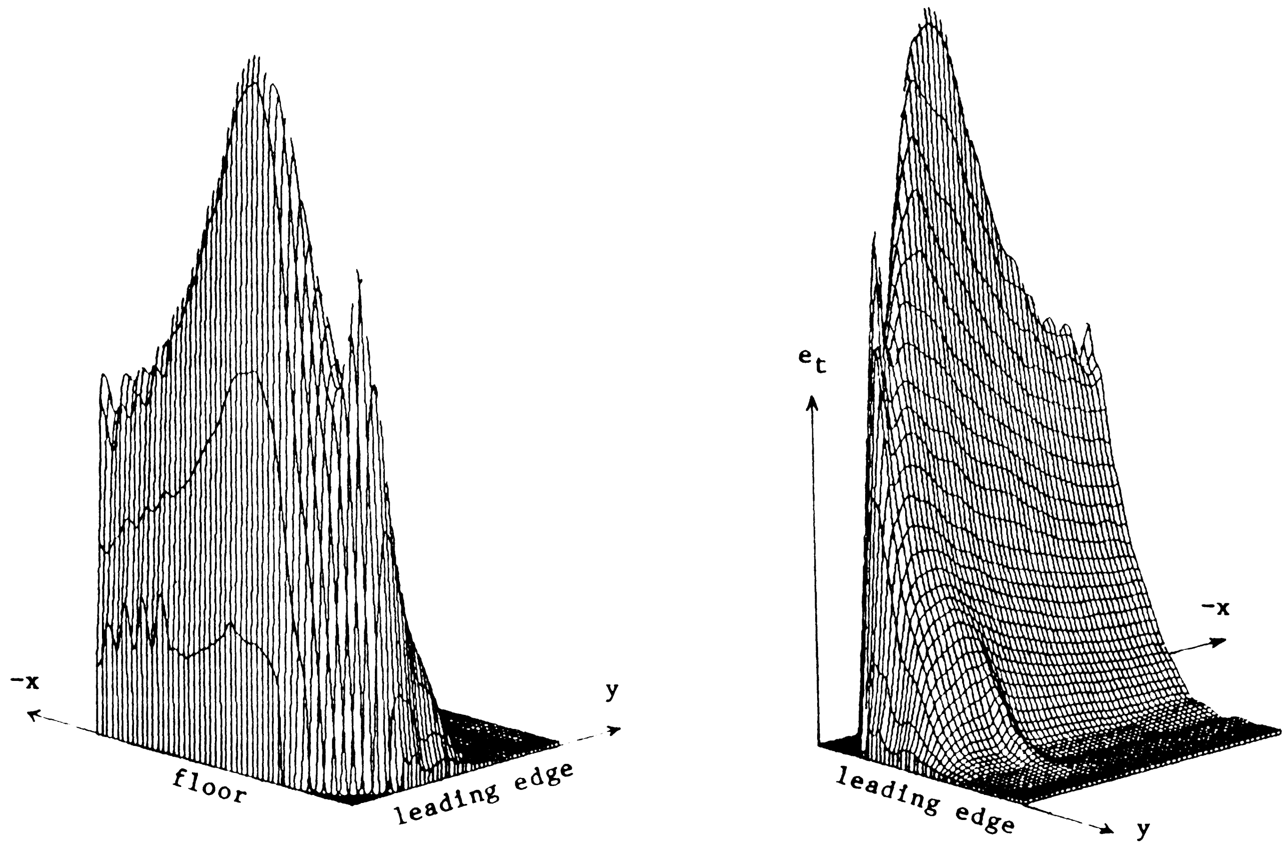

Figure 5-8 3-D Representation of e_t Distribution for the Large Circular Fillet Case.

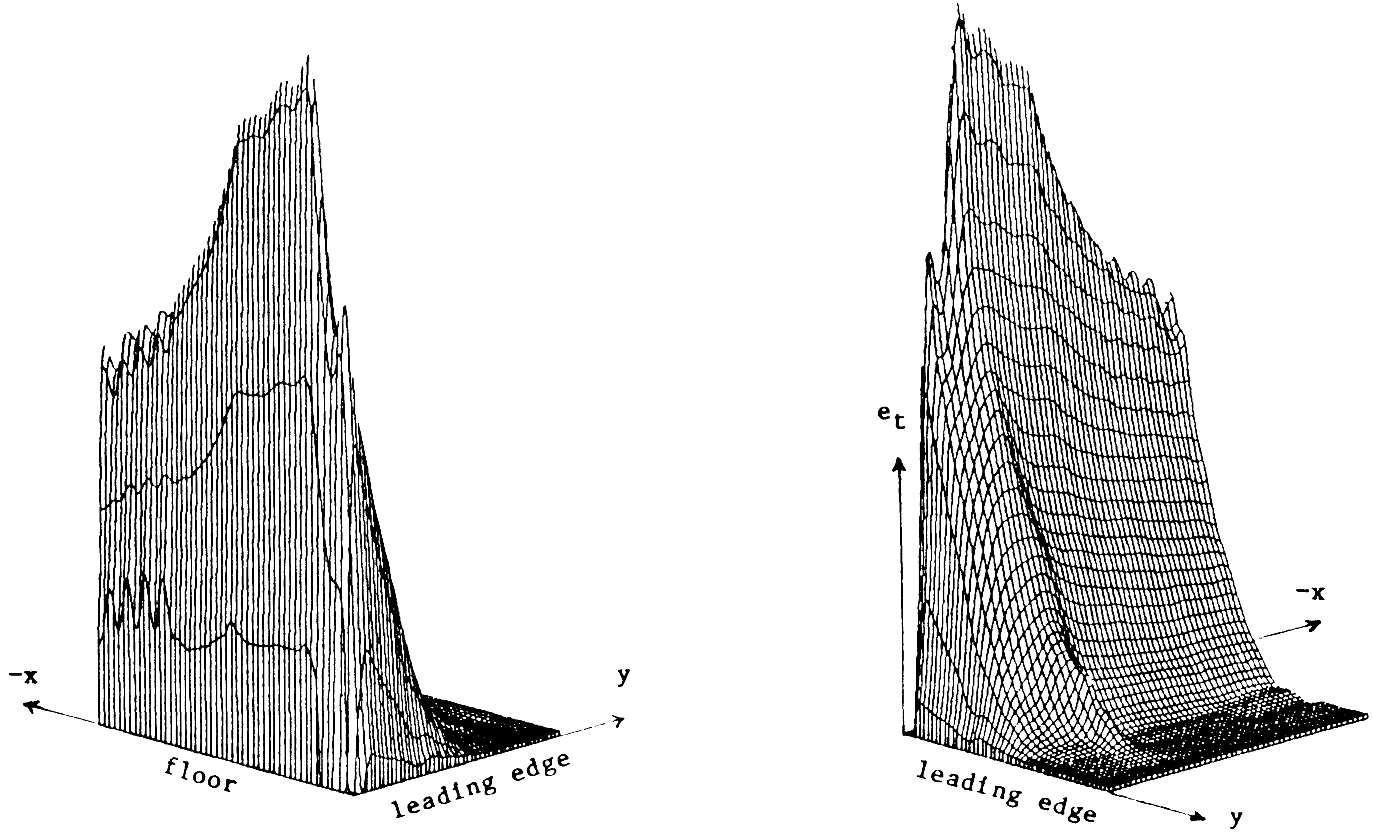

Figure 5-9 3-D Representation of e_t Distribution for the Small Elliptic Fillet Case.

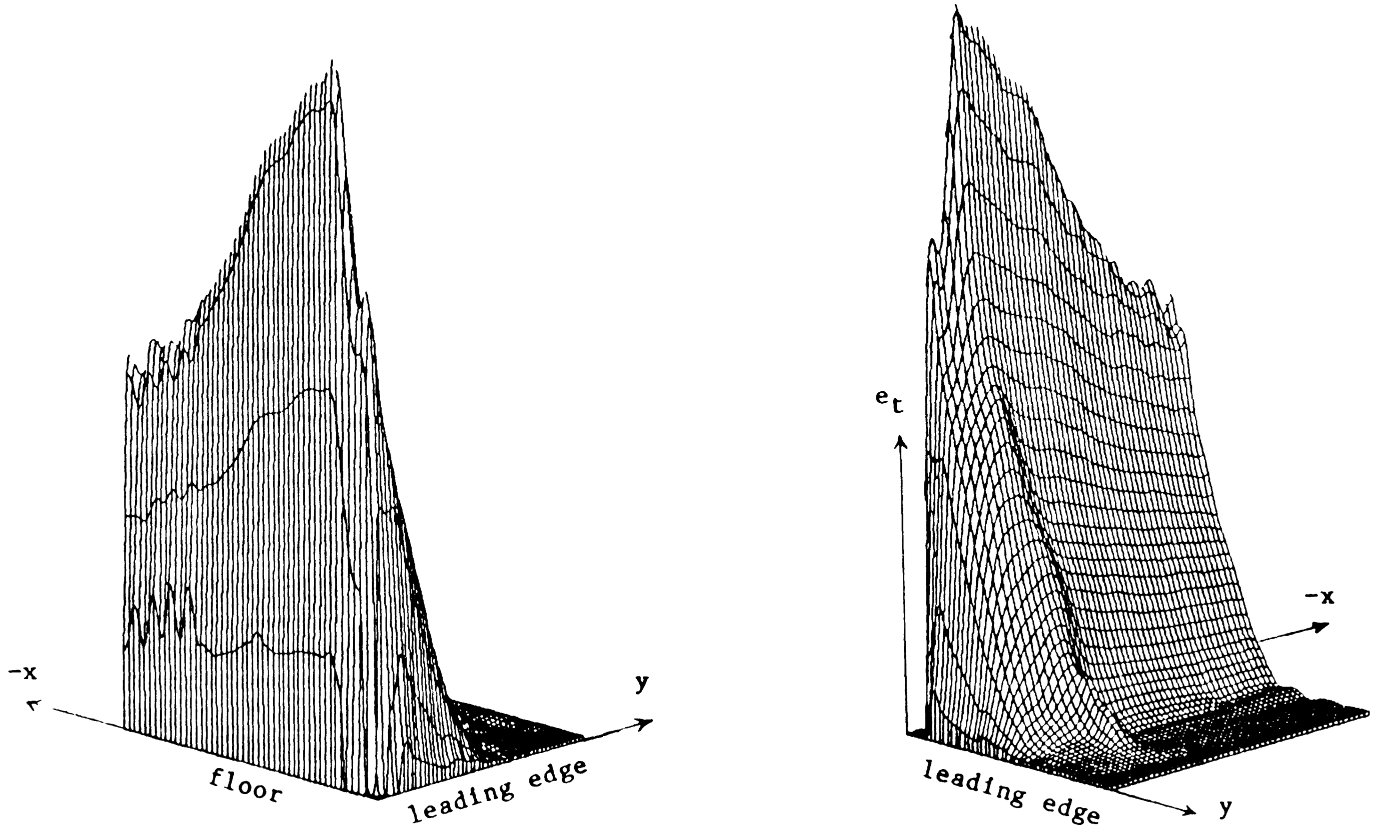

Figure 5-10 3-D Representation of e_t Distribution for the Small Circular Fillet Case.

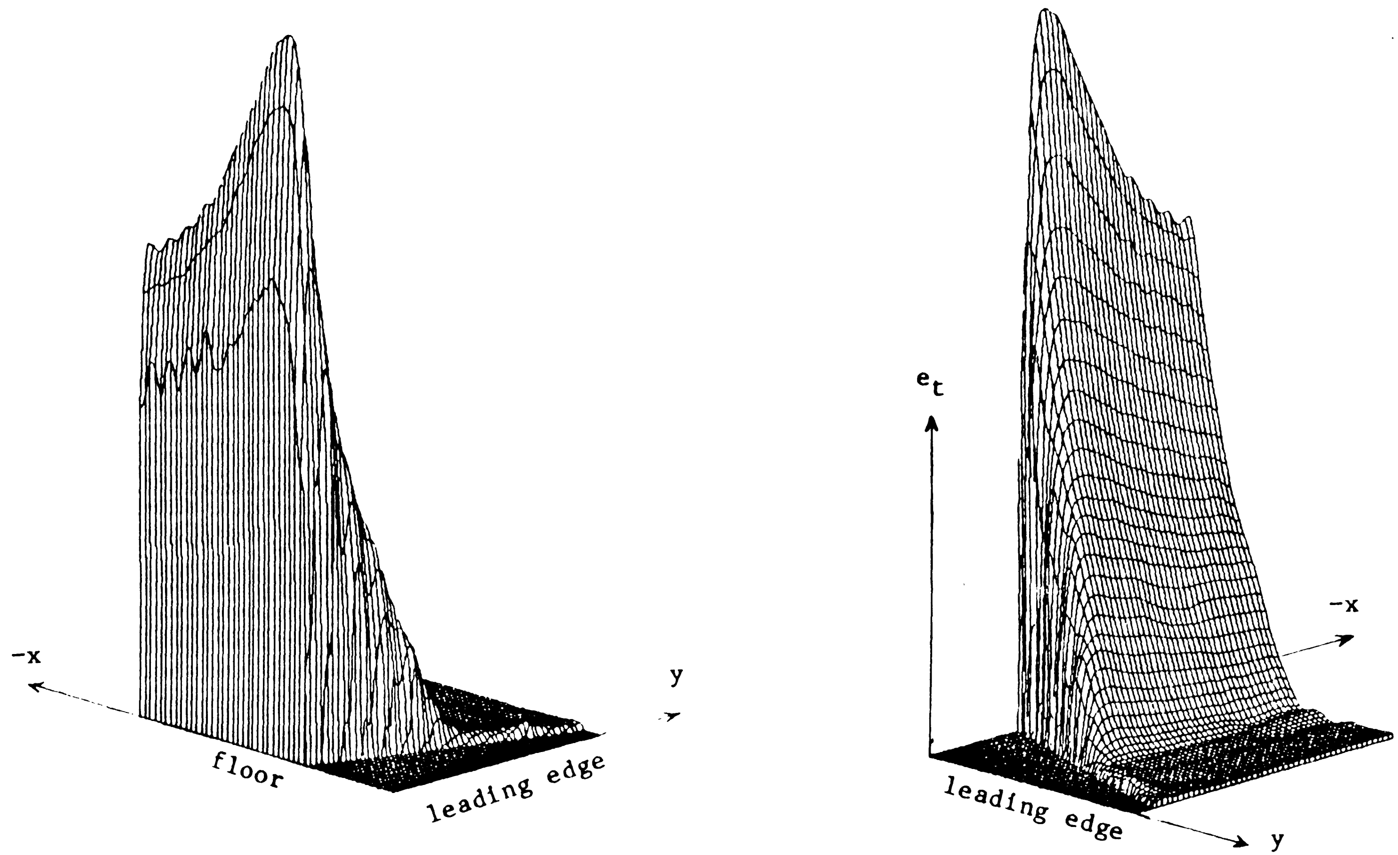

Figure 5-11 3-D Representation of e_t Distribution for the Large Triangular Fillet Case.

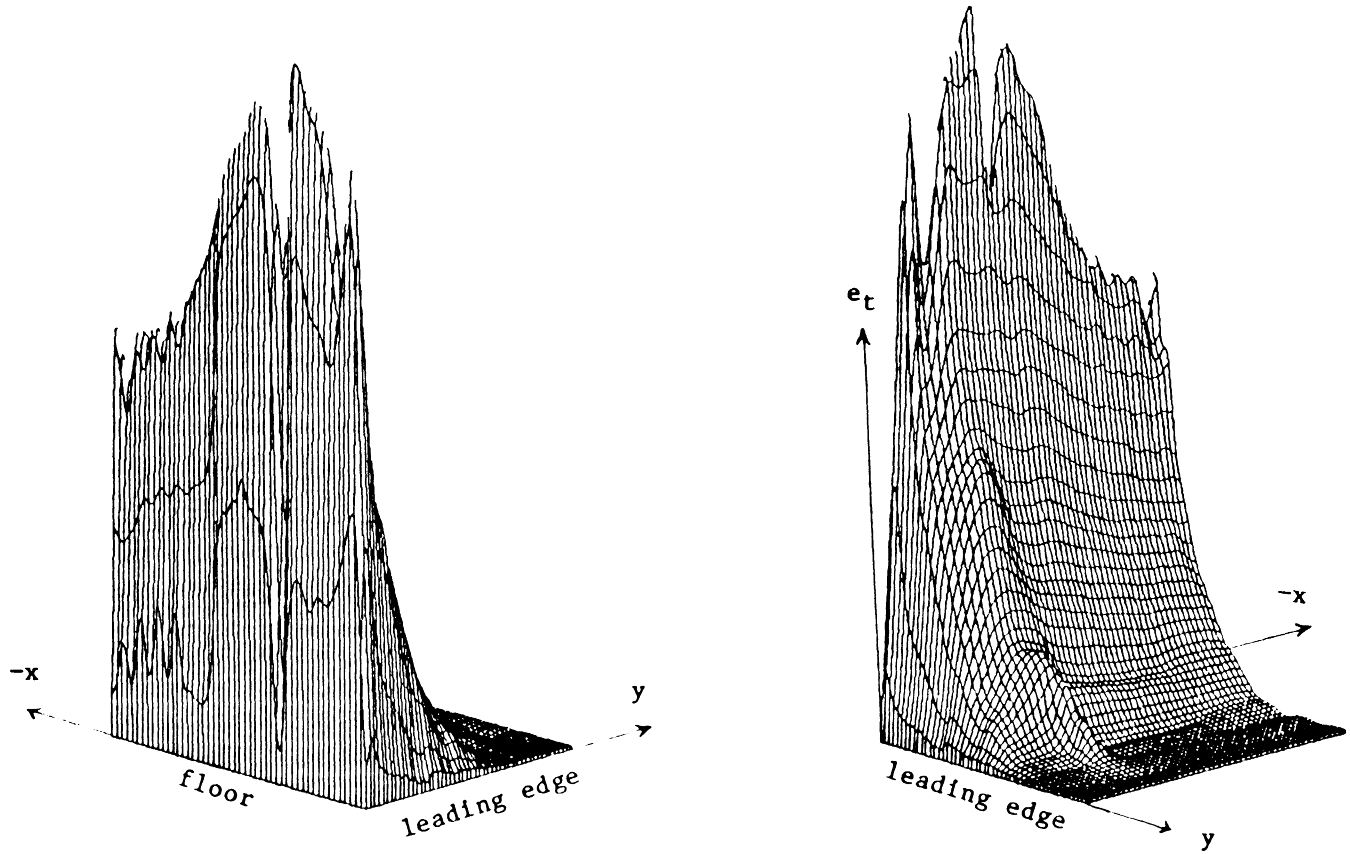

Figure 5-12 3-D Representation of e_t Distribution for the Fence Case.

same details as the contour maps. The discussion of Figs. 5-1 through 5-6 relates to Figs. 5-7 through 5-12 as well.

All these plots have been scaled to have the same physical size, any magnitude comparison should be made on the contour maps. The topographic plots can be used as visualization aids and for comparing overall shapes but not magnitudes.

These figures showed clearly the large increase in energy in going from the outer flow to the floor (moving along the negative y direction). The energy could also be seen to increase in the +x direction up to the nominal vortex center, beyond which there generally was a decrease of energy up to the cylindric body.

The darkened flat areas adjacent to the xy origins, represent the fillets. The large circular fillet is clearly seen in Fig. 5-8, whereas the small elliptic fillet is not obvious in Fig. 5-9. This is due to the relatively small size of this fillet which is dwarfed by the e_t distribution.

The large triangular fillet of Fig. 5-11 had the smoothest e_t distribution, especially when compared to the no fillet case or the vortex generator fence of Fig. 5-12. The fence, which was not visible on this topographic map, caused several local energy peaks to be created.

5-3 Turbulent Kinetic Energy (E_t)

As described in Section 5-1, the data field was extrapolated in the -x direction by 25.4 mm to achieve an upstream boundary condition nearly the same for each of the different geometries. The extrapolation was performed as follows. The energy contained in slab A as defined in Fig. 5-13 was calculated according to the procedure developed in Section 4-3, for each geometry. Slab A was 6.35 mm wide so that by adding four more slabs of identical width (slabs B through E) the 25.4 mm extension could be achieved. The energy contained in the added slabs B through E was calculated using a piecewise linear decay of the energy contained in A. This linear extrapolation model can be justified by the slopes of the contour lines in Figs. 5-1 through 5-6. These contours can be approximated by straight lines upstream of x = -150 mm. Here again, the no fillet case was used as reference and was assumed to have a constant kinetic energy distribution upstream of x = -177.8 mm. This assumption implied that all five slabs had the same energy content for this case.

The energy contained in each slab was given by:

$$B = A - \frac{1}{2}(A - A_{NF})$$
$$C = B - \frac{1}{2}(B - B_{NF})$$
$$D = C - \frac{1}{2}(C - C_{NF})$$
$$E = D - \frac{1}{2}(D - D_{NF})$$

$$A_{NF} = B_{NF} = C_{NF} = D_{NF} = E_{NF}$$

where the subscript NF refers to the energy calculated for the no fillet case. This in effect forces the energy calculated in slab A for each modified flow to decay to approximately the value calculated for the no fillet case. This method reduced the differences in computed energy content that existed in slab A to the more similar values computed for

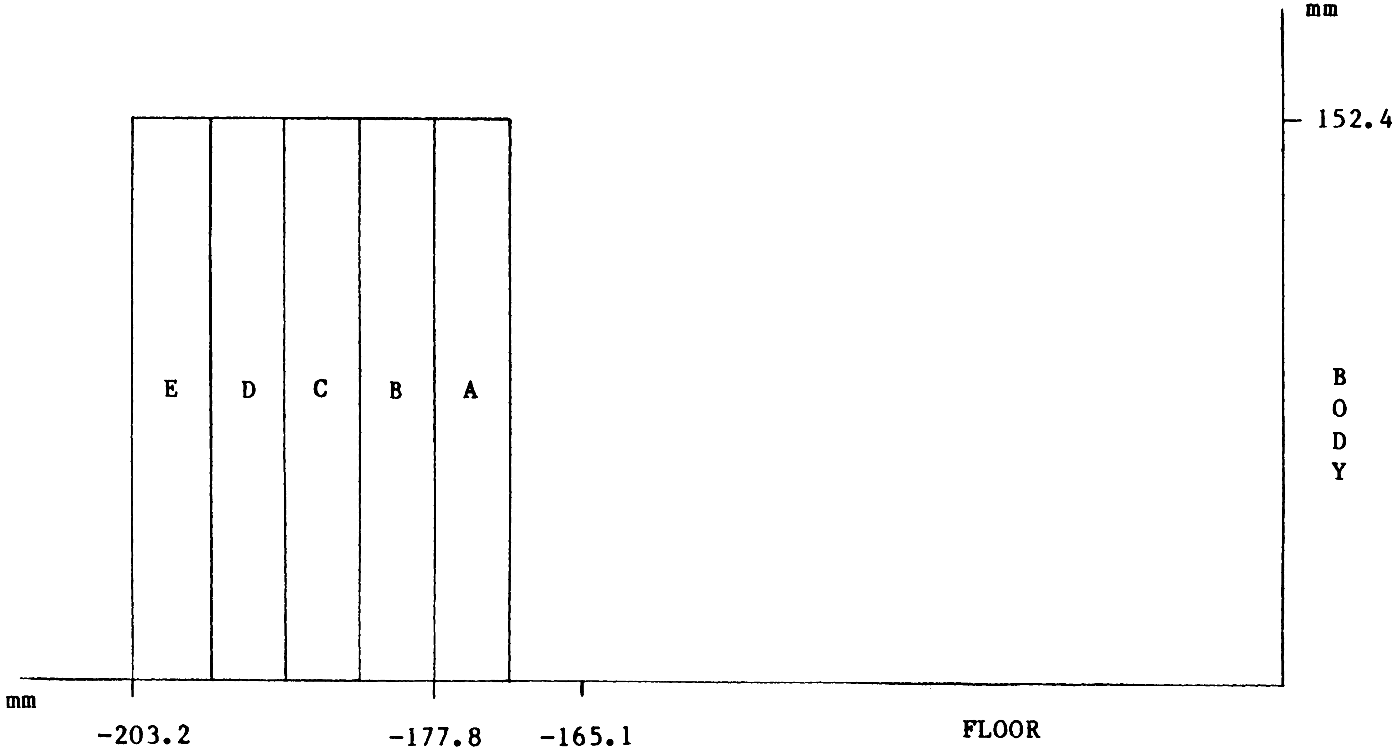

Figure 5-13 Extrapolation for the Energy Density.

slab E. Thus, slab E represented a more uniform boundary. The overall extrapolation for each case was the sum of the energy contained in each slab:

$$\text{adjustment} = B + C + D + E$$

The results of this adjustment method are shown in Tables 5-1 and 5-2. The results from this analysis are supported by the observations made on the contour maps.

Table 5-1

Extrapolation of the Total E_t

Case	Slab A	Slab B	Slab C	Slab D	Slab E	Total Extrapolation B+C+D+E
no fillet	1.287	1.287	1.287	1.287	1.287	5.148
large circular fillet	1.432	1.360	1.323	1.305	1.296	5.284
small elliptic fillet	1.287	1.287	1.287	1.287	1.287	5.148
small circular fillet	1.359	1.323	1.305	1.296	1.292	5.216
large triangular fillet	1.697	1.492	1.390	1.338	1.313	5.533
vortex generator fence	1.351	1.319	1.303	1.295	1.291	5.208

Note: All numerical values are nondimensionalized E_t values which must be multiplied by 10^{-6}.

Table 5-2

Corrected Total E_t

Case	Total E_t up to x = -177.8 mm		Total extrapolation		Total E_t up to x = -203.2 mm
no fillet	45.249	+	5.148	=	50.397
large circular fillet	50.968	+	5.284	=	56.252
small elliptic fillet	44.875	+	5.148	=	50.023
small circular fillet	48.250	+	5.216	=	53.465
large triangular fillet	35.211	+	5.533	=	40.744
fence	47.751	+	5.208	=	52.959

Comparison of Corrected Total E_t

Case	Corrected E_t	% Difference	Comment
no fillet	50.397	reference	
large circular fillet	56.252	+ 11.62	modest increase
small elliptic fillet	50.023	- 0.74	insignificant difference
small circular fillet	53.465	+ 6.09	small increase
large triangular fillet	40.744	- 19.15	significant decrease
fence	52.959	+ 5.08	small increase

Note: All numerical values are nondimensionalized E_t values which must be multiplied by 10^{-6}.

5-4 Spectral Estimates

The Fourier transform outputs computed by the Data 6000 digital signal processor [10] were:

$$F_1(m) = \frac{1}{\sqrt{N}} \sum_{n=0}^{N-1} x_n \cos \frac{2\pi nm}{N}$$

$$F_2(m) = \frac{1}{\sqrt{N}} \sum_{n=0}^{N-1} x_n \sin \frac{2\pi nm}{2N} \qquad m = 0,1,2 \ . \ . \ .N - 1$$

where

$F_1(m)$ = m^{th} component of the cosine transform

$F_2(m)$ = m^{th} component of the sine transform

N = Number of points acquired (must be 2^n number)

x_n = n^{th} value of acquired record (volts) multiplied by the window, $W(m)$.

The two types of spectra computed from the above output selections were:

(1) F_{MAG} (magnitude) plotted on a linear y-scale in volts,

$$F_{MAG} = 2(F_1^2 + F_2^2)^{1/2}$$

(2) F_{ALOG} (absolute log) plotted on a logarithmic scale in dBm,

$$F_{ALOG} = 20 \log \left[F_{MAG}(W2 \cdot \Delta t)^{1/2}\right] + \text{constant}$$

where

W2 = windowing factor (0.375 for the Hanning window used)

Δt = sampling period

A spectrum using the MAG output option was computed for every other grid point for each geometry modification.

All the spectra were found to have very similar shapes regardless of geometry condition or position in the grid matrix. They differed only by their magnitude along the y-axis (vertical axis). This observation suggests that the turbulent boundary layer is the driving force for the junction vortex since their spectra are very similar apart from the magnitudes. The vortex seemed to amplify the low frequencies up to 2 kHz beyond which there was a significant reduction as seen in the spectra with ordinate values displayed on a linear scale. Figure 5-14 shows the two extreme spectra for the no fillet case and these are typical of the other geometries.

Since all the shapes were very similar, a comparison was made in terms of the magnitude of the peaks. Six spectra with different values for the peaks or maxima were arbitrarily selected from the no fillet set of spectra. The same peak magnitude was looked for at or around the same grid point for each geometry. Figure 5-15 shows six such groups of nearly identical spectra displaced in space. It was assumed that when all the spectra lie at about the same physical location (group 1) no geometry effect was detected. On the other hand, group 2 shows how the two large fillets (circular and triangular) displaced the higher energy

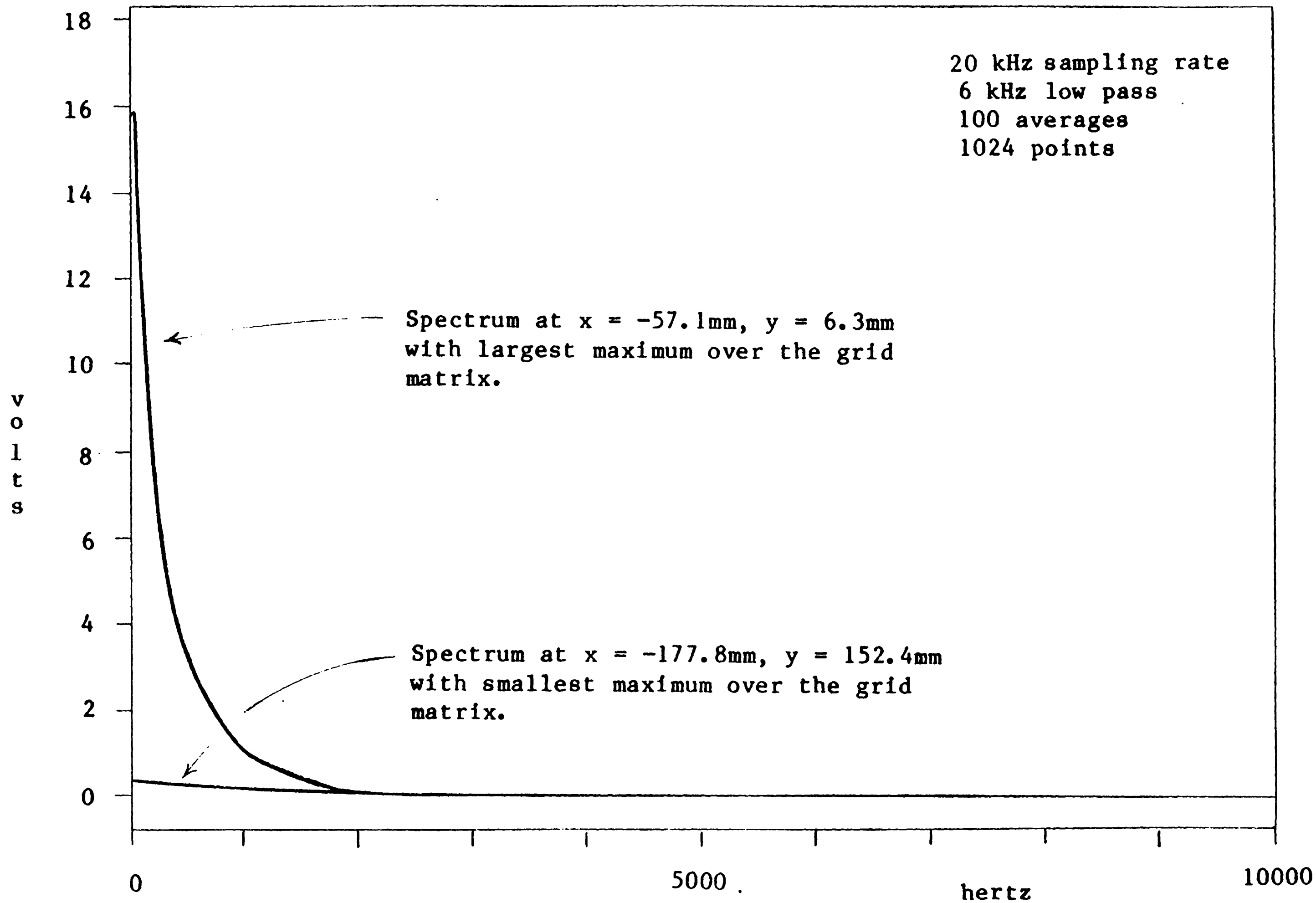

Figure 5-14 Peak Magnitude Extremes for the No Fillet Case Spectra.

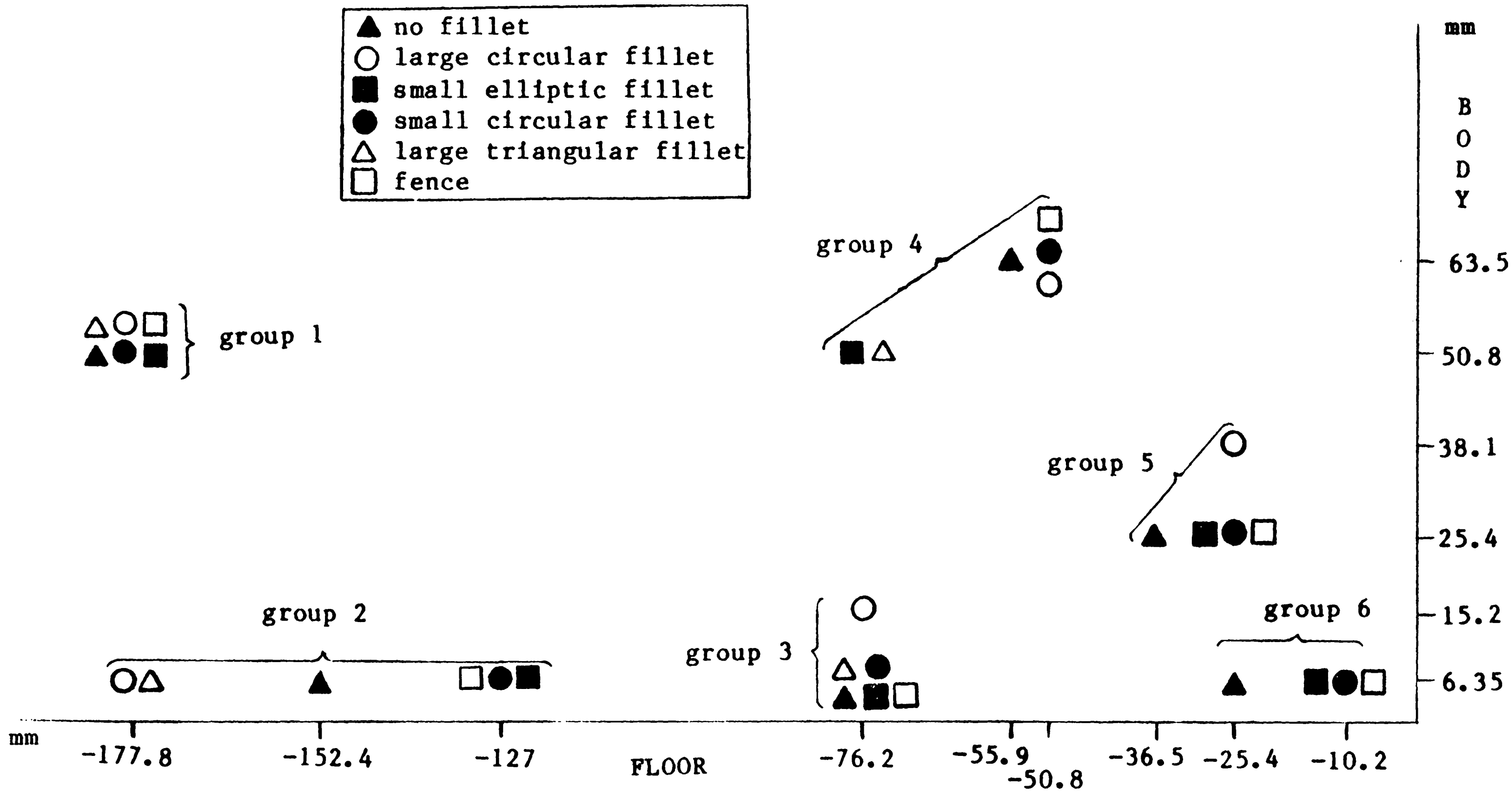

Figure 5-15 Displacement of Energy Due to Geometry Change.

fluid upstream, whereas the small fillets and the fence appear to have displaced this higher energy fluid downstream. A typical set of spectra representing group 4 are given in appendix B.

Although all the spectra taken tend to suggest that the upstream turbulent boundary layer drives the vortex, the real time smoke visualizations can be interpreted to show low frequency oscillations of the vortex. The spectra taken over a 10 kHz band width did not have a high resolution. In an effort to identify any vortex oscillating frequencies at the lower frequencies, the resolution was increased by sampling at 2 msec and low passing at 150 Hz with all other parameters remaining unchanged. These results are offered with reservation since the spectra were truncated at 150 Hz, beyond which a significant portion of the energy was suppressed by the filter, but resulting in some aliasing. No investigation or analysis was performed to estimate the extent of the signal's contamination. Nevertheless, two spectra were taken for the no fillet case at the same distance from the floor (y=4mm). Figure 5-16 shows results at x = -177.8 mm, well upstream of the vortex and separation. Figure 5-17 was taken at x = -71.1 mm where the vortex passed frequently on its excursions from its mean position. This location was about 10 mm upstream of the mean position of the primary separation. Here again, the shapes were very similar with the peak value increased toward the body where the large flow fluctuations occur. Figure 5-17 can be interpreted to show a peak at about 11 Hz when compared to Fig. 5-16. The upstream flow in Fig. 5-16 appears characterized by a broader band signal in the frequency interval, whereas the vortex flow in Fig. 5-17 suggests a local peak over the same band signal.

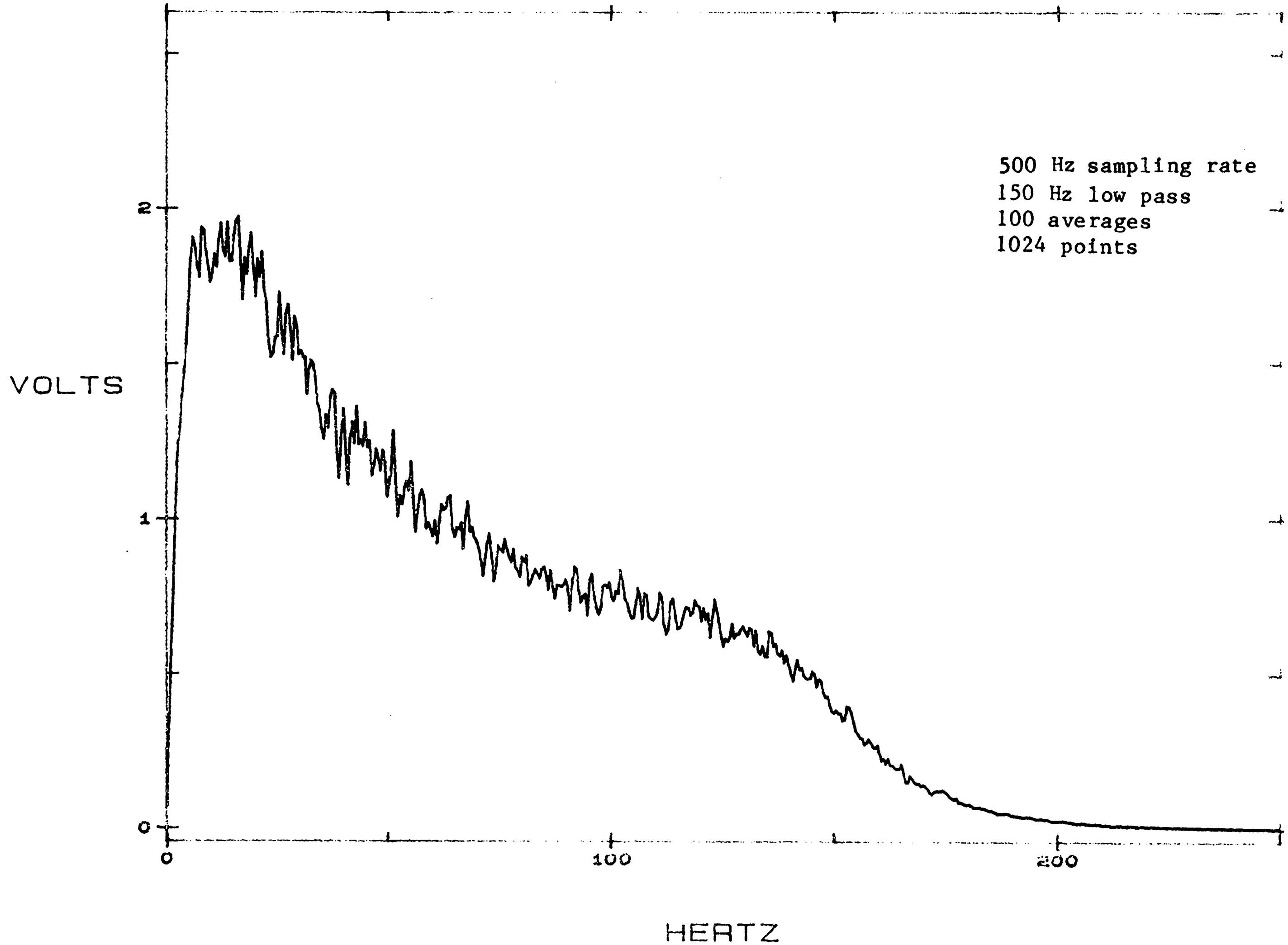

Figure 5-16 No Fillet Case Spectrum with a 150 Hz Low Pass at x = -177.8mm.

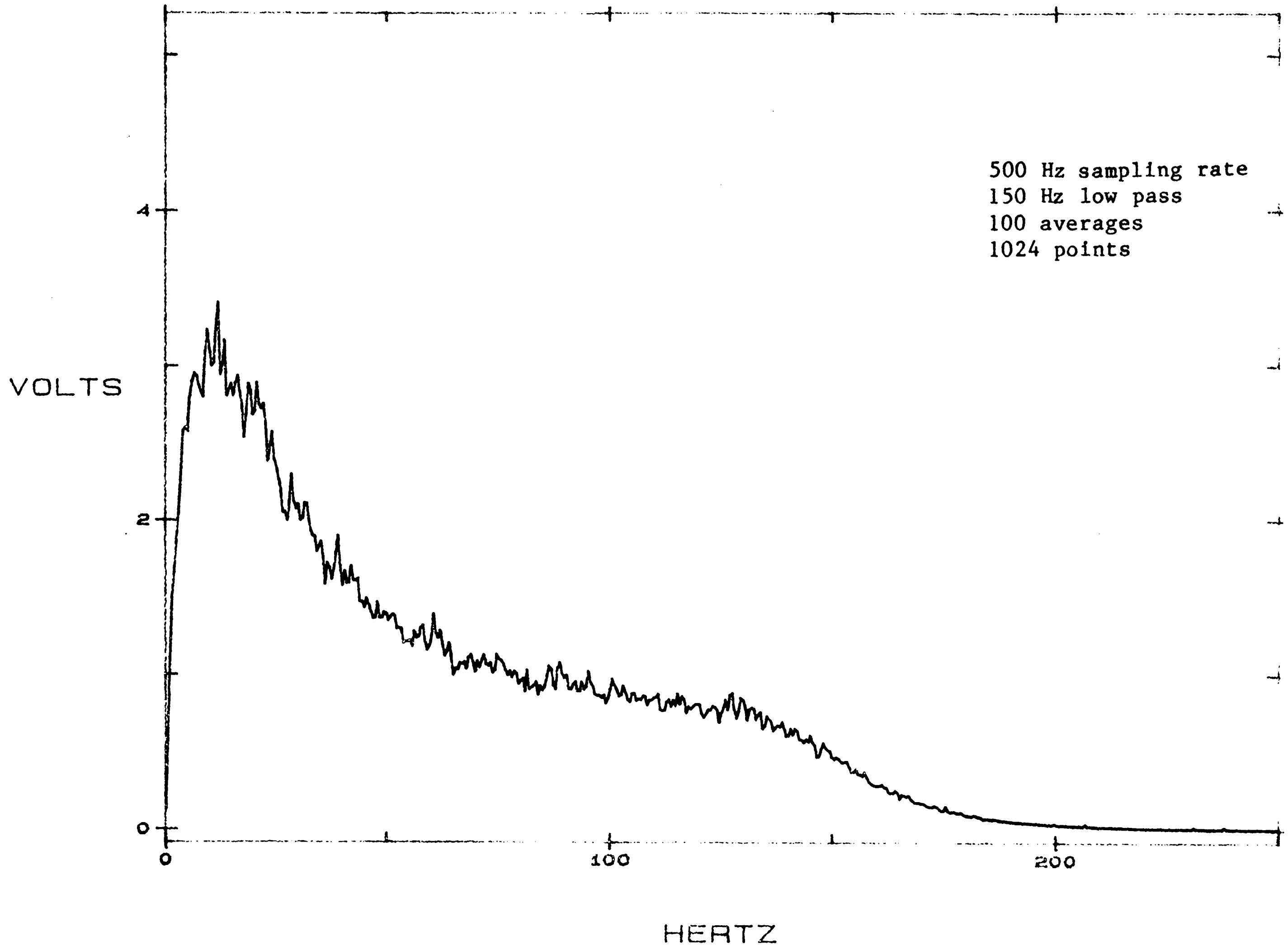

Figure 5-17 No Fillet Case Spectrum with a 150 Hz Low Pass at x = -71.1 mm.

6. CONCLUSIONS

The effects of geometry modifications on some properties of time resolved flow measurements on the upstream symmetry plane of a junction vortex region were studied. A single linearized hot-wire was used to characterize the spatial distribution of the fluctuating flow turbulent kinetic energy. The distribution was integrated to give a measure of the turbulent kinetic energy content of the flow region where the largest fluctuations were seen in real time smoke visualizations. The wire signal was also used for spectral estimations throughout the flow field.

Six different cases were considered including a reference case with no geometry changes. The geometry modifications consisted of a large circular wraparound fillet, a small elliptic wraparound fillet, a small circular wraparound fillet, an upstream flow fence and, a large leading edge triangular fillet. In the smoke visualizations, none of the modifications had any significant effect except the large triangular fillet which resulted in a reduced vortex structure. The large triangular fillet also appeared to be the most effective in significantly reducing the integrated turbulent kinetic energy. With regard to the turbulent kinetic energy, the elliptic wraparound fillet had an insignificant effect while the large and small wraparound fillets and the vortex generator fence had adverse effects.

The spectra obtained over the flow field suggest that the upstream turbulent boundary layer was the driving force behind the junction vortex time variant behavior. An examination of the low frequency end of the spectra suggests a weak local peak at about 11 Hz for the flow between the upstream separation point and the average vortex center.

REFERENCES

1. Baker, C. J., "The Turbulent Horseshoe Vortex," Journal of Wind Engineering and Industrial Aerodynamics, June 1980.

2. Menna, J. D., "A Three-Dimensional Turbulent Boundary Layer Upstream and Around a Junction Vortex Flow," Dissertation, Mechanical Engineering, Virginia Polytechnic Institute and State University, Blacksburg, Virginia, May 1984.

3. Harsh, M. D., "An Experimental Investigation of a Turbulent Junction Vortex," Dissertation, Mechanical Engineering, Virginia Polytechnic Institute and State University, Rept. VPI-E-85-4, Blacksburg, Virginia, February 1985.

4. Tree, I. K., "Laser-Doppler Measurements in a Turbulent Junction Vortex," Dissertation, Mechanical Engineering, Virginia Polytechnic Institute and State University, Blacksburg, Virginia, 1985.

5. Squire, L. C., Maltby, R. L., Keating, R. F. A., and Stanbrook, A., "The Surface Oil Flow Technique, Flow Visualization in Wind Tunnels Using Indiators," NATO Agardograph No. 70, North Atlantic Treaty Organization Advisory Group for Aerospace Research and Development, April, 1962, pp. 1-74.

6. Saad, M. A., Compressible Fluid Flow, Prentice-Hall, New Jersey, 1985, pp. 499-500.

7. White, F. M., Fluid Mechanics, McGraw Hill, New York, 1979, pp. 279.

8. Disa, "Type 55M25 Linearizer," Instruction Manual, Disa Electronics Corporation, New Jersey.

9. Klebanoff, P. S., "Characteristics of Turbulence in a Boundary Layer with Zero Pressure Gradient," NACA TN3178, July 1954.

10. Data 6000, "Application Note No. 304, FFT Outputs on the Data 6000," Analogic Corporation, Danvers, Massachusetts.

11. Kay, S. M., and Marple, S., "Spectrum Analysis--A Modern Perspective," Proceedings of the IEEE, Vol. 69, No. 11, 1981.

12. Disa, "Type 55D35 RMS Voltmeter," Instruction and Service Manual, Disa Electronics Corporation, New Jersey.

13. Sampson, R. J., "Surface II Graphics Systems," Series on Spatial Analysis, Kansas Geological Survey, Lawrence, Kansas.

APPENDIX A

Data Stations for Each Geometry

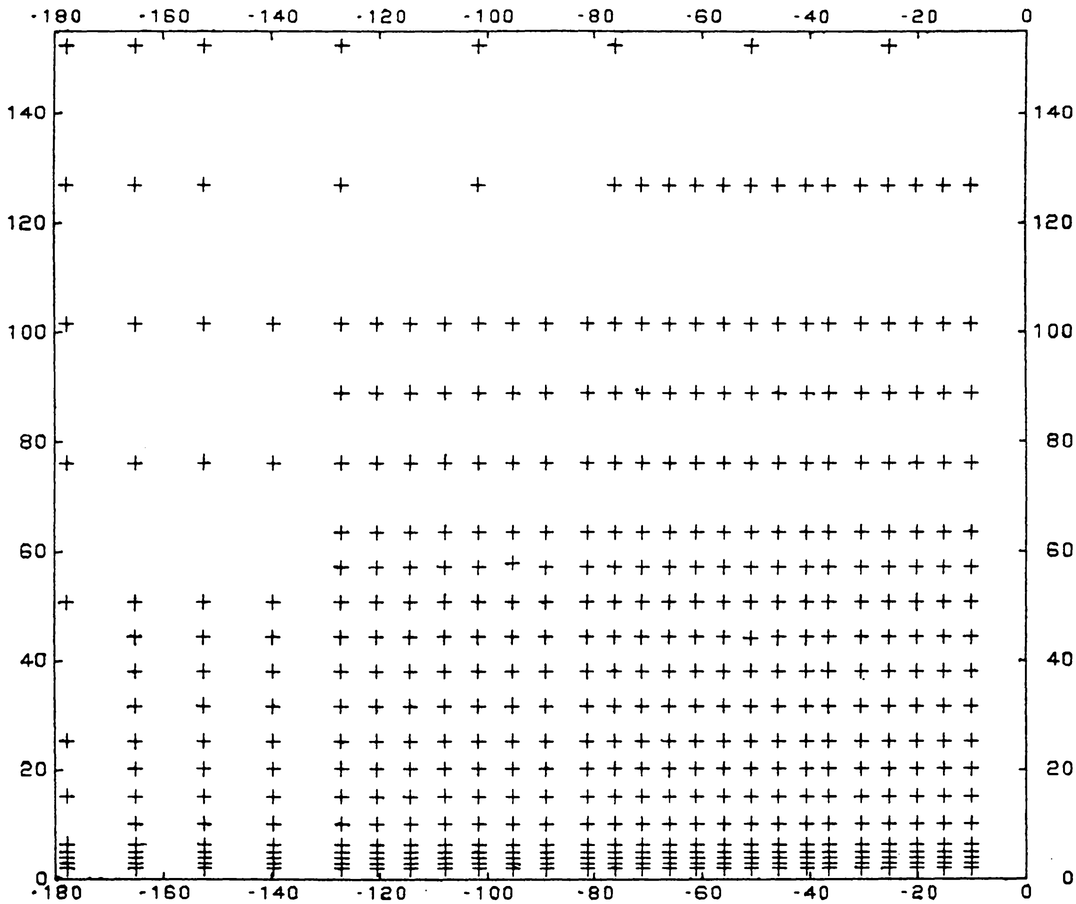

Figure A-1 Data Stations for No Fillet Case.

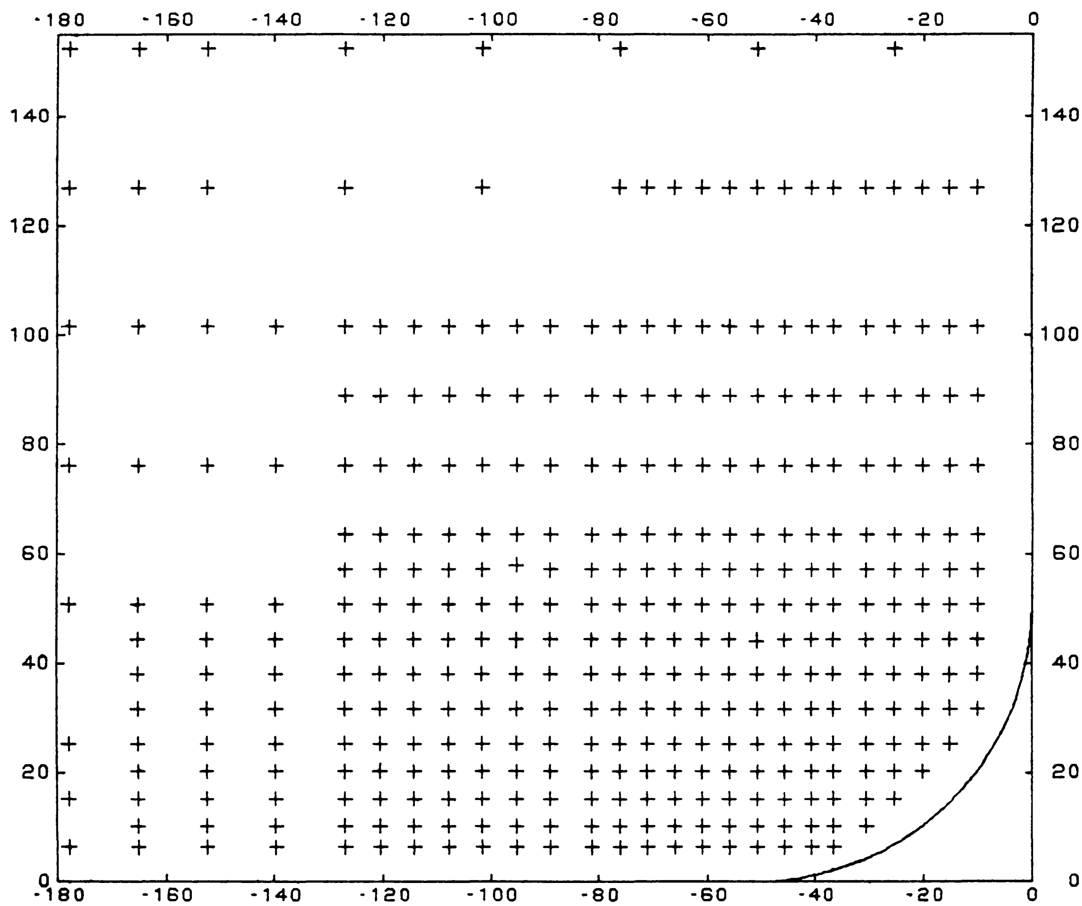

Figure A-2 Data Stations for Large Circular Fillet Case.

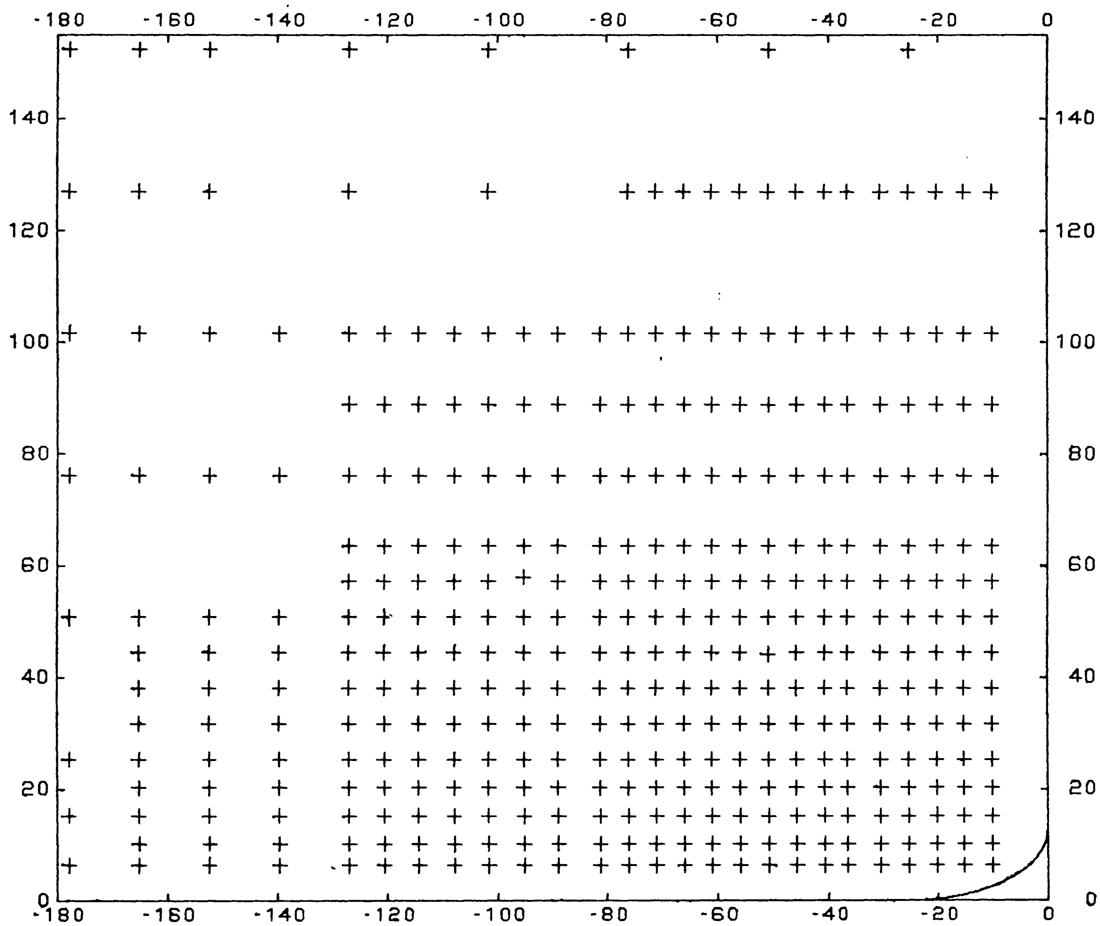

Figure A-3 Data Stations for Small Elliptic Fillet Case.

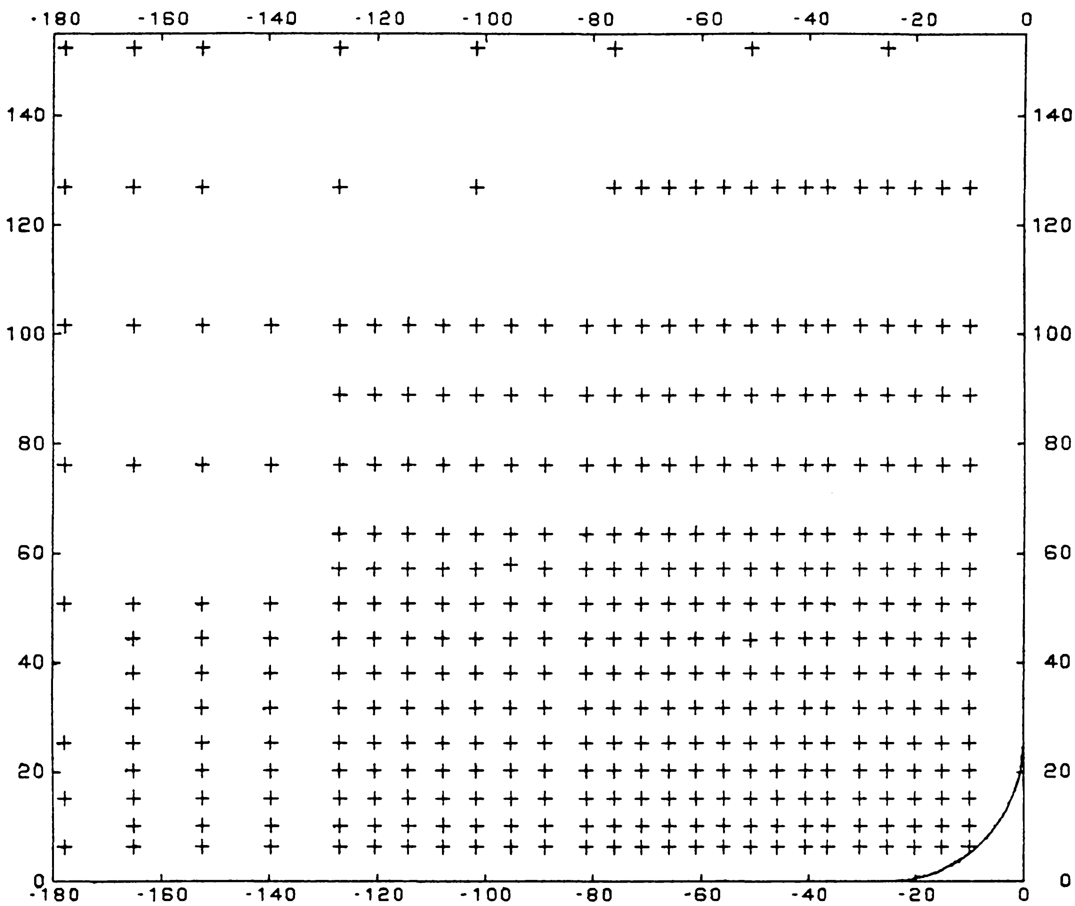

Figure A-4 Data Stations for Small Circular Fillet Case.

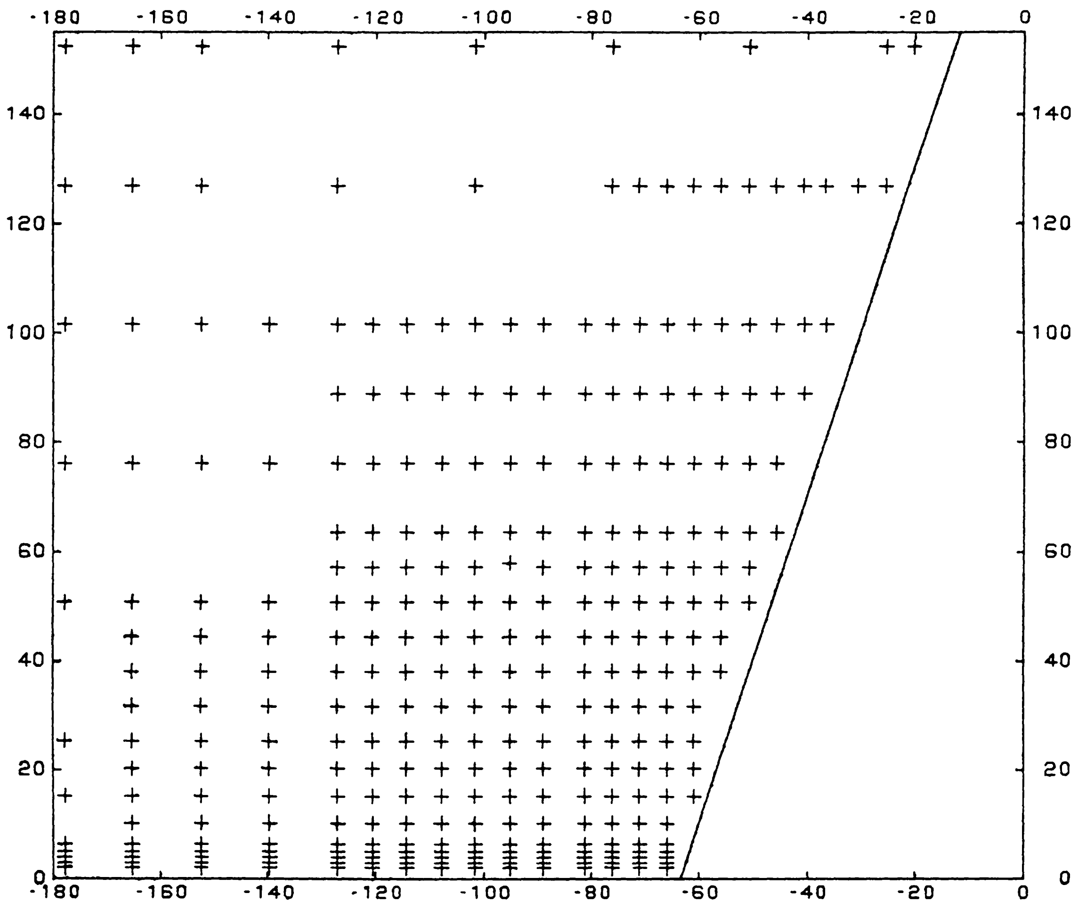

Figure A-5 Data Stations for Large Triangular Fillet Case.

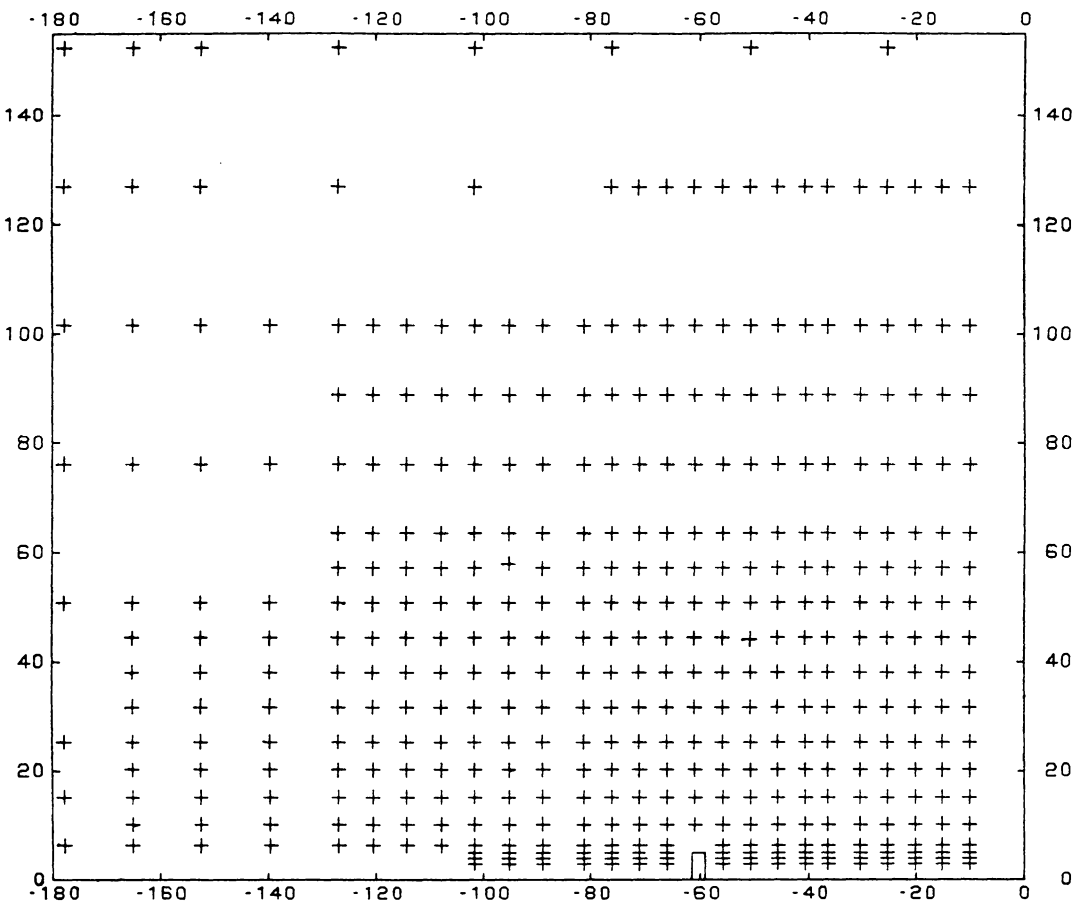

Figure A-6 Data Stations for the Fence Case.

APPENDIX B

Selected Spectra

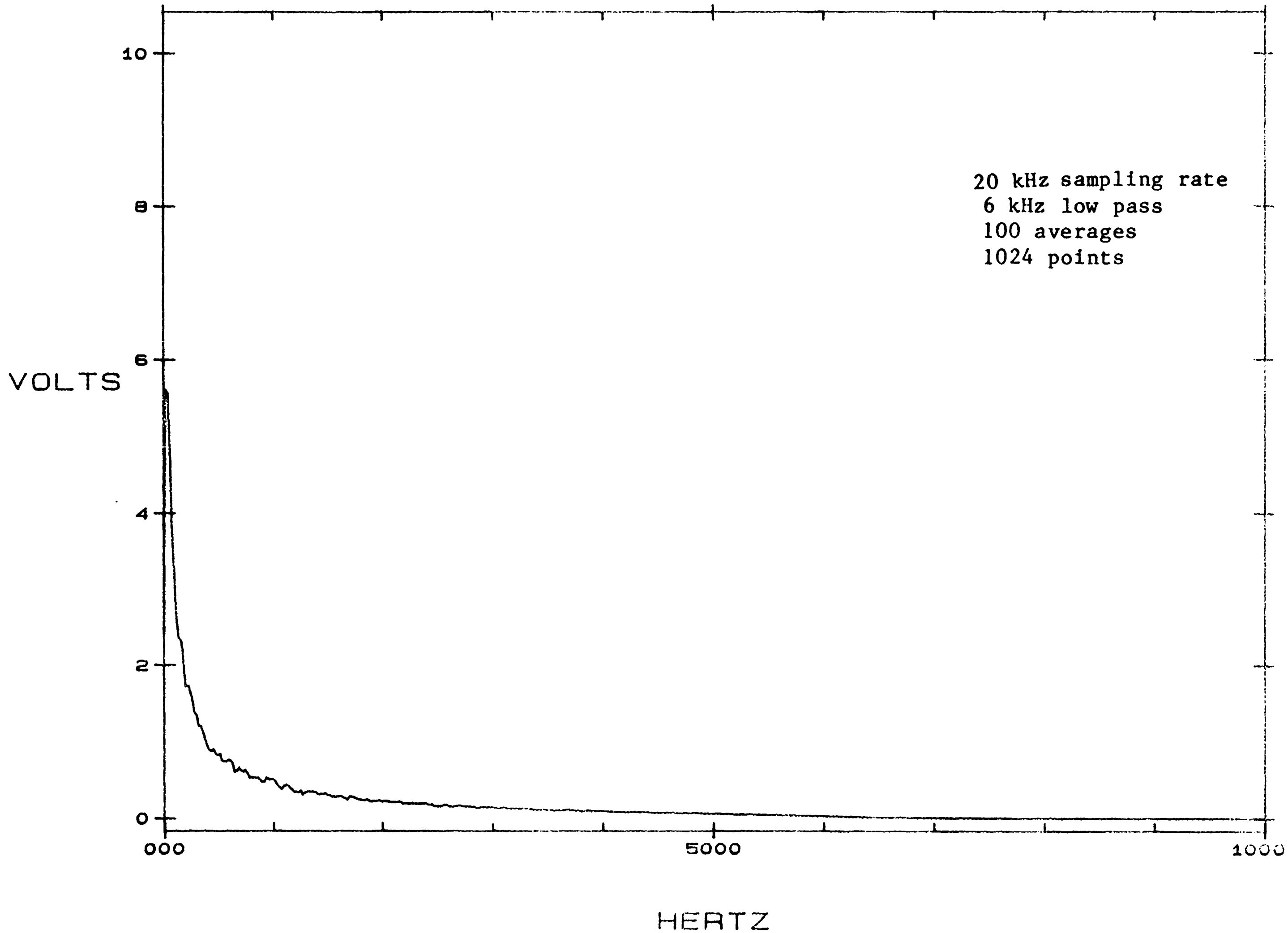

Figure B-1 Spectrum for No Fillet Case at x = -55.9 and y = 63.5.

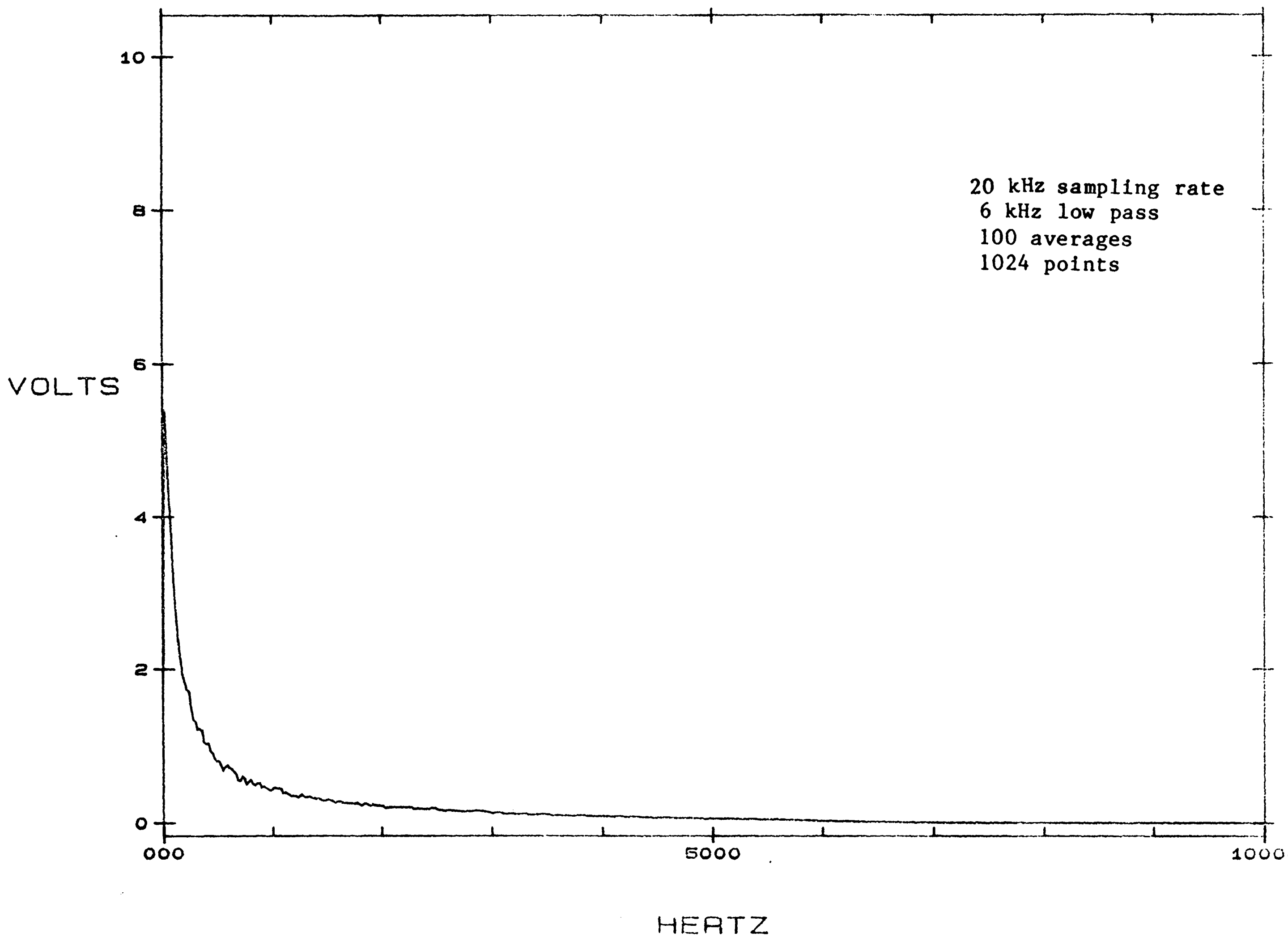

Figure B-2 Spectrum for Large Circular Fillet case at x = -50.8 and y = 63.5.

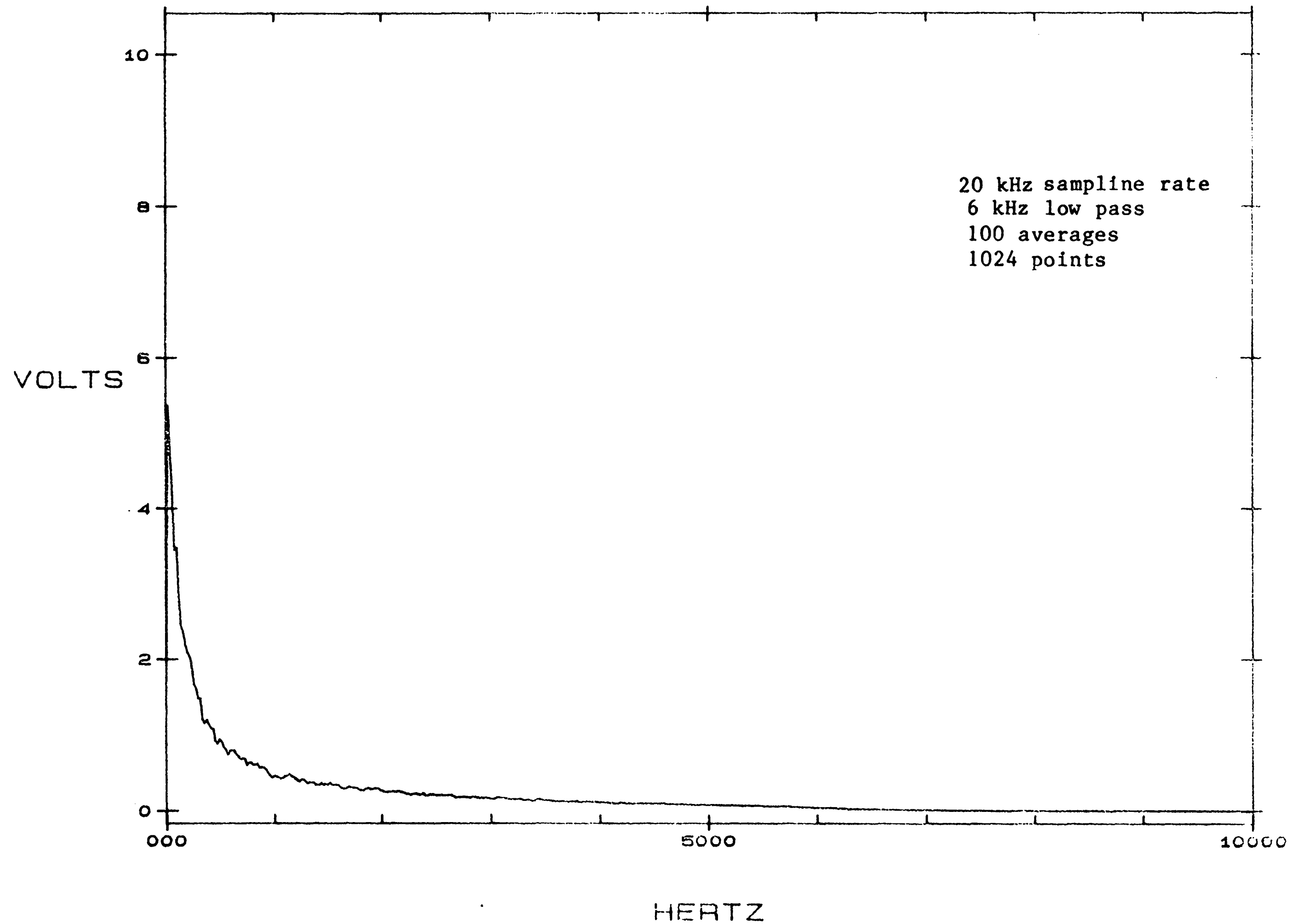

Figure B-3 Spectrum for Small Elliptic Fillet Case at x = -76.2 and y = 50.8.

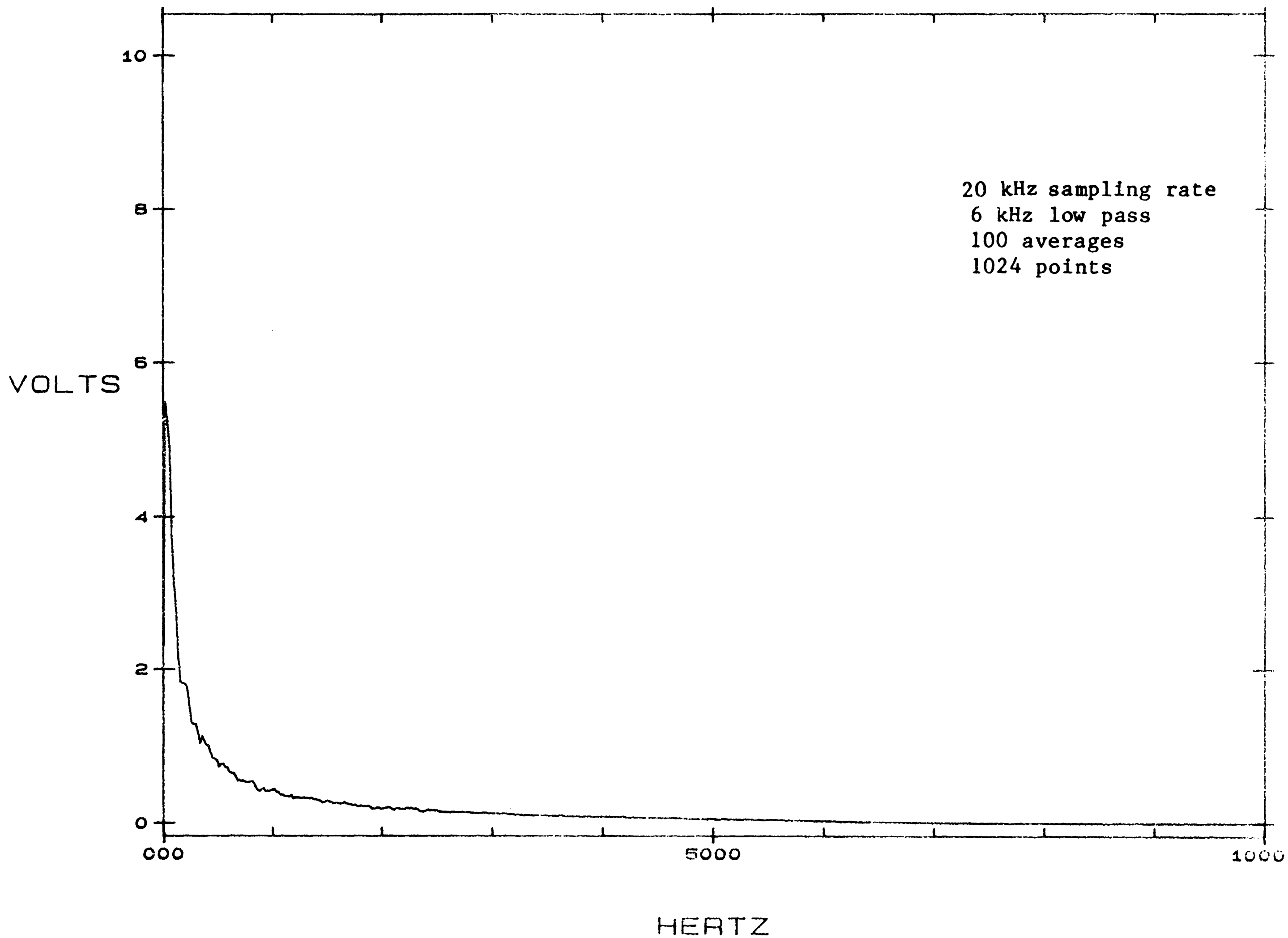

Figure B-4 Spectrum for Small Circular Fillet Case at x = -50.8 and y = 63.5

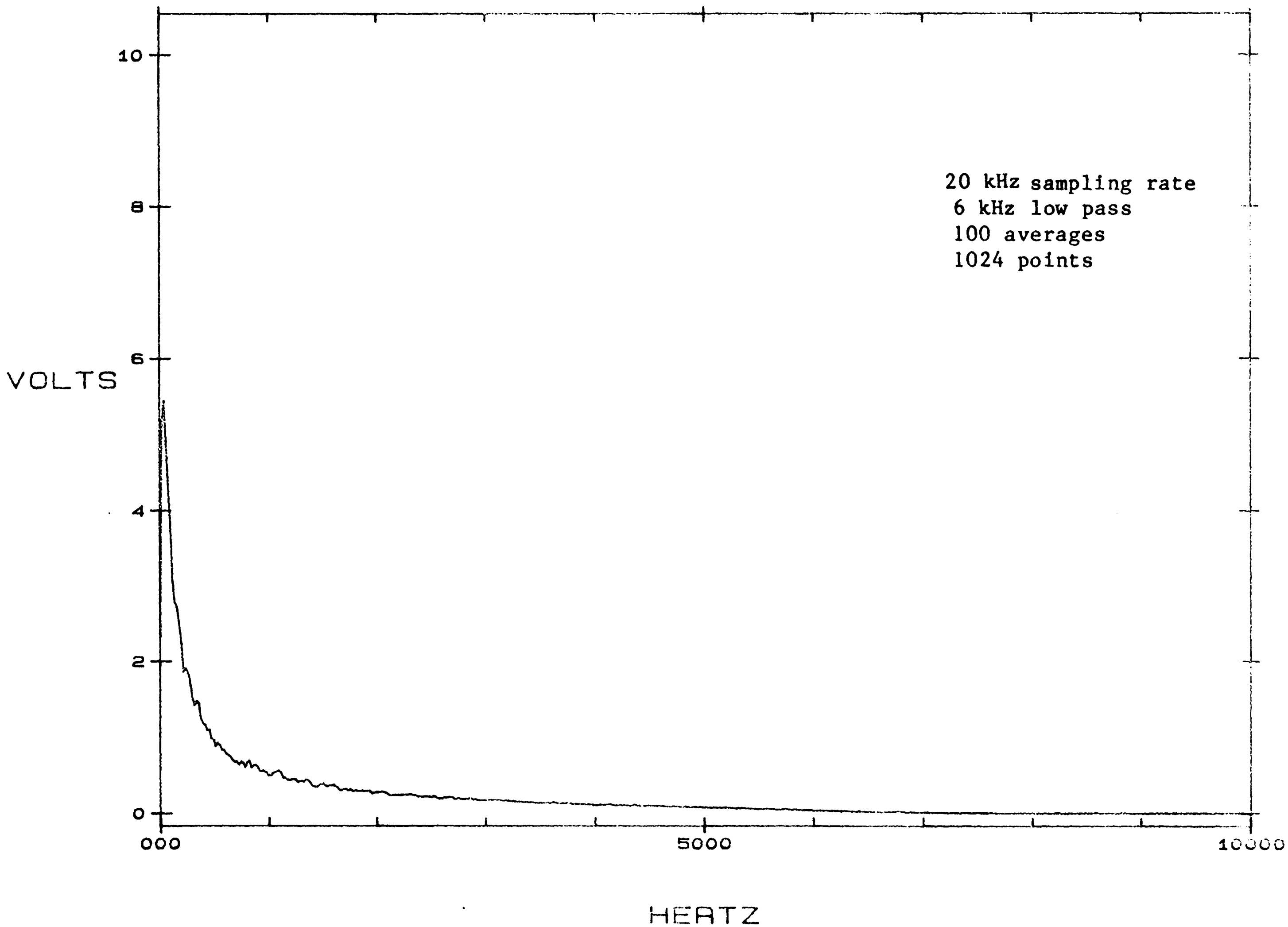

Figure B-5 Spectrum for Large Triangular Fillet Case at x = -76.2 and y = 50.8.

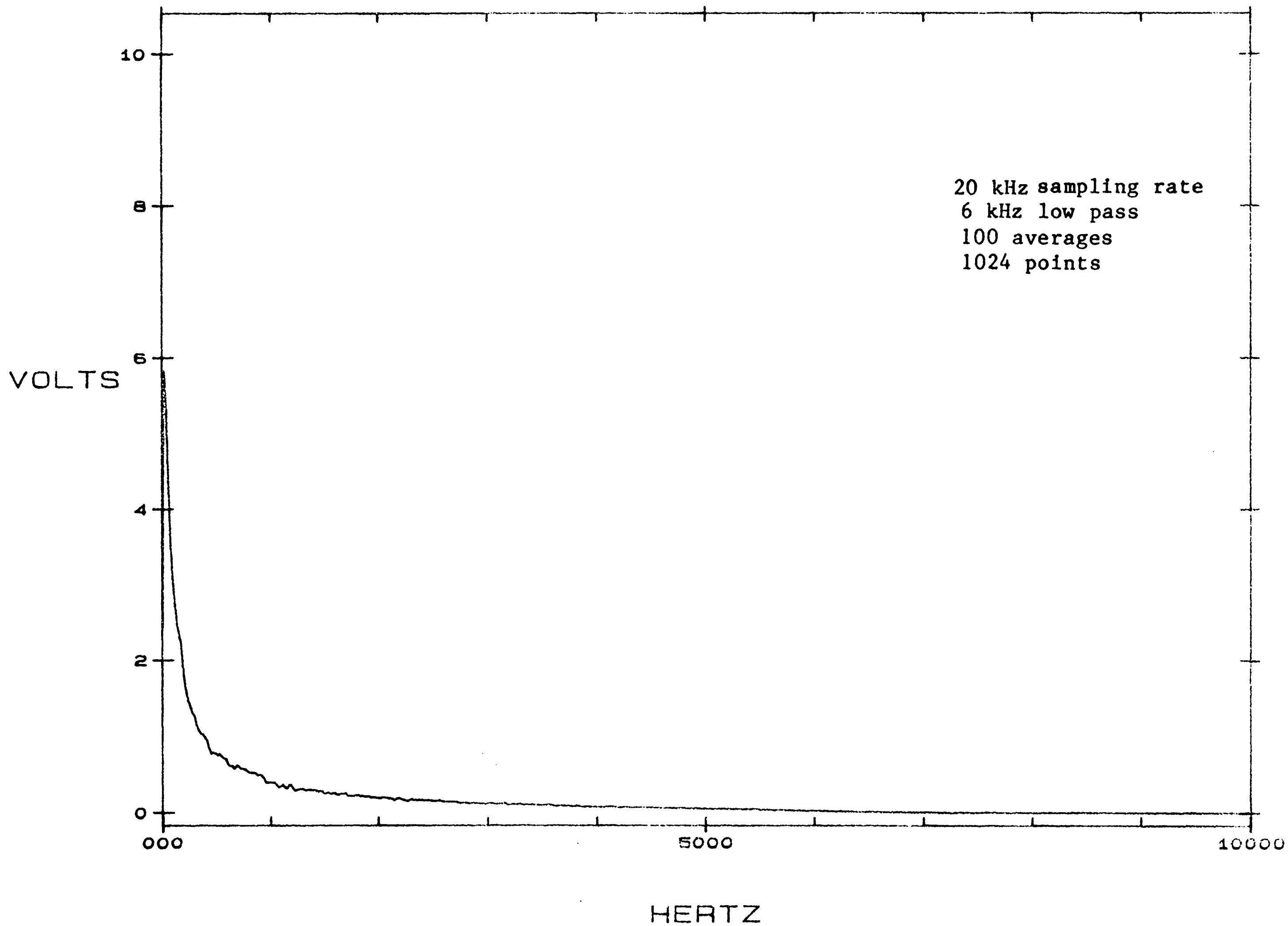

Figure B-6 Spectrum for Fence Case at x =-50.8 and y = 63.5

The vita has been removed from the scanned document